



저작자표시-비영리-변경금지 2.0 대한민국

이용자는 아래의 조건을 따르는 경우에 한하여 자유롭게

- 이 저작물을 복제, 배포, 전송, 전시, 공연 및 방송할 수 있습니다.

다음과 같은 조건을 따라야 합니다:



저작자표시. 귀하는 원저작자를 표시하여야 합니다.



비영리. 귀하는 이 저작물을 영리 목적으로 이용할 수 없습니다.



변경금지. 귀하는 이 저작물을 개작, 변형 또는 가공할 수 없습니다.

- 귀하는, 이 저작물의 재이용이나 배포의 경우, 이 저작물에 적용된 이용허락조건을 명확하게 나타내어야 합니다.
- 저작권자로부터 별도의 허가를 받으면 이러한 조건들은 적용되지 않습니다.

저작권법에 따른 이용자의 권리는 위의 내용에 의하여 영향을 받지 않습니다.

이것은 [이용허락규약\(Legal Code\)](#)을 이해하기 쉽게 요약한 것입니다.

[Disclaimer](#)

공학박사 학위논문

**파편 재진입 생존성 분석을 고려한
우주발사체 상단의 비행안전 분석**

Flight Safety Analyses on the Upper Stage of a Space
Launch Vehicle with Survivability Analyses of Debris
Reentering the Earth's Atmosphere

2013년 2월

서울대학교 대학원

기계항공공학부

심 형 석

파편 재진입 생존성 분석을 고려한 우주발사체 상단의 비행안전 분석

Flight Safety Analyses on the Upper Stage of a Space
Launch Vehicle with Survivability Analyses of Debris
Reentering the Earth's Atmosphere

지도교수 김 규 홍

이 논문을 공학박사 학위논문으로 제출함

2012 년 12 월

서울대학교 대학원

기계항공공학부

심 형 석

심형석의 공학박사 학위논문을 인준함

2012 년 12월

위 원 장 _____ (인)

부위원장 _____ (인)

위 원 _____ (인)

위 원 _____ (인)

위 원 _____ (인)

Abstract

Flight Safety Analyses on the Upper Stage of a Space Launch Vehicle with Survivability Analyses of Debris Reentering the Earth's Atmosphere

Hyung-Seok Sim

School of Mechanical and Aerospace Engineering

The Graduate School

Seoul National University

The key point of this study is to analyze the flight safety of a space launch vehicle accounting for the survivability of vehicle debris in order to accurately assess the risk posed to the public on the ground in case of the failure of a launch vehicle flying at high velocity.

The flight safety analysis of a space launch vehicle is conducted by assuming the failure of a launch vehicle, simulating debris free fall, analyzing impact distribution areas of debris, and then computing the expected casualty with casualty areas of the fragments and a population data model. If a vehicle fails at high velocity, the falling debris might partially melt or fully demise due to high aerothermodynamic loads resulting in the reduction of hazard to the people on the ground. In this light, reentry survivability analyses on the high speed fragments are required for more precise estimation of the ground risk posed by the launch vehicle failure.

This study was focused on the three contents for accurate flight safety analysis of a space launch vehicle.

Firstly, a program to analyze the flight safety of a launch vehicle was developed. In order to compute the distribution area of impacting debris from the flight failure of a launch vehicle, the uncertainty in the imparted velocity of debris by explosion, the uncertainty in debris ballistic coefficients, vehicle guidance and performance error, and the uncertainty in the effect by wind and lift were considered. A sheltering model to account for the protection provided to persons located inside structures was employed. Finally, the expected casualty was analyzed utilizing the fragment impact distribution data, debris casualty area, and the population distribution model. The analysis results were compared with those of TumCor program developed by ACTA (Inc) in USA which employs relatively simple approach for expected casualty analysis.

Secondly, a code to analyze the survivability of debris reentering the Earth's atmosphere at high velocity was developed. The aerothermodynamic load during free fall, the temperature variation due to thermal load, and the phase shift after reaching the melting point were integrated into the 3-DOF trajectory simulation of debris in order to analyze the size and weight of the debris impacting the ground. The results of survivability analyses on simple shaped objects were compared to the ones obtained by the codes developed by NASA and ESA in order to validate the developed code. In addition, the analysis on an actually reentered orbital object using the developed code was performed for the comparison with the measured results.

Finally, the developed survivability analysis code was combined with the flight safety analysis program to analyze the flight safety of the upper stage of a 2-stage launch vehicle. The effect of incorporating the survivability analysis in the flight safety analysis procedure was investigated by comparing the expected casualty results with the case when the fragments are assumed to impact the Earth in their initial state without any mass loss. As a result, it is shown that the expected casualty value considering the demise of debris was considerably lower than the case in which the survivability analysis was excluded. Consequently, it is noted that the consideration of the survivability analysis is essential in the flight safety analysis for the period when the vehicle flies at very high speed. Furthermore, in order to investigate the effects of

Abstract

uncertainty variations, analyses using the developed program with various conditions were conducted. It was shown that the wind profile, the IIP trajectory, and the explosion velocity can have significant effects on the expected casualty of a launch vehicle.

Keywords: Launch Vehicle, Flight safety Analysis, Fragment Impact area, Sheltering, Earth Reentry, Hypersonic, Aerothermodynamic load, Survivability

Student Number: 2009-30167

Name: Sim, Hyung Seook

Contents

CHAPTER 1. INTRODUCTION	1
1.1 Flight safety analysis of space launch vehicles	1
1.1.1 The history of flight safety analysis of space launch vehicles	2
1.1.2 The procedure of flight safety analysis of space launch vehicles	4
1.2 Survivability analysis of reentry debris.....	6
1.2.1 Survivability analysis program of foreign countries	8
1.3. Research topics of the paper.....	11
CHAPTER 2. DEVELOPMENT OF FLIGHT SAFETY ANALYSIS PROGRAM (FSAS).....	17
2.1 Fragment impact footprint.....	17
2.1.1 Impact predictor	17
2.1.2 Impact uncertainty model of fragment	18
2.2 Expected casualty	26
2.3 Sheltering model	28
2.3.1 Fragment sheltering model.....	28
2.3.2 Population sheltering model.....	31
2.4 Program validation	34
CHAPTER 3. DEVELOPMENT OF SURVIVABILITY ANALYSIS PROGRAM FOR ATMOSPHERIC REENTRY (SAPAR)	39
3.1 SAPAR Module	39
3.1.1 Trajectory module.....	40
3.1.2 Aerodynamics module	41
3.1.3 Aerothermodynamics module.....	45
3.1.4 Thermal module	57
3.1.5 Ablation module	60
3.2 Program validation	61

3.2.1 Comparison with ORSAT and SCARAB analysis on simple-shaped objects.....	61
3.2.2 Comparison with actually recovered space debris	66
CHAPTER 4. FLIGHT SAFETY ANALYSIS ON THE UPPER STAGE OF A LAUNCH VEHICLE	71
4.1 Launch vehicle configuration and trajectory.....	71
4.1.1 Main mass characteristics.....	71
4.1.2 Mission definition and sequence	72
4.1.3 Flight trajectory and parameters.....	73
4.1.4 Population near trajectory	79
4.2 Conditions for flight safety analysis.....	81
4.2.1 Debris model	81
4.2.2 Statistical Analysis	84
4.2.3 Wind profile of Australia	85
4.3 Flight safety analysis on the upper stage.....	92
4.3.1 Survivability analysis	92
4.3.2 Expected casualty analysis	102
4.3.3 Parametric study	110
CHAPTER 5. CONCLUSIONS	120
BIBLIOGRAPHY	124
국문초록.....	130
감사의 글.....	132

List of Tables

List of Tables

Table. 1 Variables in equation for population sheltering model [41]	32
Table. 2 Population sheltering model for Australia.....	33
Table. 3 Drag coefficients for various object shapes and flow regimes	45
Table. 4 Area-averaged heat ratios for various object shapes and flow regimes.....	51
Table. 5 Physical properties of spheres for code validation [25]	62
Table. 6 Physical properties of cylinders ($L/D=2$) for code validation [25]	63
Table. 7 Material properties of objects for code validation [25]	64
Table. 8 Initial conditions of simulation.....	64
Table. 9 Mass characteristics of the launch vehicle	72
Table. 10 Mission condition of the launch vehicle.....	73
Table. 11 Flight event sequence of the launch vehicle	73
Table. 12 Debris model of the upper stage of the launch vehicle	82
Table. 13 Material properties [25, 26].....	83
Table. 14 Debris model of the upper stage of the launch vehicle	103

List of Figures

Fig.1.1 Debris impact dispersion model [14].....	5
Fig.1.2 General Risk analysis Procedure [14].....	6
Fig.1.3. Delta II 2nd stage (top), with typical re-entry survivor objects, retrieved in South Africa in 2000 (center row), and retrieved in the central USA in 1997 (bottom row) [18].....	7
Fig.1.4. SCARAB geometric model of a spacecraft fragment, just before thermal fragmentation [32].....	10
Fig.1.5 Flight safety analysis procedure	16
Fig.2.1 Simple L/D impact distribution model	24
Fig.2.2 Bivariate normal density function.....	27
Fig.2.3 Casualty areas due to penetration of debris hitting a wood roof [14]	29
Fig.2.4 Casualty areas due to penetration of debris hitting a light metal roof [14].....	30
Fig.2.5 Casualty areas due to penetration of debris hitting a composite roof [14].....	30
Fig.2.6 Casualty areas due to penetration of debris hitting a reinforced concrete roof [14].....	31
Fig.2.7 Fragment footprints (3σ) by failures of the sample launch vehicle	36
Fig.2.8 Expected Casualty ($\log_{10}(E_c/\text{km}^2)$) by FSAS	37
Fig.2.9 Expected Casualty($\log_{10}(E_c/\text{km}^2)$) by TumCor.....	37
Fig.2.10 Comparison of E_c values of sample launch vehicle for latitudes by TumCor and FASA codes	38
Fig.2.11 Comparison of E_c values of sample launch vehicle for longitudes by TumCor and FASA codes	38
Fig.3.1 Program module of SAPAR code	40
Fig.3.2 Sphere in continuum flow	43
Fig.3.3 Drag coefficient of sphere in transitional regime.....	44

List of Figures

Fig.3.4 Stagnation point Stanton number bridging function in transitional flow regime [19].....	47
Fig.3.5 Heat transfer rate distribution on the sphere [28]	50
Fig.3.6 Free-molecular flow ratios of heating on surfaces parallel to the flow to stagnation-point heating on a sphere of the same radius [45, 46]	52
Fig.3.7 Free-molecular flow ratios of average heating on the sides of a rotating crossflow cylinder to stagnation-point heating to a sphere of the same radius [45, 46]	52
Fig.3.8 Continuum flow ratio of average heating to the side of an end-on cylinder to stagnation-point heating to a sphere of the same radius.....	53
Fig.3.9 1-D heat conduction model of a sphere	57
Fig.3.10 Comparison of demise altitudes for spheres predicted by ORSAT [25] and SAPAR	65
Fig.3.11 Comparison of impact masses for cylinders predicted by SCARAB [25] and SAPAR	65
Fig.3.12 Comparison of demise altitudes for boxes predicted by SCARAB [25] and SAPAR	66
Fig.3.13 Temperature vs. time for Delta-II second stage cylindrical tank	69
Fig.3.14 Heat fluxes vs time for Delta-II second stage cylindrical tank	70
Fig.4.1 Launch vehicle PPI and IIP trajectory	74
Fig.4.2 Altitude above Earth ellipsoidal surface vs. flight time	75
Fig.4.3 Downrange vs. flight time	76
Fig.4.4 Velocity vs. flight time.....	76
Fig.4.5 Acceleration vs. flight time.....	77
Fig.4.6 Vehicle nominal and 3-sigma position (latitude)	78
Fig.4.7 Vehicle nominal and 3-sigma position (longitude)	78
Fig.4.8 Vehicle nominal and 3-sigma position (altitude)	79
Fig.4.9 Nominal and 3-sigma Velocity.....	79
Fig.4.10 Australia population density ($\log_{10}(\text{pop}/\text{km}^2)$) near IIP trajectory	80

List of Figures

Fig.4.11 Configuration of KSLV-I upper stage [57].....	81
Fig.4.12 Semi-major axes of debris footprint ellipses of all the fragment groups vs. number of simulation runs for 506 sec fail case.....	85
Fig.4.13 January wind profile of Australia.....	86
Fig.4.14 February wind profile of Australia.....	86
Fig.4.15 March wind profile of Australia.....	87
Fig.4.16 April wind profile of Australia.....	87
Fig.4.17 May wind profile of Australia.....	88
Fig.4.18 June wind profile of Australia.....	88
Fig.4.19 July wind profile of Australia	89
Fig.4.20 August wind profile of Australia.....	89
Fig.4.21 September wind profile of Australia.....	90
Fig.4.22 October wind profile of Australia	90
Fig.4.23 November wind profile of Australia	91
Fig.4.24 December wind profile of Australia.....	91
Fig.4.25 Altitude for KM case fragment vs. downrange for 505 sec fail case	92
Fig.4.26 Altitude for all fragment groups vs. downrange for 505 sec fail case	93
Fig.4.27 Velocity-altitude map of all fragment groups for 505 sec fail case.....	94
Fig.4.28 Surface temperatures for all fragment groups vs. altitude for 505 sec fail case	96
Fig.4.29 Mass of all fragment groups vs. altitude for 505 sec fail case	96
Fig.4.30 Demise factor of all fragment groups vs. altitude for 505 sec fail case	97
Fig.4.31 Heat flux of KM nozzle vs. time for various vehicle fail time and velocities (time in abscissa is shifted for the time of maximum heat flux to be zero)	98
Fig.4.32 Demise factor of KM nozzle vs. time for various vehicle fail time and velocities (time in abscissa is shifted for the time of maximum heat flux to be zero)	99
Fig.4.33 Heat flux of KM nozzle vs. altitude for various vehicle fail time and velocities (time in abscissa is shifted for the time of maximum heat flux to be zero)	100

List of Figures

Fig.4.34 KM nozzle velocity-altitude map for various vehicle fail time and velocities (time in abscissa is shifted for the time of maximum heat flux to be zero)	100
Fig.4.35 Altitude of KM nozzle vs. downrange from launch pad for various vehicle fail time and velocities (time in abscissa is shifted for the time of maximum heat flux to be zero).....	101
Fig.4.36 Demise factors of all fragment groups vs. initial velocity	102
Fig.4.37 Three-sigma impact areas of all fragment groups for 496~507 fail time with July wind profile in two second interval in case of not considering the demise of debris	104
Fig.4.38 Expected casualty distribution ($\log_{10}(Ec/km^2)$) of Australia by the launch vehicle failure in 496-507 sec with July wind profile not considering the demise of debris	105
Fig.4.39 Accumulated Ec in Australia vs. latitude by the launch vehicle failure in 496- 507 sec with July wind profile not considering the demise of debris	106
Fig.4.40 Three-sigma impact areas of all fragment groups with survivability analysis for 496~507 fail time with July wind profile in two second interval	107
Fig.4.41 Expected casualty distribution ($\log_{10}(Ec/km^2)$) of Australia by the launch vehicle failure in 496-507 sec with July wind profile considering the demise of debris	108
Fig.4.42 Comparison of accumulated Ec in Australia vs. latitude by the launch vehicle failure in 496-507 sec with July wind profile between the cases with and without SAPAR application	109
Fig.4.43 Accumulated Ec in Australia vs. latitude by the launch vehicle failure in 496- 507 sec using wind profiles from January to December with SAPAR application	111
Fig.4.44 Accumulated Ec in Australia vs. latitude by the launch vehicle failure in 496- 507 sec varying the maximum imparted velocity by explosion in three orthogonal direction with SAPAR application	113
Fig.4.45 Three-sigma impact areas of all fragment groups for 496~507 fail time with	

List of Figures

July wind profile in two second interval in case of the maximum imparted velocity by explosion in each three orthogonal direction of 200 m/s with SAPAR application.....	114
Fig.4.46 Expected casualty distribution ($\log_{10}(Ec/km^2)$) of Australia by the launch vehicle failure in 496-507 sec with July wind profile and maximum imparted velocity by explosion in each three orthogonal direction of 200 m/s with SAPAR application.....	115
Fig.4.47 Comparison of accumulated Ec in Australia vs. latitude by the launch vehicle failure in 496-507 sec with July wind profile between the cases of 160 and 165 degree launch azimuths with SAPAR application.....	116
Fig.4.48 Expected casualty distribution ($\log_{10}(Ec/km^2)$) of Australia by the launch vehicle failure in 496-507 sec with July wind profile with SAPAR application (launch azimuth =160 degree).....	117
Fig. 4.49 Comparison of accumulated Ec in Australia vs. latitude by the launch vehicle failure in 496-507 sec with July wind profile between the cases varying the stagnation heat flux factor.....	119

Chapter 1. Introduction

1.1 Flight safety analysis of space launch vehicles

A Launch of a space launch vehicle can pose hazards to people and property in the area near the launch pad and downrange area along the flight track in case of a flight failure. Because launch vehicles are operated in harsh surroundings such as extremely high vibration level, cryogenic temperature, and low vacuum etc. the failure probability of the launch vehicle flight is relatively high. The launch vehicle is launched with a large amount of propellant which can explode upon impacting the earth surface resulting in a disaster. Furthermore, because the launch vehicle travels long distance in high altitude, the resulting fragments from flight failures of launch vehicles can fall on wide area. Therefore the risk to the ground from the launch vehicle failure must be analyzed prior to the launch and efforts to lower the risk level should be made when the risk is determined to be excessive.

Most space faring nations established space regulations which stipulate risk standards for launches of space launch vehicles. Several U.S. Federal regulations (AFSPC MAN 91-710 [1], FAA part 417 [2]) allow risk standards of $3E-5$ for each hazard by falling debris, distant overpressure, and toxic material that results in a total allowable risk of $9E-5$. NASA NPR 8715.5 [3] and Australian Space Launch Agency (SLASO) [4] provide a casualty expectation (E_c) limit per mission of $1E-4$. Here the casualty expectation (E_c) is defined as the average number of casualties that can occur as a result of a launch if the launch were to be repeated thousands of times.

One of the major hazards is the potential impact of debris resulting from a failing launch vehicle that breaks up from an explosion, aerodynamic loads, or FTS (flight termination system) activation. In these cases, the impact probability distributions for impacting vehicle debris can be computed assuming the vehicle fails in a certain time interval with predetermined failure probability. Then the corresponding probabilities of

fragments impacting specified population centers and the expectation of casualties (E_c) for each center are computed. The total collective E_c (casualty expectation) by falling debris is computed by summing the above E_c values over the population centers and the flight time intervals.

1.1.1 The history of flight safety analysis of space launch vehicles

The flight safety analysis is thought to be most actively and widely researched in the U.S. Analyses of the risks associated with launch failures have been performed from the beginning of the development for launch vehicles in the U.S. [5, 6]. The analysis methods have progressed considerably from a period of ultra-conservativeness when the computations were conducted by hands with simplification to complex computer models which employed fragment trajectory simulations. The range safeties of Saturn rockets have been analyzed by NASA with the predefined flight failure rate, population density of the countries around the flight track, and the lethal area of the vehicle fragments assuming that the fragments would fall in a corridor of a certain width [7-9]. Their approach was as follows;

$$P_{IP} = \sum_n P_{I,n} \times \left[\frac{N}{L_A} \right]_n \times A_L \quad (1.1)$$

Where,

n : index for countries

P_{IP} : probability of injuring person

$P_{I,n}$: probability of impacting a certain country

$[N/L_A]_n$: population density of the country (/m²)

A_L : lethal area (m²)

Here, P_{IP} has the similar meaning to expected casualty (E_c), population density of the country ($[N/L_A]_n$) is the population per unit area of the countries within the

Chapter 1

fragment impact corridor around the flight track, and lethal area (A_L) is the area within which the public becomes a casualty by fragments. The probability of impacting a certain country ($P_{I,n}$) in the above equation was calculated by the following relation.

$$P_{I,n} = \frac{\Delta t_n}{T_B} \times P_F \quad (1.2)$$

Where,

Δt_n : dwell time of the impact point trace over a certain country

T_B : total burn time of the stage

P_F : probability of any failure causing the stage to drop short

In these analyses, all the fragments from a launch vehicle failure in a time interval were assumed to fall within a same area regardless of their sizes and ballistic coefficients.

In the U.S. eastern test range the flight safety analysts started to employ the concept of piece category [10] which is now called as the fragment group. They assigned the pieces to several categories on the basis of ballistic coefficient. All pieces in a category are assumed to have the same density function, namely they are assumed to have the same free fall characteristics, while the pieces of other categories fall on different areas with different density functions. They used this approach in the derivation of the ship hit probability contour. The probability of a piece category impacting a ship could be calculated using the impact probability density function of that category, the relative location of the ship from the mean impact point of the category, and the ship's effective area. In the later time, this approach using fragment groups became popular in the other flight safety analyses such as expected casualty analysis and aircraft hit probability analysis etc.

It is thought that the methodology with high fidelity has been first developed by Baker et al. [6]. Their method is being nowadays used in several U.S. federal launch sites, and is also adopted in the present research with some improvements. Although

they used several simplified models such as impact point interpolation, linear relation between fragment initial velocity and the impact points, etc, they calculated the impact distribution of each fragment group, computed the impact probability of each fragment group on each population center, and then analyzed expected casualty for the population center considering the sheltering level of the structure in which people reside. Baker et al. [6] employed five uncertainty models (1. vehicle state vector ($x, y, z, \dot{x}, \dot{y}, \dot{z}$) uncertainty, 2. destruct-induced velocity, 3. wind uncertainty, 4. fragment ballistic coefficient uncertainty, 5. fragment lift effect) to generate the impact distributions of fragment groups. The casualty expectation was analyzed based on these impact distributions, population model, and casualty areas of fragment groups. Here the casualty area is defined as an area around a debris impact point in which a person who is present will become a casualty in the event of that debris impact.

As the computing power improved, some simplification models in the methodology of Baker et al. were replaced by Monte Carlo simulation [11-13]. This improved methodology is being used in several U.S. federal ranges and almost becomes a standard procedure. Especially, U.S. FAA (Federal Aviation Administration) recently issued “Flight Safety Analysis Handbook, Ver1.0” [14] which adopt this methodology in order to help launch and reentry launch vehicle operators conduct flight safety analyses properly. Australian space launch agency (SLASO: Space Licensing and Safety Office) [4] also requires launch operators who plan to launch vehicles in launch sites in Australia to analyze the launch risk according to this methodology.

1.1.2 The procedure of flight safety analysis of space launch vehicles

The risk analysis starts with segmenting the vehicle trajectory into short time intervals. Hazards for each time interval are computed for each failure mode of the vehicle by assuming that the failure occurred at a representative time within the interval. The probability density function of fragment impact is produced for each vehicle fragment group resulting from the failure of each failure mode. The impact

Chapter 1

distributions are calculated accounting for the effects of destruct or explosion-induced velocities, vehicle guidance and performance error, and uncertainties in effects by wind, drag, and aerodynamic lift etc. The impact probability of each fragment group on each population center is calculated using this impact probability density distribution, the area of the population center, and relative location between the population center and the mean impact point of the fragment group. The casualty expectation for each center is computed based on the fragment probability of impact, fragment casualty area, and the population density of the population center [6].

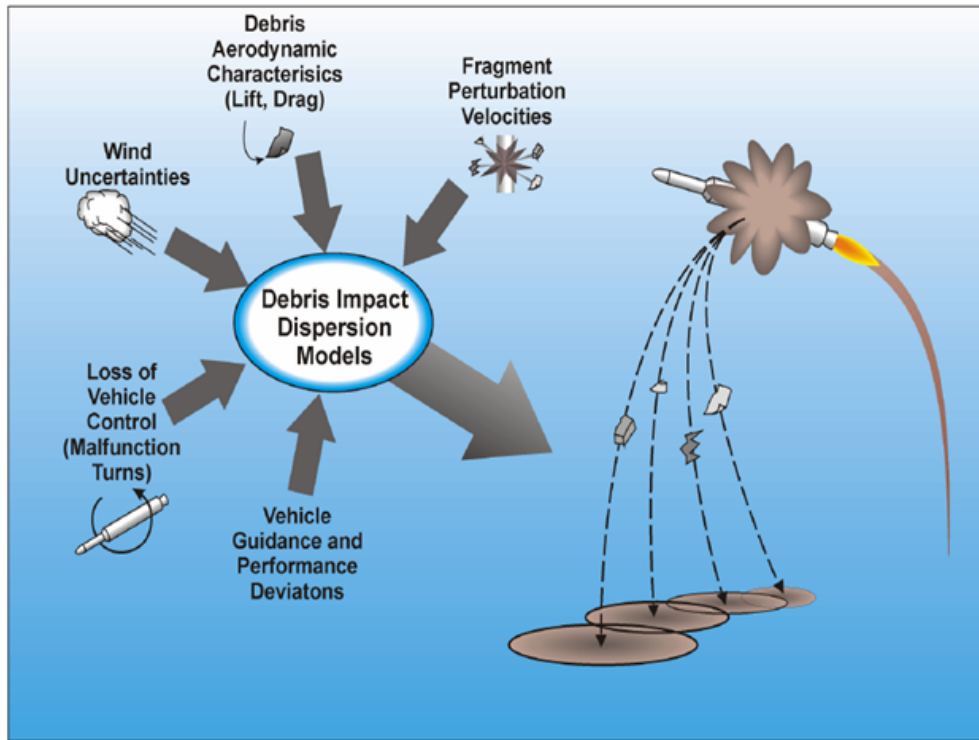


Fig.1.1 Debris impact dispersion model [14]

The casualty expectations for each time interval and failure mode are weighted by the probability that the particular failure mode will occur during the time interval. The total casualty expectation is computed for all critical centers by combining the

weighted results for all failure times, failure modes, and impacting fragment groups. The spacing of the successive failure times for the analysis is made to be close so that the successive impact distribution areas for fragment groups overlap sufficiently to form the actual continuous distribution [4, 6].

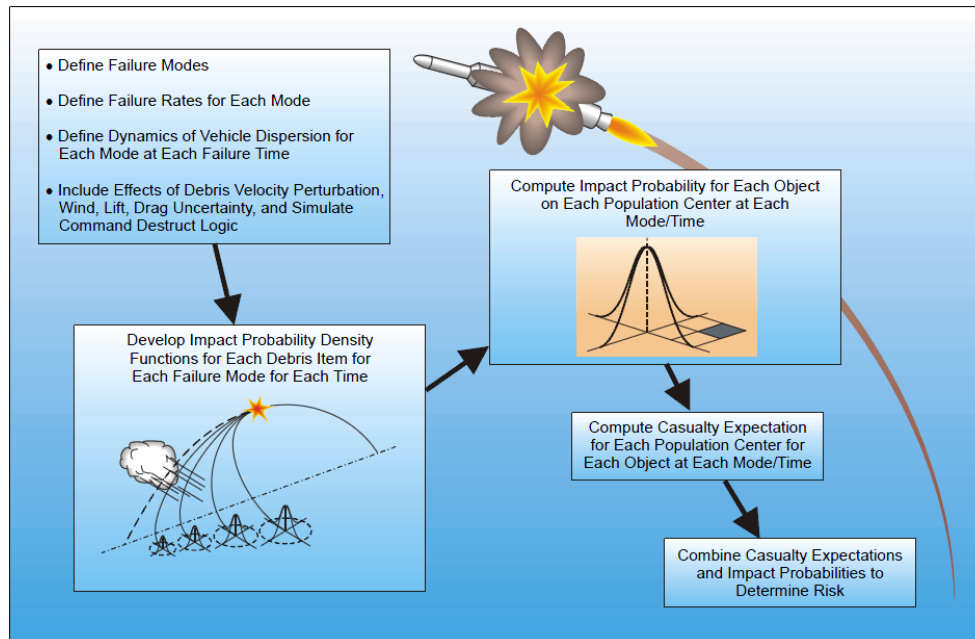


Fig.1.2 General Risk analysis Procedure [14]

1.2 Survivability analysis of reentry debris

After the launch of Sputnik satellite in 1957, more than 19,000 artificial objects have returned to Earth [15]. It was suggested that 10% to 40% of the mass of larger objects may survive the severe structural and thermal loads during atmospheric reentry [16]. Actually, three pieces of debris with total weight of 325 kg from upper stage of US Delta-II rocket have impacted the earth, which were about 35% of the initial weight of 920kg [17, 18]. Figure 1.3 shows recovered debris from the second stage of Delta-II rocket.

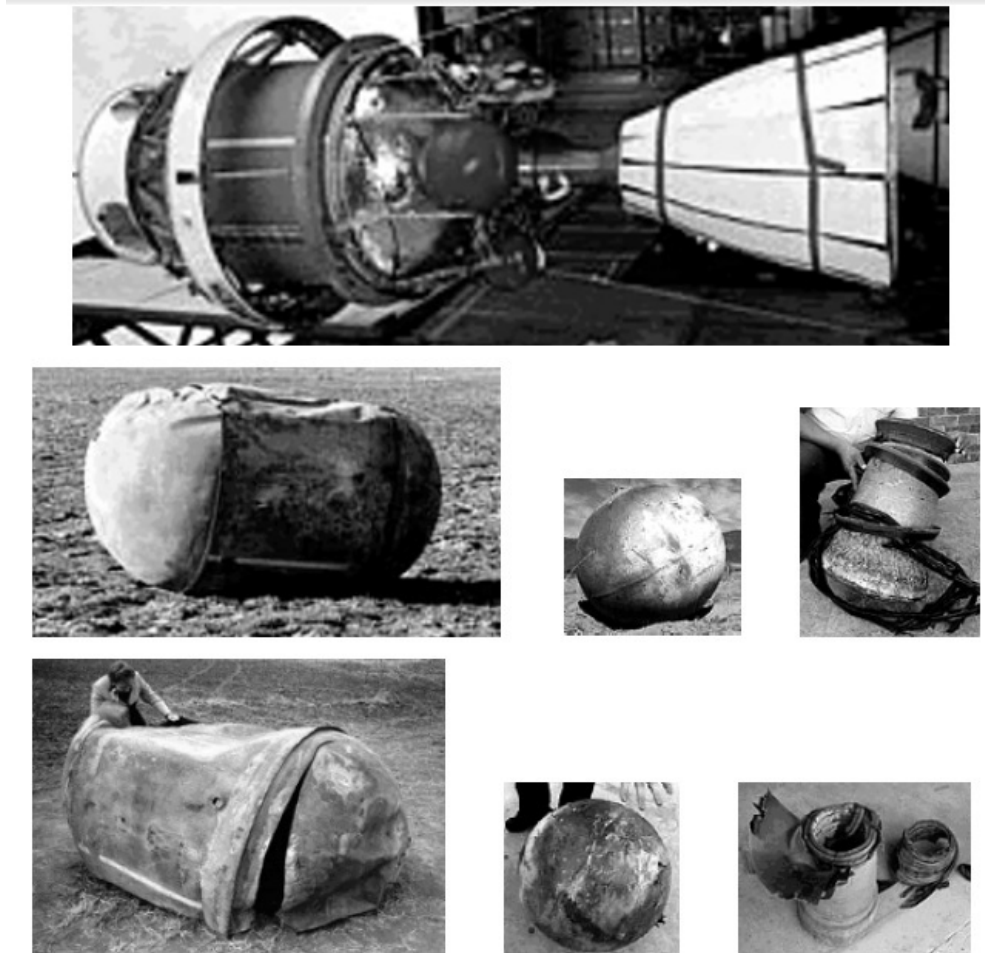


Fig.1.3. Delta II 2nd stage (top), with typical re-entry survivor objects, retrieved in South Africa in 2000 (center row), and retrieved in the central USA in 1997 (bottom row) [18]

Analysis of the risk from orbital debris reentering the Earth has become an important topic in recent years [19, 20] because these space debris which survive the reentry can pose risks to the ground. Several national organizations from the space-faring nations have established the Space Debris Mitigation Standards and Handbooks that stipulate risk standards for debris that survives reentry [21]. Tools with which to

analyze the survivability of reentry objects, and thus determine the potential ground risk from the objects, have been developed by several space agencies and research institutes.

1.2.1 Survivability analysis program of foreign countries

Europe, Japan, Russia, China and the United States have developed the computer codes to model in detail the fragmentation and eventual demise of space debris during reentry, taking into account both the thermal and dynamical aspects [22, 23, 24, 33, 34]. In practice, these tools are used to determine whether satellites or the upper stages of launch vehicles comply with the human casualty risk standards. The codes analyze the casualty areas from the surviving debris and then the casualty risks are simply computed by using the average population density in the belt potentially affected by the satellite debris impact which can be determined by the inclination angle of the satellite and the year of reentry [62].

Among these tools, Spacecraft Atmospheric Re-entry and Aerothermal Breakup (SCARAB) [22] by ESA (European Space Agency) and the Object Reentry Survival Analysis Tool (ORSAT) [23, 24] by NASA (National Aeronautics and Space Administration) can provide high fidelity simulation results, and have been widely used over the last decade. Although they adopt different approaches for trajectory simulation and the calculation of drag coefficients and heating rates, both tools have shown good agreement when analyzing objects with simple shapes [25]. These codes haven't been open to the public and the uses of the codes are restricted to their inner circles. Therefore, in order for a country to analyze the survivability of the orbital debris, it should develop its own program and that is the reason why a survivability analysis code was researched in the present paper.

1.2.1.1 United States

Chapter 1

U.S. NASA has two kinds of survivability analysis program; DAS (Debris Assessment Software) [26] and ORSAT. DAS was developed in 1998 by Lockheed utilizing the simplified models to generate conservative risk results. The current version is Ver. 2.0. ORSAT was developed mainly by JSC (Johnson Space Center). The first version (Ver. 4.0) presented in literature was developed in 1993. The program has been upgraded to Ver. 5.0 (1999), Ver. 5.8 (2003), and Ver. 6.0 (2005) [27, 28].

The more realistic ORSAT code simulates the reentry process by integrating software modules for integrated trajectory, atmospheric, aerodynamic, aerothermodynamic and thermal modules. The drag coefficient is calculated in aerodynamic module using object type, object motion (spinning, tumbling etc.), and flow regime and used to simulate the trajectory of debris in trajectory module. In aerothermodynamics module, heating rates for an object are computed utilizing velocity and geometry of the object, Stanton No., and Knudsen No etc. The thermal module computes the temperature of the object using a lumped mass model or a 1-D heat conduction model. After the melting temperature is reached, the net heat absorbed into the object or outer layer was tracked. If the absorbed heat exceeds the material heat of ablation, the object is assumed to demise.

ORSAT has been used as a primary tool by NASA to assess the casualty areas of orbital objects over the past decade [28]. Frequently, ORSAT has been used for a higher fidelity survivability analysis when the NASA DAS (Debris Assessment Software), which generates conservative risk results by relatively simple approach, has raised an issue that a spacecraft might be unable to meet the safety standard. If an uncontrolled orbital object during reentry is predicted by ORSAT to have risk greater than the human casualty risk criteria, controlled reentries or retrievals using other vehicles must be considered at great additional cost in NASA [29]. ORSAT is originally a survivability analysis code while the human casualty risk is simply computed by using the survivability analysis results and the average population density around the ground track of the space craft.

1.2.1.2 Europe

NASA ORSAT is a kind of object-oriented code which analyzes individual simple-shaped parts of reentered satellites or the upper stages of launch vehicles. On the contrary, the SCARAB (Spacecraft Atmospheric Re-Entry and Aerothermal Breakup) software system of ESA (European Space Agency) is a spacecraft-oriented code that can model the complete spacecraft as one consistent object [18]. Aerodynamic and aerothermodynamic coefficients are calculated for the real, complex geometric shape, and not only for simplified object shapes. Breakup events are computed by analyzing the actually acting structural and thermal loads. Shadowing and protection of spacecraft parts by others are taken into account. At present, SCARAB is the only spacecraft-oriented code. SCARAB has been developed by HTG (Hypersonic-Technologie Gottingen) within the frame of several ESA/ESOC contracts [19]. Figure 1.4 shows the geometric model of a spacecraft just before thermal fragmentation in SCARAB [32].

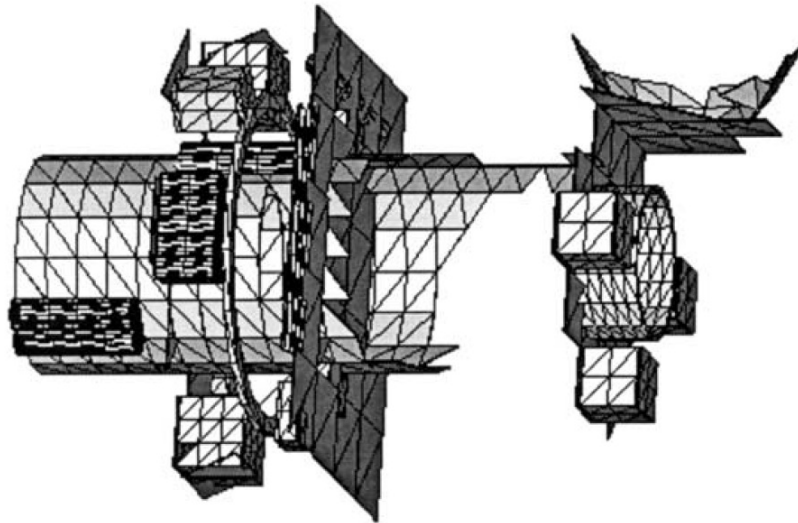


Fig.1.4. SCARAB geometric model of a spacecraft fragment, just before thermal fragmentation [32]

Chapter 1

1.2.1.3 Japan

Japan has a survivability analysis code named ORSAT-J which is a modified version of the NASA ORSAT (version 4.0) [19]. Compared to the NASA ORSAT, ORSAT-J is basically limited to the lumped thermal mass model without partial melting. Drag coefficient and convective aeroheating are the same as in ORSAT.

1.2.1.4 China

China recently developed an object-oriented tool i.e. debris reentry and ablation prediction system (DRAPS) [33, 34]. DRAPS has analysis approach similar to that of NASA's ORSAT. This program extends object shapes up to 15 types while NASA's ORSAT can analyze 4 types. In addition, a simple Monte Carlo method has been taken into account for uncertainties in initial conditions, atmospheric models, and aerodynamic models and subsequently reentry risk is assessed in a probabilistic manner [34]. The results presented in the paper [34] showed some discrepancies about demise altitudes for reentering debris of SPARTAN spacecraft compared with the analysis by ORSAT.

1.3. Research topics of the paper

Although Korean space law does not request that the launch operator in the country should submit the expected casualty analysis results to the government, it is thought to be appropriate to prove the risk by launch vehicles developed and launched in Korea are in the same level as the ones of other countries. To this end, an analysis program named 'Flight Safety Analysis System (FSAS)' was developed to compute the expected casualty of launch vehicles developed in Korea because the higher fidelity programs for flight safety analysis which employ the general procedures explained in the above

sections haven't been open to the public. The procedure was adopted from the methods suggested by Baker et al [6] and the improvements regarding the Monte Carlo simulation on fragment trajectory based on several uncertainties were added as in other researches [11-13]. The code was validated by comparing the analysis results with those of TumCor program [4, 14] from ACTA(Inc) in USA.

The launch vehicle operators of space faring nations are generally required to evaluate launch hazards to determine if the risks for a particular launch mission are within acceptable limits specified in the space regulations. If the risks are computed to exceed the limit, the launch may be postponed, a revised trajectory and launch vehicle configuration may be required, or high-risk locations may be partially or wholly evacuated. These additional activities can cause great rises in development or launch cost for a launch vehicle.

The risk analyses inevitably contain uncertainties that result from a lack of complete information of the mechanisms over the vehicle failure and the consequential effects. For this reason, the space regulations state that the assumptions for analyses shall be conservative whenever ambiguities exist in the analysis procedure. In such a case, the analyses produce the results that overestimate the risks of the mission due to conservative assumptions over several uncertainties. Therefore, if the analysis methodology becomes more realistic by removing the uncertainties in the procedure, the more accurate calculation is possible, resulting in a lower expected casualty prediction. So, flight safety analysts are required to make every effort to minimize uncertainties using the most appropriate methods which is physically reasonable. And in some cases, the accurate analysis may result in reduction of development or launch cost by excluding the additional activity to reduce risk factors.

Up to now, the flight safety analyses for launch vehicles have been conducted assuming the falling debris impact the earth surface without any mass loss due to ablation or melting even for the case with very high reentry speed. This approach leads to conservative risk predictions and has been widely accepted in flight safety analysis. However, when the vehicle fails at very high velocity, the fragments should undergo a

Chapter 1

large amount of heat load resulting in partial or full ablation. This would reduce the ground risk compared with the analysis using the assumption of no ablation especially when the people are under some protection by a degree of sheltering level. Therefore, if a flight safety analyst accounts for the melting or ablating process of debris in the flight safety procedure, he/she can make a more accurate analysis that necessarily results in lowered expected casualty result.

In this light, a survivability analysis program for atmospheric reentry named SAPAR(Survivability Analysis Program for Atmospheric Reentry) [35] was developed in the present research in order to be included in the flight safety analyses of launch vehicles. The SAPAR code simulates the reentry process by integrating software modules for integrated trajectory, atmospheric, aerodynamic, aerothermodynamic and thermal analysis. The SAPAR trajectory module simulates a three degree-of-freedom (DOF) trajectory by integrating the equations of motion in terms of the ECI (Earth Centered Inertial) frame accounting for the Earth and atmosphere model. The aerodynamic module computes average drag coefficients of objects within free molecular, transitional, and continuum flow regimes as function of Knudsen number. The heat fluxes to reentry objects such as convective heat flux, oxidation heat flux, and reradiation heat loss are computed in the aerothermodynamics module. The thermal module computes the temperature of the object using a nodal thermal math model. The demise of an object is determined when the absorbed heat exceeds the heat of ablation of the object.

SARAR is a kind of object oriented code that uses an approach and equations similar to those of ORSAT. However, because the analysis of ORSAT on actually recovered space debris of cylindrical tank showed some discrepancies compared with the experimental analysis [16], the cause of the discrepancy was investigated and improvements about reradiation heat loss of a metallic hollow cylinder were made in this study [35]. The SAPAR code was validated by comparing the survivability analysis results on simple-shaped objects with those of ORSAT and SCARAB [25]. In addition, the analyses on the actually recovered cylindrical tank were compared with the

measured data and showed good agreement after improvements on the reradiation heat loss of a cylindrical tank compared with the approach of ORSAT [35]. Although the SAPAR code has been developed to be used in the flight safety analysis of launch vehicles, it can also be utilized in the risk analysis of space satellites reentering the Earth's atmosphere after mission termination like other survivability analysis programs such as DAS, ORSAT and SCARAB.

The ultimate subject of this research is to analyze the flight safety of a launch vehicle flying at high velocity with the consideration of the reentry process of the debris including melting or ablation for more accurate analyses. For this end, the SAPAR code was put into the FSAS code in the procedure of trajectory simulation of falling debris. FSAS takes Monte Carlo simulations on the fragment trajectory until it reaches the Earth surface to determine the impact point distribution area. Survivability analysis was employed in this trajectory simulation when the object altitude was above 20 km. Below this altitude, only typical 3-dof simulations on falling of the objects were conducted because the objects were decelerated to about several hundred meters per second and the aerodynamic heating became negligible. The resulting combined procedure for the flight safety analysis developed in this paper is depicted in Fig. 1.5.

This paper is organized as follows. Firstly, the flight safety analysis code (FSAS) and survivability analysis code (SAPAR) are explained in Chapter 2 and Chapter 3 with details of modules and validation of the results. The main contribution of this study is in Chapter 4, in which FSAS and SAPAR codes are combined and the flight safety analyses on the upper stage of a launch vehicle are conducted and the effect of considering the demise of debris on the expected casualty is investigated. In addition, analyses by the developed program with various conditions such as wind profile, the IIP trajectory, and explosion velocity are conducted. Here, IIP (Instantaneous Impact Point) is defined as the impact point, following thrust termination of a launch vehicle with or without atmospheric drag effects. The launch vehicle analyzed in this paper has a 2-stage configuration like Korea Space Launch Vehicle-I (KSLV-I). The First stage is powered by liquid propellant rocket engine that uses kerosene and liquid oxygen while

Chapter 1

second stage adopts solid propellant kick motor. Finally, the conclusions are given in Chapter 5.

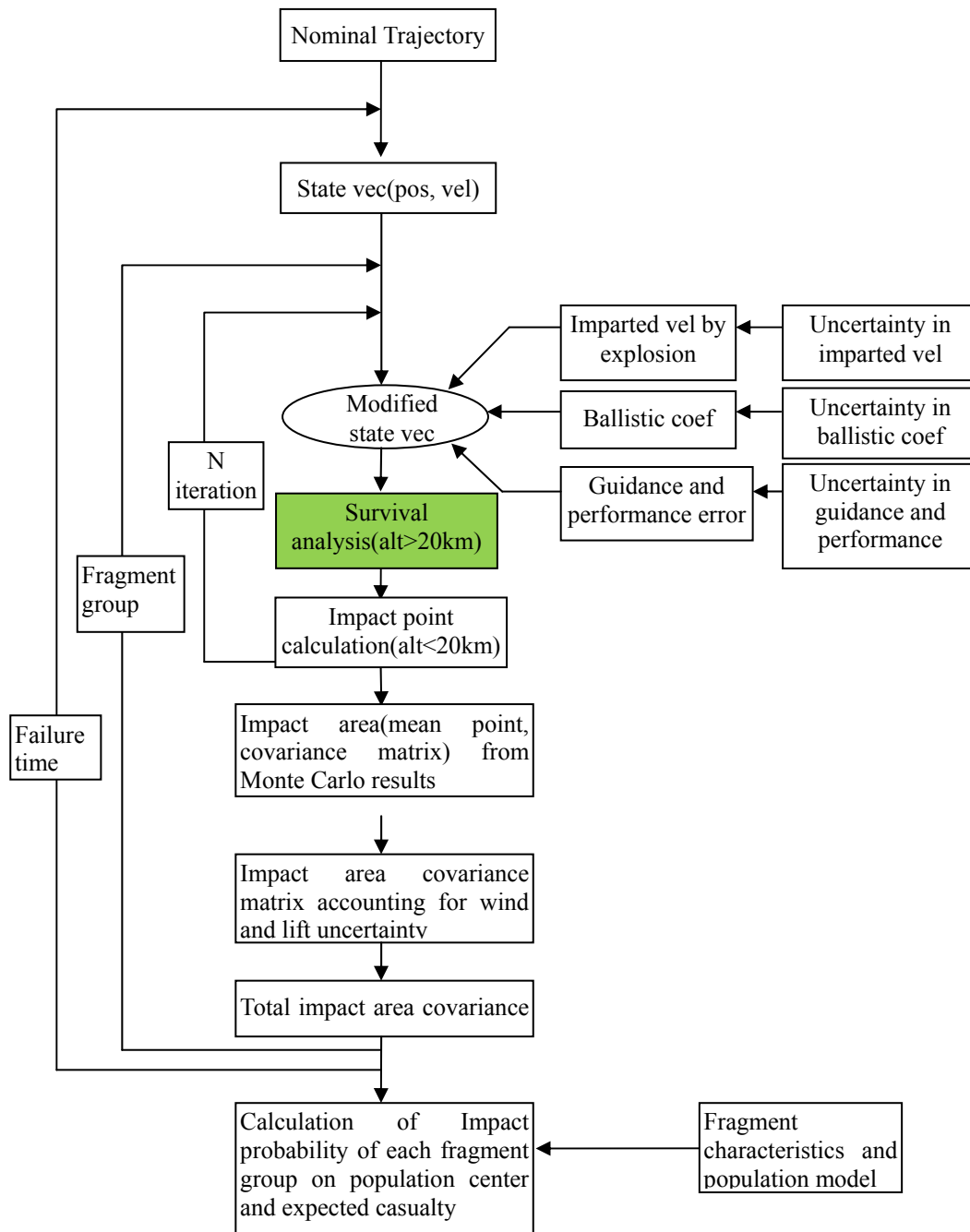


Fig.1.5 Flight safety analysis procedure

Chapter 2. Development of Flight Safety Analysis Program (FSAS)

2.1 Fragment impact footprint

The flight safety analysis of a launch vehicle is accomplished by segmenting the flight trajectory according to flight time by a certain interval i.e. 1 sec. Impact distributions of vehicle fragments are calculated assuming the vehicle fails in a certain representative time within a time interval. The impact points are strongly affected by the initial state vector $(x, y, z, \dot{x}, \dot{y}, \dot{z})$, fragment aerodynamic characteristics, and wind effects etc. Because these factors have uncertainties in their nature, a statistical approach using impact distribution area or footprint concept is used in the analysis. The debris footprint is the statistical region defining the scatter of debris resulting from a breakup at a specific point in time at a specific point in space.

Figure 1.1 illustrates the impact footprints of debris due to uncertainty sources. Although only four pieces of debris are shown in the figure, actually there can be thousands of fragments. In order to simplify the modeling process and to reduce the computing time, debris pieces are generally grouped into “fragment groups” consisting of fragments having similar characteristics such as size and ballistic coefficient. Mean impact points and standard deviations of impact footprints of fragment groups are computed based on the above uncertainty sources using Monte Carlo methods or by propagating state vector uncertainty which is expressed as a covariance matrix using linear relationships.

2.1.1 Impact predictor

An impact predictor uses a state vector to define the initial metric conditions and

Chapter 2

computes an impact point on the surface of the Earth. For flight safety, the impact predictor must account for elliptical rotating earth model, gravity model, atmosphere model, and wind model. For impact prediction, a 3-dof simulation that integrates the equations of motion in ECI (Earth Centered Inertial) frame was used in this research. WGS84 (World Geodetic System 84) [36] was used as the Earth model and US Standard 1976 model [37] or the GRAM95 (NASA/MSFC Global Reference Atmospheric Model-1995) [38] was used as the atmosphere and wind model. The differential equations for 3-dof simulation in ECI frame is as follows.

$$\frac{d}{dt} \vec{r} = \vec{v} \quad (2.1)$$

$$\frac{d}{dt} \vec{v} = \vec{g}(\vec{r}) + \vec{a}(\vec{r}, \vec{v}) \quad (2.2)$$

Where,

\vec{r} : position vector in ECI frame (m)

\vec{v} : velocity vector in ECI frame (m/s)

\vec{g} : acceleration by Earth gravity (m/s²)

\vec{a} : acceleration by aerodynamic force including wind effects (m/s²)

t : time (sec)

The impact point in latitude and longitude can be given by coordinate transformation from ECI to LLH (Latitude, Longitude, and Height) frame.

2.1.2 Impact uncertainty model of fragment

2.1.2.1 Fragment imparted velocity from explosion

Imparted velocities that fragments might receive from a vehicle explosion or pressure rupture have a significant effect on impact points of the fragments. Fragment

velocity perturbations by explosion are defined usually based on the specified maximum expected magnitude. A tri-variate normal distribution for velocity perturbation with equal standard deviations along all three axes and no correlation is assumed. This leads to a Maxwellian probability distribution regarding the magnitude and a random distribution about direction. In the Monte Carlo process, randomly selected velocity perturbation magnitudes along each three orthogonal direction are added to the original fragment velocity and the trajectories are computed to the ground for each new state vector. Then the impact points from the trajectories are compiled and a covariance matrix for each fragment group in an East-North coordinate system are computed. Maximum imparted velocity by explosion is assumed as 100 meter per second in each three orthogonal direction in this research.

2.1.2.2 Uncertainty in ballistic coefficient

The drag effect during free-fall is characterized by the size, mass and shape of each fragment. The parameter that specifies the atmospheric effect is the ballistic coefficient which is defined as a mass divided by drag coefficient and reference area ($\beta = \frac{m}{C_d \cdot A}$, m =mass (kg), C_d =drag coefficient, A =reference area (m^2)). Because fragment group represents a set of actual fragments, the group does not have a unique ballistic coefficient (β), instead it has a range of values and uncertainty in the original selection of ballistic coefficient (β). It can be assumed that the ballistic coefficient has a lognormal distribution since it is calculated by multiplying several random variables [11, 14]. In the Monte Carlo process, randomly selected ballistic coefficients from lognormal distribution were used to compute the impact points. The impact points from the simulations are compiled and covariance matrixes in an East-North coordinate system are computed.

2.1.2.3 Guidance and performance uncertainty

Chapter 2

A launch vehicle can fly a deviated trajectory within the normal range because of the uncertainties in performance of rocket engine and various control devices and variations in the atmospheric environments. Uncertainties in a launch vehicle's guidance and performance make uncertainty in the state vector of a vehicle at the time of failure. These trajectories are generally referred to as 3-sigma trajectories and provided by the vehicle manufacturer. The state vector uncertainty produces dispersions in the locations of the debris during free fall and at impact. The effects by guidance and performance uncertainty on impact distributions were considered also by a Monte Carlo method in this research. In the Monte Carlo process, statistically selected state vectors from the 3-sigma trajectory were used to compute the impact points. The impact points from the simulations are compiled and covariance matrixes in an East-North coordinate system are computed.

2.1.2.4 Effects of wind

The strength of the wind is also an external source of uncertainty during free-fall. The wind dispersion effect was considered by computing the time a fragment falling at terminal velocity through an altitude band and assuming the fragment travels laterally at the velocity of the wind. This assumption implies that the fragment would be imbedded in the wind, which is quite accurate for low ballistic coefficient debris and becomes less accurate as the ballistic coefficient increases. For the case of typical vehicle fragments that have ballistic coefficients of about $100 \sim 200 \text{ (kg/m}^2\text{)}$ and are falling from 20 km altitude, this assumption makes about 10 ~ 20% error in impact point compared with the actual integration of the equation of motion accounting for the wind effect. In addition, the wind uncertainty is not a main source in the impact uncertainty for the fragments of upper stage of a launch vehicle that fails in very high altitude and velocity, so the above assumption does not have significant effects on the final expected casualty result of this study.

With the assumption that the fragments would travel laterally at the velocity of the wind while they fall at terminal velocity, the impact uncertainty by wind can be given very simply without using any Monte Carlo simulations. First, segment the altitude into n bands as follows;

$$\Delta H_j = H_{j+1} - H_j, j = 1, 2, \dots n$$

Where,

ΔH_j = altitude band

H_j, H_{j+1} = altitude limits of j^{th} altitude band

n = number of altitude bands

The final falling velocity of each fragment in each altitude band is calculated as follows;

$$V_{T,i,j} = \sqrt{\frac{2\beta_i \cdot g}{(\rho_{j+1} + \rho_j) / 2}} \quad (2.3)$$

Where,

$V_{T,i,j}$ = terminal velocity of i^{th} fragment group in j^{th} altitude band (m/s)

β_i = ballistic coefficient of i^{th} fragment group (kg/m^2)

g = acceleration of gravity (m/s^2)

$(\rho_j + \rho_{j+1})/2$ = average air density in j^{th} altitude band (kg/m^3)

The time of i^{th} fragment group falling at terminal velocity through j^{th} altitude band is given by;

$$\delta t_{i,j} = \frac{\Delta H_j}{V_{T,i,j}} \quad (2.4)$$

Where,

$\delta t_{i,j}$ = time needed for i^{th} fragment group to fall j^{th} altitude band (sec)

Chapter 2

The distance traveled by i^{th} fragment group laterally through all the altitude bands is computed as follows [14];

$$\begin{bmatrix} E_i \\ N_i \end{bmatrix} = \begin{bmatrix} \delta t_{i,1} & \delta t_{i,2} & \dots & \delta t_{i,n} & 0 & 0 & \dots & 0 \\ 0 & 0 & \dots & 0 & \delta t_{i,1} & \delta t_{i,2} & \dots & \delta t_{i,n} \end{bmatrix} \begin{bmatrix} W_{E1} \\ W_{E2} \\ \vdots \\ W_{En} \\ W_{N1} \\ W_{N2} \\ \vdots \\ W_{Nn} \end{bmatrix} \quad (2.5)$$

Where,

E_i : distance traveled laterally in eastern direction by i^{th} fragment group during free fall (m)

N_i : distance traveled laterally in northern direction by i^{th} fragment group during free fall (m)

W_{Ej} : wind velocity in eastern direction in j^{th} altitude band (m/s)

W_{Nj} : wind velocity in northern direction in j^{th} altitude band (m/s)

The covariance matrix for impact distribution of i^{th} fragment group by wind uncertainty can be expressed as the matrix product in East-North coordinates;

$$\begin{bmatrix} \sigma_E^2 & \sigma_{EN} \\ \sigma_{EN} & \sigma_N^2 \end{bmatrix}_i = \begin{bmatrix} \delta t_{i,1} & \dots & \delta t_{i,n} & 0 & \dots & 0 \\ 0 & \dots & 0 & \delta t_{i,1} & \dots & \delta t_{i,n} \end{bmatrix} \Sigma_W \begin{bmatrix} \delta t_{i,1} & \dots & \delta t_{i,n} & 0 & \dots & 0 \\ 0 & \dots & 0 & \delta t_{i,1} & \dots & \delta t_{i,n} \end{bmatrix}^T \quad (2.6)$$

Where,

σ_E^2, σ_N^2 : impact points variances in east and north directions by wind (m^2)

σ_{EN} : impact point covariance by wind (m^2)

Σ_W : wind covariance matrix

$$\Sigma_W = \begin{bmatrix} \sigma_{WE_1}^2 & \sigma_{WE_1E_2} & \cdot & \sigma_{WE_1E_n} & \sigma_{WE_1N_1} & \sigma_{WE_1N_2} & \cdot & \sigma_{WE_1N_n} \\ \sigma_{WE_2E_1} & \sigma_{WE_2}^2 & \cdot & \sigma_{WE_2E_n} & \sigma_{WE_2N_1} & \sigma_{WE_2N_2} & \cdot & \sigma_{WE_2N_n} \\ \cdot & \cdot & \cdot & \cdot & \cdot & \cdot & \cdot & \cdot \\ \sigma_{WE_nE_1} & \sigma_{WE_nE_2} & \cdot & \sigma_{WE_n}^2 & \sigma_{WE_nN_1} & \sigma_{WE_nN_2} & \cdot & \sigma_{WE_nN_n} \\ \sigma_{WN_1E_1} & \sigma_{WN_1E_2} & \cdot & \sigma_{WN_1E_n} & \sigma_{WN_1}^2 & \sigma_{WN_1N_2} & \cdot & \sigma_{WN_1N_n} \\ \sigma_{WN_2E_1} & \sigma_{WN_2E_2} & \cdot & \sigma_{WN_2E_n} & \sigma_{WN_2N_1} & \sigma_{WN_2}^2 & \cdot & \sigma_{WN_2N_n} \\ \cdot & \cdot & \cdot & \cdot & \cdot & \cdot & \cdot & \cdot \\ \sigma_{WN_nE_1} & \sigma_{WN_nE_2} & \cdot & \sigma_{WN_nE_n} & \sigma_{WN_nN_1} & \sigma_{WN_nN_2} & \cdot & \sigma_{WN_n}^2 \end{bmatrix} \quad (2.7)$$

2.1.2.5 Effects of lift

Debris can experience a lift force perpendicular to its direction of motion during free-fall. Lift effects on falling debris can only be approximated because the magnitude of the lift force fluctuates as the fragment tumbles and the motion of the fragment cannot be defined exactly. In this research, the lift uncertainty is estimated using a lift-to-drag coefficient which is specified as inputs for fragment groups. The debris impact distribution due to lift can be calculated assuming the debris falls in dynamic equilibrium state as in Fig. 2.1. [12, 14];

$$D \sin \alpha = L \cos \alpha \quad (2.8)$$

$$\alpha = \tan^{-1} \left(\frac{L}{D} \right) \quad (2.9)$$

$$d = h \times \tan \alpha = h \times \left(\frac{L}{D} \right) \quad (2.10)$$

Hence,

$$\sigma_d = h \times \sigma_{L/D} \quad (2.11)$$

The covariance matrix is expressed as follows in Earth-North coordinate;

$$\begin{bmatrix} \sigma_E^2 & \sigma_{EN} \\ \sigma_{EN} & \sigma_N^2 \end{bmatrix}_{lift} = \begin{bmatrix} \sigma_d^2 & 0 \\ 0 & \sigma_d^2 \end{bmatrix} \quad (2.12)$$

It can be seen that the impact distribution due to lift is in a circular shape. Three

Chapter 2

object $\sigma_{L/D}$ values are assigned in this paper based on an Apollo debris reentry lift study as follows [14];

$\sigma_{L/D}=0.01$ for box objects

$\sigma_{L/D}=0.05$ for tumbling flat objects

$\sigma_{L/D}=0.03$ for objects neither flat nor boxy

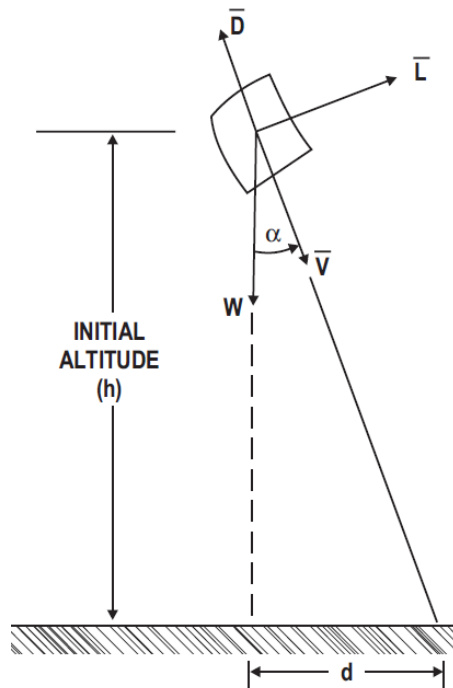


Fig.2.1 Simple L/D impact distribution model

2.1.2.6 Combination of Covariance Matrices

The mean impact point can be computed assuming that the fragments have zero imparted velocity, average ballistic coefficient of each fragment group, zero guidance and performance error, average wind profile, and zero lift effect. Because the uncertainty sources considered in the above sections are independent of each other, the

total impact covariance matrix in East-North coordinate can be computed as follows [12, 14];

$$\Sigma_{\text{Total}} = \Sigma_{\Delta v} + \Sigma_{\beta} + \Sigma_{\text{G\&P}} + \Sigma_{\text{wind}} + \Sigma_{\text{lift}} \quad (2.13)$$

Where,

Σ : covariance matrix of impact distribution area due to uncertainties

Δv : uncertainty in imparted velocity by explosion

β : uncertainty in ballistic coefficient

G&P : guidance and performance error

wind: uncertainty in wind effect

lift : uncertainty in lift effect

The total covariance matrix means the impact probability distributions accounting for the impact uncertainties for each of the sources of uncertainty. The resulting total covariance matrix computed above is a 2×2 matrix defined in Earth-North coordinate. In order to eliminate the non-diagonal terms, the coordinate is transformed to principal coordinates [14, 39];

$$[\Sigma_{\text{total}}]_{E,n} = \begin{bmatrix} \sigma_E^2 & \sigma_{EN} \\ \sigma_{EN} & \sigma_N^2 \end{bmatrix} \rightarrow \begin{array}{c} \text{Coordinate Transformation} \\ \begin{array}{c} \eta \\ \text{N} \\ \xi \\ \varphi \\ \text{E} \end{array} \end{array} \rightarrow \begin{bmatrix} \sigma_{\xi}^2 & 0 \\ 0 & \sigma_{\eta}^2 \end{bmatrix} \quad (2.14)$$

Where,

$$\varphi = 0.5 \tan^{-1} \left(\frac{2\sigma_{EN}}{\sigma_N^2 - \sigma_E^2} \right) \quad (2.15)$$

Dispersion ellipses have semi-major and semi-minor axes ($\sigma_{\xi}, \sigma_{\eta}$) defined by the directions of the axes forming a bivariate normal impact distribution.

2.2 Expected casualty

The probability that a fragment group impacts a population center can be calculated using the impact distribution, the area of the population center, and the relative location of the population center based on the mean impact point of the fragment group. The total impact covariance matrix for a given fragment group is usually assumed to define a bivariate normal probability density function as follows (Here, ξ , and η are the principal coordinates and the mean value is located on the origin point($\xi=0, \eta=0$));

$$P(\xi, \eta) = \frac{1}{2\pi\sigma_\xi\sigma_\eta} \times e^{-\frac{\xi^2}{2\sigma_\xi^2}} \times e^{-\frac{\eta^2}{2\sigma_\eta^2}} \quad (-\infty < \xi < \infty \text{ and } -\infty < \eta < \infty) \quad (2.16)$$

Then, the impact probability of a fragment group on a population center is obtained by integrating the bivariate normal density function over the region of the population center;

$$P_I = \frac{1}{\sqrt{2\pi}\sigma_\xi} \int_{\xi_A - 0.5\sqrt{A_P}}^{\xi_A + 0.5\sqrt{A_P}} e^{-\frac{\xi^2}{2\sigma_\xi^2}} d\xi \times \frac{1}{\sqrt{2\pi}\sigma_\eta} \int_{\eta_A - 0.5\sqrt{A_P}}^{\eta_A + 0.5\sqrt{A_P}} e^{-\frac{\eta^2}{2\sigma_\eta^2}} d\eta \quad (2.17)$$

Where,

P_I : impact probability of a fragment group on a population center

σ_ξ : standard deviation of impact distribution (downrange direction) of the fragment group (m)

σ_η : standard deviation of impact distribution (crossrange direction) of the fragment group (m)

ξ_A : distance from the mean impact point of the fragment group to the population center (downrange direction) (m)

η_A : distance from the mean impact point of the fragment group to the

population center (crossrange direction) (m)

A_p : area of the population center (m^2)

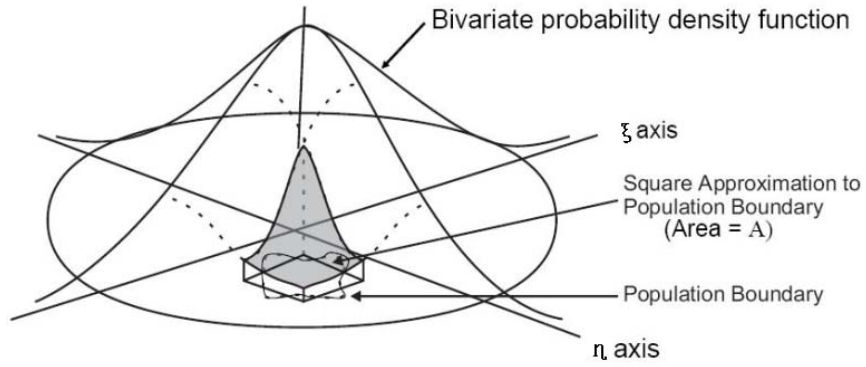


Fig.2.2 Bivariate normal density function

When the impact probability of each fragment group on each population center is obtained, the casualty expectation for a fragment group “i” for a population center “j” for a given failure time and failure mode is given by;

$$E_{C,ij} = P_{I,ij} \times A_{C,i} \times \frac{N_{P,j}}{A_{P,j}} \quad (2.18)$$

Where

i : index for fragment groups

j : index for population centers

$E_{C,ij}$: casualty expectation for a fragment group “i” for a population center “j”

$P_{I,ij}$: probability of a fragment from debris group “i” impacting on population center “j”

$A_{C,i}$: casualty area (the area on the ground within which a person will become a casualty) for a fragment group “i” (m^2)

$N_{P,j}$: the number of people in population center “j”

$A_{P,j}$: area of the population center “j” (m^2)

Chapter 2

The accumulated E_c (casualty expectation) for a given failure time and failure mode is computed by summing the E_c values over all fragment groups and population centers;

$$E_{C-accum} = \sum_i \sum_j E_{C,ij} \quad (2.19)$$

The $E_{C-accum}$ values are weighted by their corresponding probability of occurrence and summed over all failure times and failure modes to get the total casualty expectation of the mission;

$$E_{C-collective} = \sum_k \sum_l P_{f,kl} \times E_{C-accum,kl} \quad (2.20)$$

Where,

$E_{C-collective}$: collective E_c for the mission

k : index for failure time

l : index for failure mode

$P_{f,kl}$: probability of l^{th} failure mode occurring at k failure time

$E_{c-accum,kl}$: accumulated E_c for k failure time and l^{th} failure mode

2.3 Sheltering model

2.3.1 Fragment sheltering model

The risk to the people is generally sensitive to the presence of various shelter types. In this research, the fragment sheltering model presented by ACTA (Inc) [14, 40] in USA was used. They categorized the roof of buildings into 4 classes (light metal, wood, composite, and concrete reinforced with steel roof) and estimate the casualty area of a fragment according to the ballistic coefficient and weight of the fragment for each roof class. The casualty area was determined by simulating the impact of the fragment on

the roof and the penetration phenomena accounting for the human vulnerability [14, 40]. Since each different location of impact on the roof will have different effect, they simulate the impacts on the roof over thousands of locations on the roofs and over many roof types. The resulting sheltering model is presented in Figs. 2.3-2.6 [14, 40].

Some of the irregularities of the curves may be attributed to the fact that as the fragment size increases, the fragment may no longer fit between the joists of a roof structure, and hence the probability of penetrating through a relatively weak roof plate drops to zero. Meanwhile the kinetic energy may become large enough to fail the joists, resulting in steep increments of casualty area. It is similar when the fragment becomes too large to fit between the girders [40].

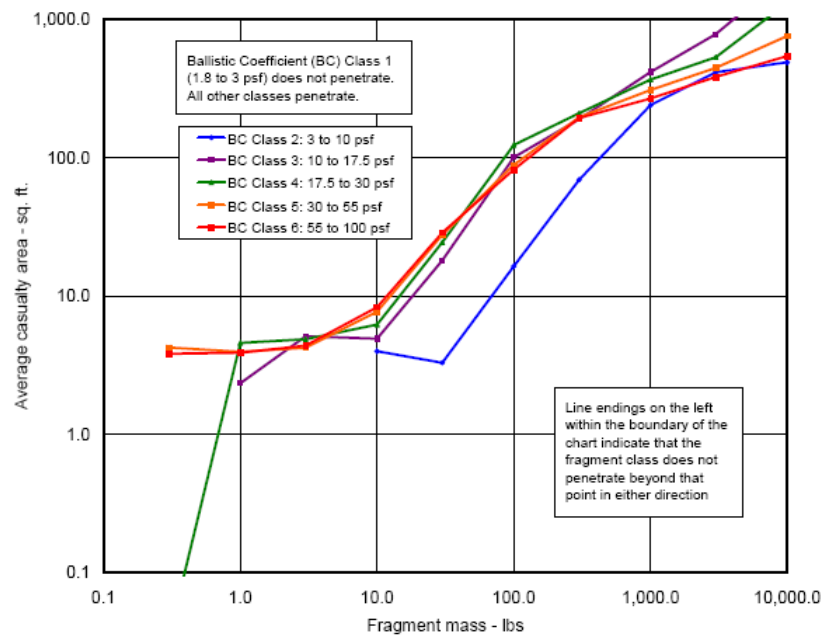


Fig.2.3 Casualty areas due to penetration of debris hitting a wood roof [14]

Chapter 2

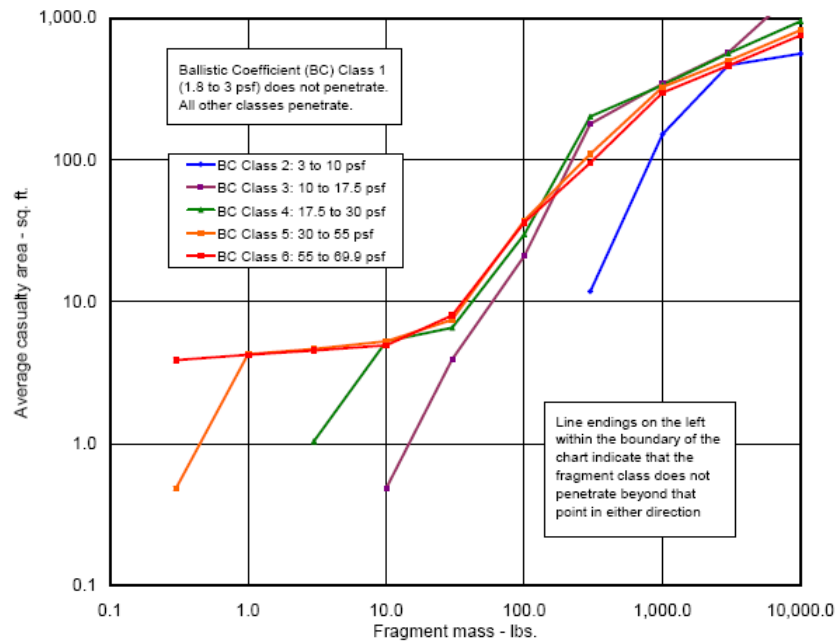


Fig.2.4 Casualty areas due to penetration of debris hitting a light metal roof [14]

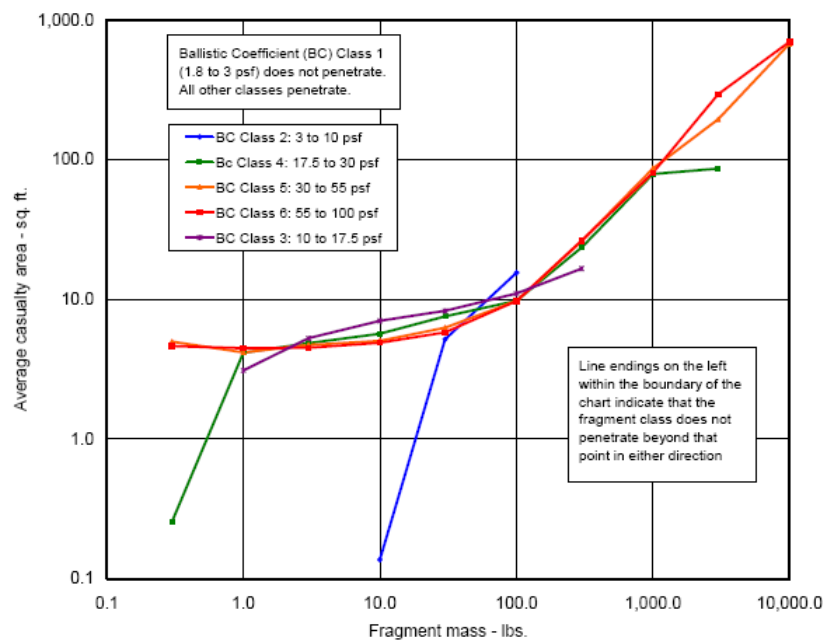


Fig.2.5 Casualty areas due to penetration of debris hitting a composite roof [14]

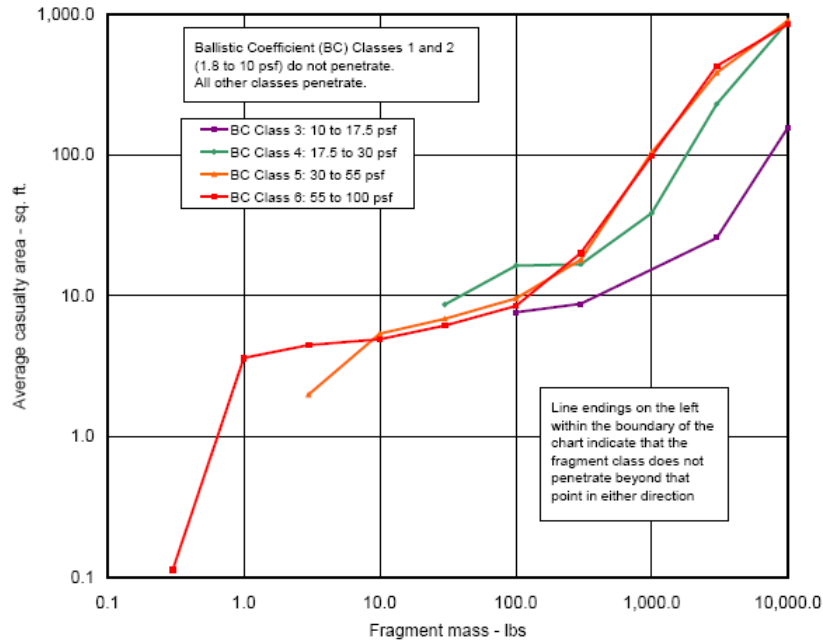


Fig.2.6 Casualty areas due to penetration of debris hitting a reinforced concrete roof [14]

The casualty area for people in the open where no sheltering effect was provided can be calculated accounting for the size and ballistic coefficient of debris, the area occupied by a person, and bouncing effect of the fragment etc [61].

2.3.2 Population sheltering model

In order to utilize the fragment sheltering model described in prior section for flight safety analysis, an allocation of how many people are in each sheltering level at each location should be made in advance. This is called the population sheltering model in this research. The method to allocate the people in a region to each sheltering category can be summarized by a matrix equation. The sheltering in a population center, \mathbf{c} (a vector whose elements are the number of people in the sheltering categories, and each

Chapter 2

row of the vector corresponds to a sheltering class), is calculated as follows [41];

$$\mathbf{c} = e_1 e_2 \mathbf{O} \mathbf{o} + s_1 s_2 \mathbf{q} + (1 - e_1 e_2 - s_1 s_2)[(1 - d - v) \mathbf{H} \mathbf{h} + (0 \ 0 \ \dots \ d \ v)^T] \quad (2.21)$$

The definitions of all variables of the equation are presented in table 1. The sum of each row of \mathbf{O} and \mathbf{H} is 100%, as are the sums of the components in each of the vector \mathbf{o} , \mathbf{q} , and \mathbf{h} .

Table. 1 Variables in equation for population sheltering model [41]

Variable	Description
e_1	Fraction of people who are employed
e_2	Fraction of those employed who are at work
\mathbf{o} (vector)	Fraction of people who are at work in each occupation category
\mathbf{O} (matrix)	Fraction of people in each sheltering class by occupation
s_1	Fraction of people who are students
s_2	Fraction of students who are at school
\mathbf{q} (vector)	Fraction of people at school in each sheltering class
d	Fraction of people not at work or school who are outside
v	Fraction of people not at work or school who are in vehicles
\mathbf{h} (vector)	Fractions of people in each housing type
\mathbf{H} (matrix)	Fraction of people in each sheltering class by housing type

In this research, population sheltering model was constructed based on the census data of the country near the flight track [41, 42]. The percentage of people who are in each building sheltering level (open, light metal, wood, composite, reinforced concrete roof) was estimated accounting for the building type, population data according to ages, and the GDP level of the country etc. The resulting population sheltering model for Australia which will be employed in the flight safety analysis in Chapter 4 is presented

in table 2 [43].

Table. 2 Population sheltering model for Australia [43]

	Open	Wood	Light metal	Composite	Concrete reinforced with steel	Total
Population ratio	0.100	0.548	0.317	0	0.036	1.00

In order to apply the sheltering model in calculating the expected casualty, equation (2.18) can be modified as follows;

$$E_{C,ij} = P_{I,ij} \times \sum_m A_{C,i,m} \times \frac{N_{P,j,m}}{A_{P,j}} \quad (2.22)$$

Where

i : index for fragment groups

j : index for population centers

m : index for sheltering levels

$E_{C,ij}$: casualty expectation for a fragment group “i” for a population center “j”

$P_{I,ij}$: probability of a fragment from debris group “i” impacting on population center “j”

$A_{C,i,m}$: casualty area for a fragment group “i” on the given population center sheltering level “m” (m^2)

$N_{P,j,m}$: the number of people in population center “j” for given sheltering level “m”

$A_{P,j}$: area of the population center (m^2)

2.4 Program validation

It is difficult to validate a flight safety analysis program by comparing the analysis results with experimental data because those experiments have never been conducted and are nearly impossible to do. The utilization of the actual fail cases which caused casualties on the ground is also difficult because the data regarding the detailed trajectory, attitude, and fail phenomena etc. of the vehicles haven't been open to the public. As a result, the developed program in the present research was validated by comparing the analysis results with those of a code developed in a company in U.S. and used for several decades in mission planning of launch vehicles.

FSAS code was validated using a program named TumCor which was developed by ACTA (Inc) [4, 14]. Because the TumCor program employs a very simple approach that utilizes only vehicle failure rate, IIP(Instantaneous Impact Point) traces of the vehicle fragments, crossrange dispersion of the IIP, and fragment casualty area, the analysis can be performed very fast while the results include some uncertainties. Therefore, although it cannot be used for a final casualty expectation prediction, the program can be used in mission planning [4]. Because the flight safety analysis cannot be validated via an experimental method and the flight safety analysis codes with high fidelity or the results obtained by those codes aren't open to the public, the TumCor program was used for the validation of FSAS code in this study.

The flight safety analysis on a sample launch vehicle which overflies East Indonesia at very high velocity was conducted by two programs (FSAS and TumCor). It was assumed that the launch vehicle has the dry weight of 0.14 ton and the vehicle would impact the earth in intact state. The casualty area for people in the open of 10 m² and the failure rate of 1e-3 (per second) were used. The ratio of people in the open, wood, light metal, composite, and concrete sheltering level are assumed to be 0.3, 0.2, 0.2, 0.2, and 0.1 respectively. The LandScan 2005 [44] population data was used as the world population model.

For FSAS simulation, the magnitudes of position and velocity standard deviation (σ)

by guidance and performance error were assumed to be 10 km and 15 m/s respectively. The April wind profile on the area was used. Because the vehicle was assumed to fall in intact state, the ballistic coefficient uncertainty was not included. With these assumptions, the fragment footprints for the area are computed as presented in Fig. 2.7. An ellipse represents a 3 sigma (3σ) impact distribution area by flight failure in one second period.

For TumCor calculation the IIP crossrange standard deviation was assumed to be 18km which was estimated from Fig. 2.7.

The Ec contours by two codes are depicted in Fig. 2.8 and Fig. 2.9. As can be seen in the figures, the results by two codes show good agreement in Ec distribution. The total Ec result computed by FSAS was $2.82\text{E-}7$ while the TumCor code predicted the Ec value of $3.08\text{E-}7$ making about 8% difference between two codes. Considering the difference in the calculation conditions, the Ec values by two codes are thought to be in reasonable agreement. Figures 2.10 and 2.11 are the Ec distributions according to latitude and longitude by two codes. In the Ec-latitude graph, the Ec value for each latitude point is summed for whole longitudes at that latitude and the each Ec value in Ec-longitude graph represents Ec value summed for all latitudes at that longitude. As can be seen in Figs. 2.10 and 2.11, the results by two codes are quite coincident.

Chapter 2

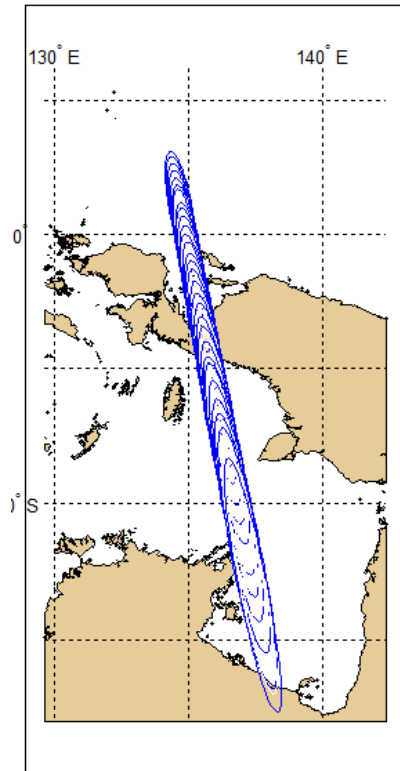


Fig.2.7 Fragment footprints (3σ) by failures of the sample launch vehicle

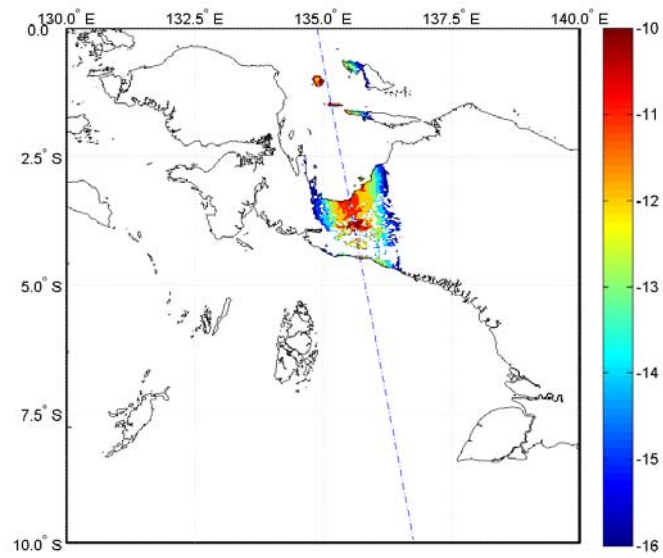


Fig.2.8 Expected Casualty ($\log_{10}(Ec/km^2)$) by FSAS

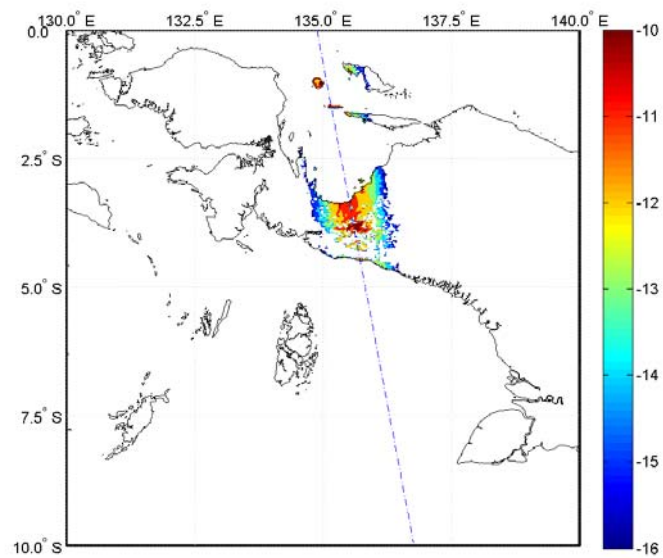


Fig 2.9 Expected Casualty($\log_{10}(Ec/km^2)$) by TumCor

Chapter 2

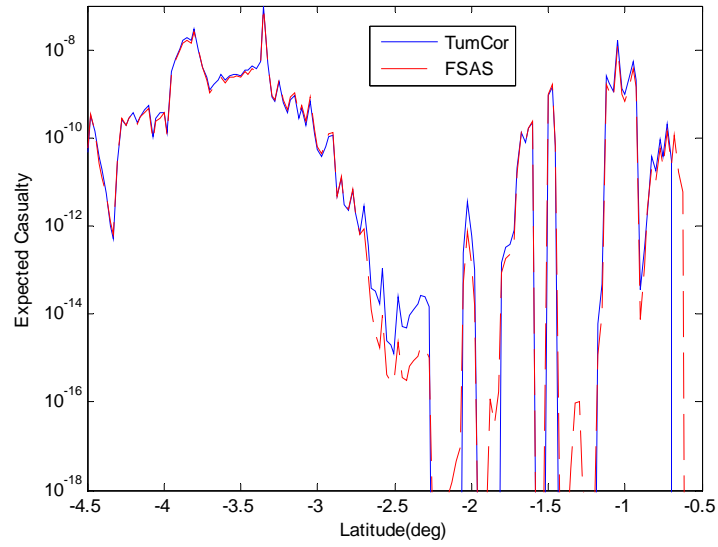


Fig.2.10 Comparison of Ec values of sample launch vehicle for latitudes by TumCor and FASA codes

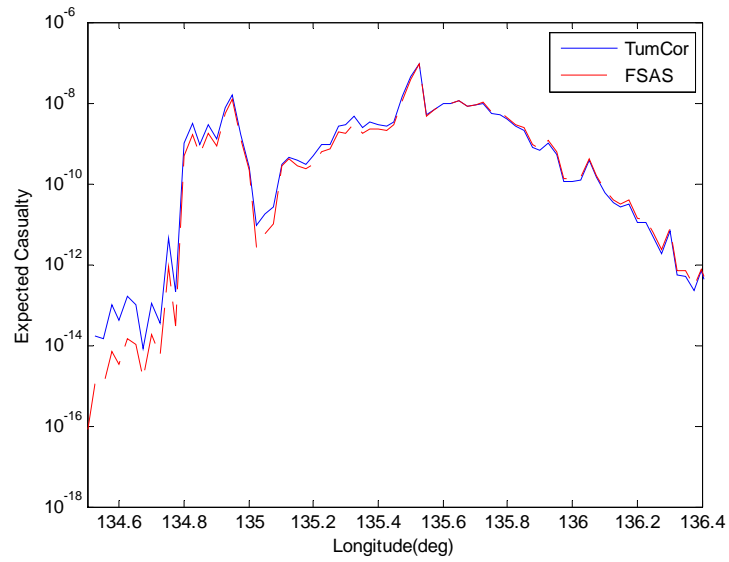


Fig.2.11 Comparison of Ec values of sample launch vehicle for longitudes by TumCor and FASA codes

Chapter 3. Development of Survivability Analysis Program for Atmospheric Reentry (SAPAR)

When launch vehicles fail at very high velocity, fragments from launch vehicle are subject to extreme aerodynamic thermal loads during atmospheric reentry resulting in full or partial melting or ablation if the fragments have low melting points and thermal capacities. The flight safety analysis procedure explained in Chapter 2 does not include these melting phenomena, so the analysis have a tendency to overestimate the risk to the ground by assuming the fragment would impact the earth surface without any mass loss. Therefore, in this research, a survivability analysis program for atmospheric reentry named SAPAR(Survivability Analysis Program for Atmospheric Reentry) [35] was developed and combined to the flight safety analysis program (FSAS) in order to enhance the accuracy for the analysis of the risk posed by failed launch vehicles.

SAPAR analyze the survivability of fragments by simulating the fragment trajectory until they hit the Earth or are fully ablated assuming the satellite or launch vehicle breakup at certain altitude as in ORSAT. Aerodynamic thermal loads during free fall, temperature variation due to thermal loads, and phase shift after object reaches melting point are included in the analysis. SAPAR can analyze several shapes - sphere, cylinder, box, and flat plate – using lumped mass model or nodal thermal mass model. Detailed explanation about the program module is given below.

3.1 SAPAR Module

SAPAR (Survivability Analysis Program for Atmospheric Reentry) was developed using an approach and equations similar to those of ORSAT with some improvements. The SAPAR code employs integrated trajectory, aerodynamic, aerothermodynamic and thermal modules to simulate the reentry process. The trajectory module simulates a

three degree-of-freedom (DOF) trajectory by integrating the equations of motion. The aerodynamic module computes the aerodynamic coefficient of the fragment that is used in the trajectory module. The aerothermodynamic module analyzes the thermal load on the fragment during free fall using the velocity and position data provided by the trajectory module. The thermal module calculates the temperature history of the surface and the nodes of the fragment using the thermal loads calculated in aerothermodynamic module. The ablation module determines whether the nodes of the fragment would demise or not, using the results of the thermal and the aerothermodynamic module. If the nodes of the fragment melt, the size and mass of the fragment vary, which affects the trajectory of the fragment. The process continues until all layers demise or the fragment impacts the ground. Figure 3.1 shows a block diagram of the relationship between the modules of the SAPAR code.

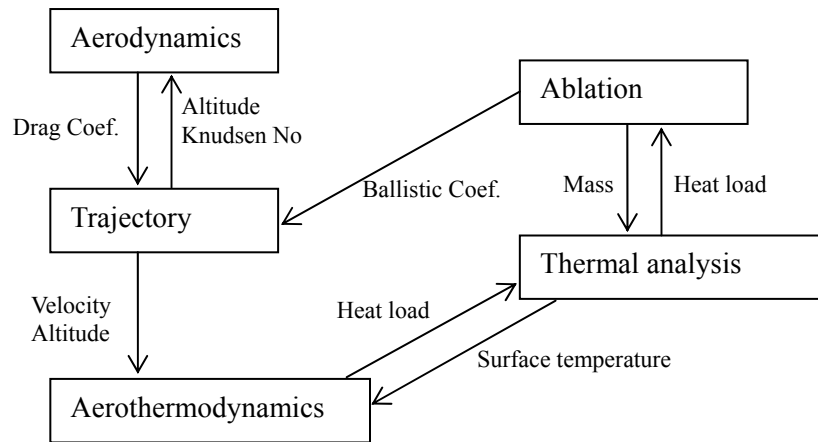


Fig.3.1 Program module of SAPAR code

3.1.1 Trajectory module

The trajectory module computes a 3-degree-of-freedom trajectory assuming the object is affected by the gravity and aerodynamic force. The differential equation in ECI (Earth Centered Inertial) was integrated to calculate the motion of the object in

Chapter 3

WGS84 Earth model. US Standard 1976 model [37] or the GRAM95 (NASA/MSFC Global Reference Atmospheric Model-1995) [38] was used as the atmosphere and wind model. The differential equations of motion for 3-dof simulation in ECI frame is as follows.

$$\frac{d}{dt}\vec{r} = \vec{v} \quad (3.1)$$

$$\frac{d}{dt}\vec{v} = \vec{g}(\vec{r}) + \vec{a}(\vec{r}, \vec{v}) \quad (3.2)$$

Where,

\vec{r} : position vector in ECI frame (m)

\vec{v} : velocity vector in ECI frame (m/s)

\vec{g} : acceleration by Earth gravity (m/s²)

\vec{a} : acceleration by aerodynamic force including wind effects (m/s²)

t : time (sec)

3.1.2 Aerodynamics module

The aerodynamics module computes average drag coefficients of objects within free molecular, transitional, and continuum flow regimes [23, 27, 45, 46]. Continuum flow exists at small (0 to 0.0001) Knudsen numbers ($Kn=\lambda/L$, λ : mean free path, L: characteristic dimension of the body) while the flow becomes free-molecular when Knudsen number increases (over 10.0). Transition flow exists in between.

3.1.2.1 Drag coefficient of spheres

1) Free molecular regime ($Kn>10$)

Assuming the air molecules which strike the sphere surface lose all of their kinetic energy and are reflected at roughly the same temperature as the object (i.e. diffuse

reflection), the drag force can be calculated as the rate of variation of momentum per unit time of the air molecules [45];

$$D = \rho A V_{\infty} \times V_{\infty} = \rho A V_{\infty}^2 \quad (3.3)$$

Where,

D : drag force (N)

ρ : air density (kg/m³)

A : cross sectional area of sphere (πr^2) (m²)

V_{∞} : Object velocity (m/s)

Drag coefficient can be calculated as follows;

$$C_d = \frac{D}{0.5 \rho V_{\infty}^2 A} = \frac{\rho A V_{\infty}^2}{0.5 \rho V_{\infty}^2 A} = 2.0 \quad (3.4)$$

It was suggested that the drag coefficient of sphere in free-molecular flow regime is 2.07 via an experimental study [31]. The value of 2.07 was used as the drag coefficient of sphere in free-molecular regime in this research.

2) Continuum regime ($Kn < 0.0001$)

The drag coefficient of sphere in continuum flow can be calculated using modified Newtonian law [47];

$$C_p = C_{p_max} \sin^2 \theta \quad (3.5)$$

Where,

C_p : pressure coefficient ($\frac{p_1 - p_{\infty}}{0.5 \rho V_{\infty}^2}$)

C_{p_max} : maximum pressure coefficient right after a normal shock wave

($C_{p_max} = 1.84$ for air with specific heat of 1.4)

θ : angle between free stream and wall (rad)

Consider the following diagram;

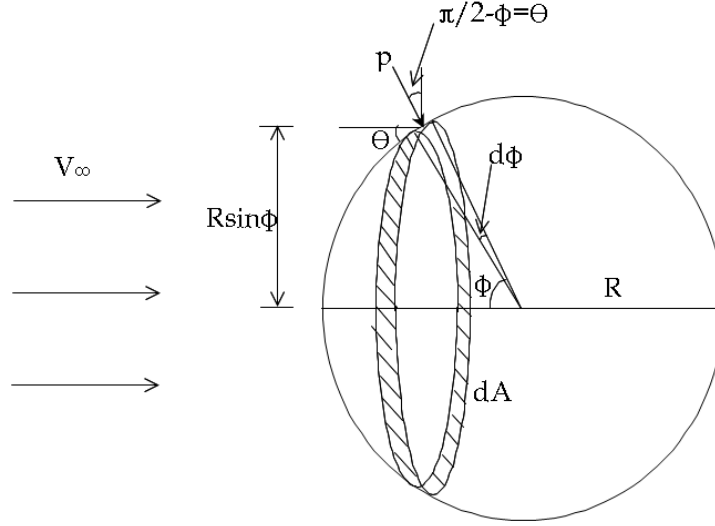


Fig.3.2 Sphere in continuum flow

In Fig. 3.2, when the normal pressure on the infinitesimal area dA defined by $d\Phi$ is p , the drag force to dA is as follows;

$$dD = p \times dA \times \sin\left(\frac{\pi}{2} - \Phi\right) = p \times dA \times \cos\Phi \quad (3.6)$$

From simple geometric calculation,

$$dA = 2\pi(R\sin\Phi)Rd\Phi = 2\pi R^2\sin\Phi d\Phi \quad (3.7)$$

Using modified Newtonian law with the definition of the pressure coefficient, the pressure (p) on dA is calculated as follows;

$$p = C_{p_max}\sin^2\theta q_\infty + p_\infty = C_{p_max}\cos^2\Phi q_\infty + p_\infty \quad (3.8)$$

If we assume the pressure on the opposite side of the free stream is equal to the pressure of the free stream, the total drag force on the sphere is expressed as following;

$$D = \int_0^{\frac{\pi}{2}} C_{p_max}\cos^2\Phi q_\infty 2\pi R^2\sin\Phi d\Phi \cos\Phi \quad (3.9)$$

The above integral can be simply equated as follows;

$$D = 0.5C_{p_max}\pi R^2 q_\infty \quad (3.10)$$

Therefore, the drag coefficient is $0.5C_{p_max}$ for reference area of πR^2 . With the C_{p_max} of 1.84 for air with specific heat of 1.4, the resulting drag coefficient of a sphere in continuum flow is 0.92.

3) Transition regime ($0.0001 < Kn < 10$)

The drag coefficient in transition regime is generally computed using a bridging function which makes the value lie between the drag coefficients of continuum and free molecular flows. In this research the bridging function presented by Rochell et al. [31] was used (see Fig. 3.3).

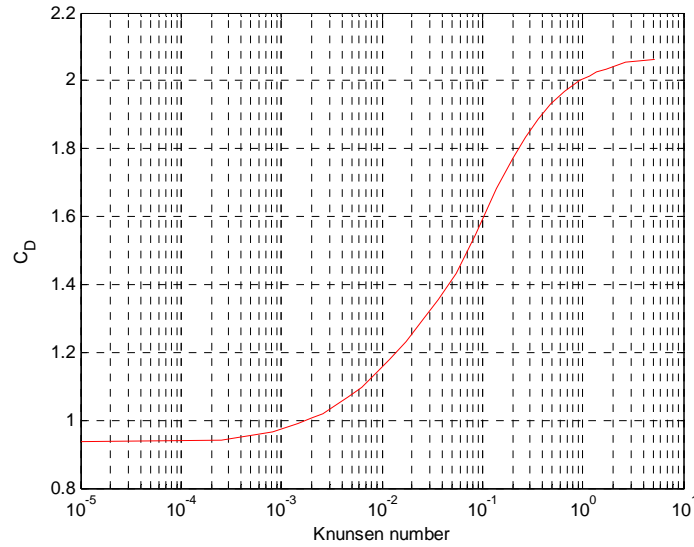


Fig.3.3 Drag coefficient of sphere in transitional regime

3.1.2.2 Drag coefficient of other shapes

Drag coefficients of cylinder, box, and flat plates can be calculated using the similar methods as sphere [45, 46, 48]. The values can be found in table 3. Here, R denotes the

Chapter 3

radius of a sphere, L is the length of a cylinder, a box, or a flat plate, D is the diameter of a cylinder, and W denotes the width of a box or a flat plate. The bridging functions of these shapes for transition regime are obtained based on Fig. 3.3 and Cropp [46].

Table. 3 Drag coefficients for various object shapes and flow regimes

Shape	Motion	Reference area	C_D (free-molecular flow)	C_D (continuum flow)	C_D (transition regime)
sphere	spinning	πR^2	2.07	0.92	Bridging function (function of Kn)
cylinder	end-on	LD	$1.57D/L$	$1.314D/L$	
	broad side and spinning	LD	2.0	1.227	
	end-over-end tumbling	LD	$1.27+D/L$	$0.52+0.56D/L$	
	random tumbling	LD	$1.57+0.79D/L$	$0.72+0.33D/L$	
box	broad side and tumbling	LW	2.55	1.42	
	end-over-end tumbling	$0.5(LW+W^2)$	2.55	1.42	
flat plate	tumbling	LW	1.27	0.71	

3.1.3 Aerothermodynamics module

The aerothermodynamics module compute the heat fluxes to reentry objects including the convective heating, oxidation heating, and reradiation heat loss based on the object shape and velocity, the air density, and the surface temperature of the object etc. Because SAPAR employs the lumped or 1-D nodal mass model, the heat fluxes averaged over the whole object surface are used in the simulation.

The net average heating (\bar{q}_{net}) to the reentering object is equal to the average hot wall convective heat flux (\bar{q}_{hw}) plus the oxidation heat flux (\bar{q}_{ox}) minus the reradiation heat flux (\bar{q}_{rr});

$$\bar{q}_{\text{net}} = \bar{q}_{\text{hw}} + \bar{q}_{\text{ox}} - \bar{q}_{\text{rr}} \quad (3.11)$$

The average convective heat flux to the actual hot wall (\bar{q}_{hw}) was calculated as the cold wall value multiplied by the wall enthalpy ratio [23]. The average cold-wall convective heat flux (\bar{q}_{cw}) is computed based on the fraction of the sphere or flat plate stagnation point heat flux. The oxidation heat fluxes were modeled using the equation presented by Cropp [46]. The reradiation heat loss was computed using the Stephan-Boltzmann equation with the temperature of the outer surface and the thermal emissivity. The reference area for the reradiation heat loss (\bar{q}_{rr}) was chosen as the whole surface area contacting the surrounding air.

3.1.3.1 Computation of cold wall Stagnation point heat flux

1) Free molecular regime ($\text{Kn} > 10$)

The stagnation point heat flux to a flat plate in free molecular regime is calculated by multiplying the thermal accommodation coefficient by the stagnation enthalpy and the mass flux [45]. The stagnation enthalpy can be approximated as $0.5V_{\infty}^2$ when the object moves at high velocity. The thermal accommodation coefficient is between 0.8 and 1.0 in most objects, so the value of 0.9 was used for all objects in this research [46]. Therefore, the stagnation heat flux to a flat plate in free molecular regime can be expressed as follows [45, 46];

$$\dot{q}_{\perp} = \frac{0.9\rho V_{\infty}^3}{2} \quad (3.12)$$

The above value can be used as the stagnation heat flux to a sphere in free molecular regime [46].

2) Continuum regime ($\text{Kn} < 0.001$)

For the sphere stagnation point heat flux in continuum regime, the Detra, Kemp, and Riddell formula [49] was used in the research. This equation approximates the higher

Chapter 3

fidelity Fay-Riddell formula [27, 50, 51] and valid in the range sea level to 76 km and 2.1 to 7.6 km/s [49]. The Detra, Kemp, and Riddell formula for sphere stagnation point heating is as follows [24, 49];

$$\dot{q}_{ss} = \frac{110285}{\sqrt{R}} \left(\frac{\rho}{\rho_{sl}} \right)^{0.5} \left(\frac{V}{V_{cir}} \right)^{3.15} \quad (3.13)$$

Where,

\dot{q}_{ss} : sphere stagnation point heat flux (kW/m²)

ρ_{sl} : sea level air density (kg/m³)

V_{cir} : orbit velocity at 122 km altitude (=7803m/s)

R : sphere radius (m)

The stagnation point heat flux for flat plate in continuum flows can be calculated by multiplying the sphere stagnation point heat flux by 0.5 [45, 52]

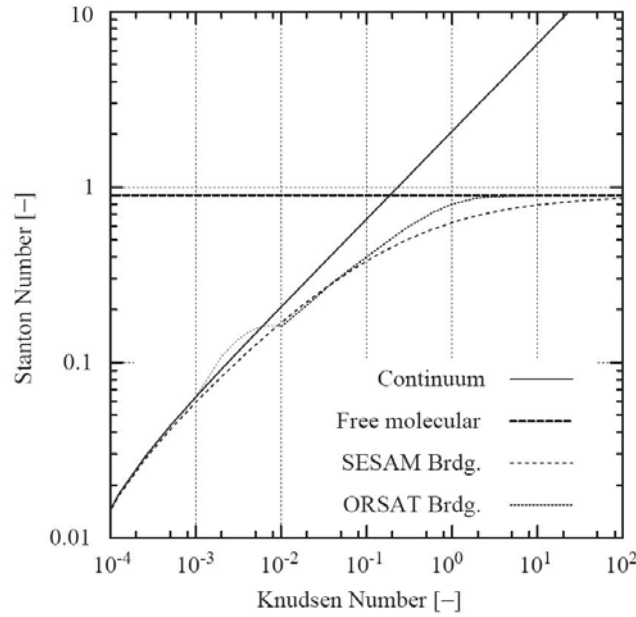


Fig.3.4 Stagnation point Stanton number bridging function in transitional flow regime [19]

3) Transition regime ($0.001 < Kn < 10$)

The stagnation point heat flux in transition regime was computed using bridging functions for Stanton number as in ORSAT [19, 24, 46]. Stanton number (St) can be approximated as follows when the object velocity is very high;

$$St = \frac{\dot{q}}{0.5\rho V^3} \quad (3.14)$$

When Stanton number can be obtained from the bridging function, the stagnation point heat flux can be calculated based on the above relation. The bridging function for sphere stagnation point in SAPAR code is same as that of ORSAT in Fig. 3.4;

3.1.3.2 Area-averaged heat ratio factor of spheres for cold wall

Because SAPAR employs the lumped or 1-D nodal mass model, the heat fluxes averaged over the whole object surface are used in the simulation. This is accomplished by integrating the heating rate distribution curve about the surface in a given flow regime and dividing it by the surface area. The area averaged heat ratio factor (F) can be used to convert stagnation point heating to the area average heating for cold wall.

$$\bar{q}_{cw} = F \times q_{stagn} \quad (3.15)$$

Where,

\bar{q}_{cw} : area average heat flux for cold wall (kW/m²)

F : area average heat ratio factor

q_{stagn} : stagnation point heat flux (kW/m²)

1) Free molecular regime ($Kn > 10$)

The free-molecular heating to flat plates at angles of attack (θ) can be expressed as follows [45];

$$q_{\theta} = q_{\perp} (\sin \theta + 0.0113 \cos \theta) \text{ for } 0 \leq \theta \leq \frac{\pi}{2} \quad (3.16)$$

Chapter 3

Consider the Fig. 3.2 to calculate the area averaged heat flux to spheres in free-molecular regime. Then, the heat flow rate the infinitesimal area dA observes can be equated as follows;

$$\begin{aligned} d\dot{Q} &= q_{\perp}(\sin \theta + 0.0113 \cos \theta) \times 2\pi R \sin \Phi R d\Phi \\ &= q_{\perp}(\sin \theta + 0.0113 \cos \theta) \times 2\pi R^2 \sin \Phi d\Phi \end{aligned} \quad (3.17)$$

If we ignore the heating to the opposite side of free stream ($\pi/2 < \Phi < \pi$), the total heat absorbed to the sphere in free molecular regime per unit time can be calculated by integrating the above equation from 0 to $\pi/2$.

$$\dot{Q} = \int_0^{\pi/2} d\dot{Q} = \int_0^{\pi/2} q_{\perp}(\sin \theta + 0.0113 \cos \theta) \times 2\pi R^2 \sin \Phi d\Phi = 1.018\pi R^2 q_{\perp} \quad (3.18)$$

The area averaged heat flux to spheres in free molecular regime can be expressed as follows;

$$\bar{q} = \frac{1.018\pi R^2 \dot{q}_{\perp}}{4\pi R^2} = 0.254 \dot{q}_{\perp} \quad (3.19)$$

As can be seen in above equation, the area averaged heat ratio factor for spheres in free molecular regime ($F_{\text{fm, sphere}}$) is 0.254.

2) Continuum regime ($\text{Kn} < 0.001$)

Figure 3.5 shows the experimental data for the heat transfer distribution on the sphere. Analysis of the data showed that there is a $(\cos(\theta/2))^a$ distribution in the heating rate [28]. Based on Fig. 3.5 the total heat absorbed to the sphere per unit time in continuum regime can be calculated as follows;

$$\dot{q}_{\text{local}} = \left(\cos \frac{\theta}{2} \right)^{5.27} \dot{q}_{ss} \quad (3.20)$$

$$\dot{Q} = \int_0^{\pi} \left(\cos \frac{\theta}{2} \right)^{5.27} \dot{q}_{ss} \times 2\pi R^2 \sin \theta d\theta = 0.275 \times 4\pi R^2 \times \dot{q}_{ss} \quad (3.21)$$

The area averaged heat flux to spheres in continuum regime can be expressed as follows;

$$\bar{q} = \frac{0.275 \times 4\pi R^2 \times \dot{q}_{ss}}{4\pi R^2} = 0.275 \dot{q}_{ss} \quad (3.22)$$

As can be seen in above equation, the area averaged heat ratio factor for spheres in continuum regime ($F_{\text{cont, sphere}}$) is 0.275.

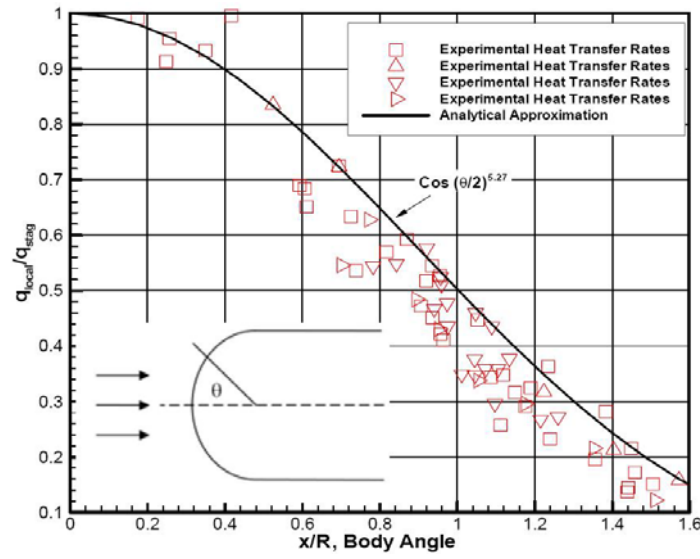


Fig.3.5 Heat transfer rate distribution on the sphere [28]

3) Transition regime ($0.001 < \text{Kn} < 1$)

The area averaged heat ratio factor for spheres in transition regime was assumed to be linearly varied according to $\log(\text{Kn})$ like in ORSAT.

3.1.3.3 Area-averaged heat ratio factor of other shapes for cold wall

Area-averaged heat ratios of cylinder, box, and flat plates can be calculated using the similar methods as sphere [45, 46, 48]. The values are summarized in table 4. Here, the angular velocities of the body in tumbling and spinning are assumed to be large

Chapter 3

enough that the average heating rates adequately approximate actual heat rate distributions [46].

Table. 4 Area-averaged heat ratios for various object shapes and flow regimes

Shape	Motion	Reference area	F_{fm}	F_{cont}	F_{trans}
sphere	spinning	$4\pi R^2$	0.25	0.275	Bridging function (function of Kn)
cylinder	end-on	πDL	$X+0.25D/L$	$B+0.16D/L$	
	broad side and spinning	πDL	$Y+X/2 \times D/L$	$0.269+0.0735D/L$	
	end-over-end tumbling	πDL	$0.637(X+Y)+0.16D/L$	$0.135+0.5B+0.165D/L$	
	random tumbling	πDL	$(0.5X+0.785Y)+0.127D/L$	$0.179+B/3+0.162D/L$	
box	broad side and tumbling	$4LW$	$0.322+0.5XW/L$	$0.307+0.069W/L$	
	end-over-end tumbling	$4LW$	$0.5X+0.161+0.161W/L$	$0.222+0.154W/L$	
flat plate	tumbling	$2LW$	0.322	0.307	

The quantities X, Y, and B are defined by Figs. 3.6, 3.7 and 3.8, which have been presented by Cropp [46].

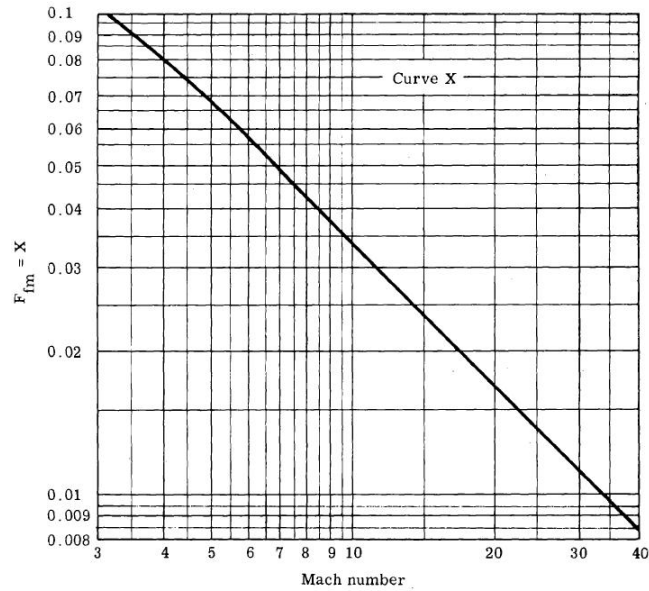


Fig.3.6 Free-molecular flow ratios of heating on surfaces parallel to the flow to stagnation-point heating on a sphere of the same radius [45, 46]

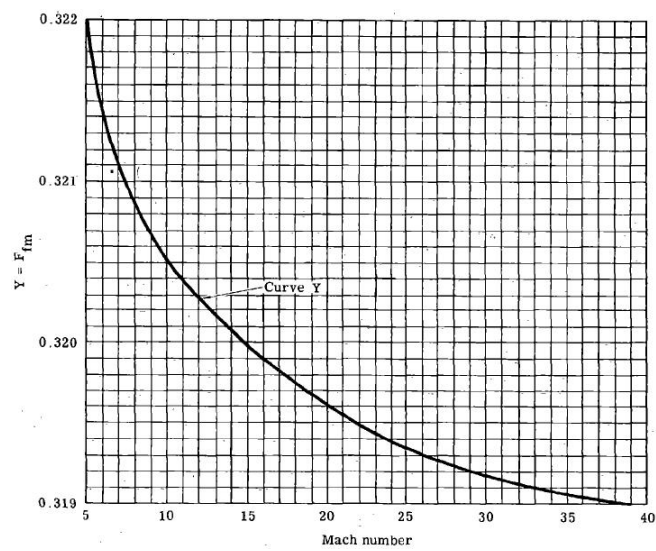


Fig.3.7 Free-molecular flow ratios of average heating on the sides of a rotating crossflow cylinder to stagnation-point heating to a sphere of the same radius [45, 46]

Chapter 3

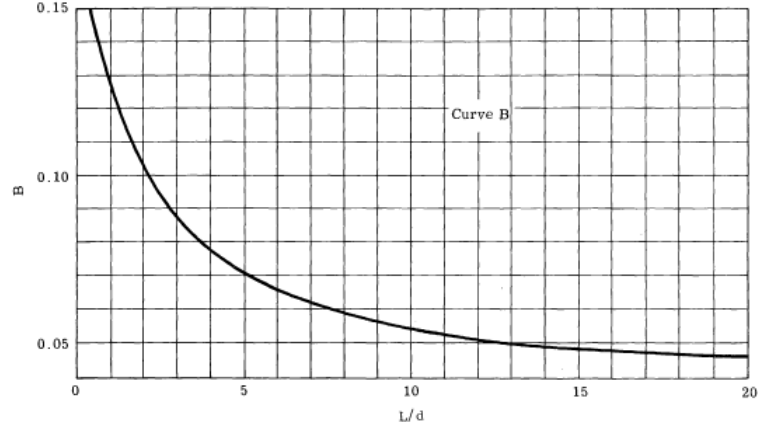


Fig.3.8 Continuum flow ratio of average heating to the side of an end-on cylinder to stagnation-point heating to a sphere of the same radius

3.1.3.4. Hot wall convective heat flux

The area averaged convective heat flux for cold wall (\bar{q}_{cw}) which can be calculated using the equations in the above sections is converted to the area averaged actual hot wall convective hat flux (\bar{q}_{hw}) using the enthalpy ratio [23]. The total heat absorbed to the actual object per unit time is obtained by multiplying the area averaged hot wall heat flux by the surface area;

$$\bar{q}_{hw} = \bar{q}_{cw} \left(\frac{h_{st} - C_{p,air} T_w}{h_{st} - C_{p,air} T_{cw}} \right) \quad (3.23)$$

$$\dot{Q} = \bar{q}_{hw} \times A_{surf} \quad (3.24)$$

Where,

h_{st} : stagnation enthalpy (J/kg)

$C_{p,air}$: specific heat at constant pressure for air (J/kg-K)

T_w : wall temperature of wall (K)

T_{cw} : cold wall temperature(=300K)

\dot{Q} : total heat absorbed to the object per unit time (J)

A_{surf} : surface area of the object (m^2)

The specific heat at constant pressure for air, $C_{p,\text{air}}$, is taken as a function of wall temperature, T_w as in ORSAT [53];

$$C_{p,\text{air}} = 959.9 + 0.15377T_w + 2.636 \times 10^{-5}T_w^2 \left(\frac{J}{kg \cdot K}\right), 300K \leq T_w \leq 2000K \quad (3.25)$$

$$C_{p,\text{air}} = 1004.7 \left(\frac{J}{kg \cdot K}\right), T_w \leq 300K \quad (3.26)$$

3.1.3.5. Oxidation heat flux

The re-entering material reacts chemically with oxygen and releases the heat of formation of the oxide to the body. Assuming the activity of air particles that reach the body surface is approximated by the Stanton number, Cropp [46] has suggested a oxidation heat flux model as follows.

The total mass flux of airflow past a body per unit area and unit time is expressed as $\rho_\infty V_\infty$. The amount of the flow that actually reaches the body surface is proportional to the level of activity of the air particle in the flow surrounding the object. This level of activity may be closely approximated by the Stanton number (St) and is an indication of the number of particles that diffuse to the body surface. In this light, the average mass rate of airflows to the body surface may be approximated as follows;

$$\dot{m}_{\text{air}} = St \cdot \rho_\infty V_\infty \quad (3.27)$$

Since the convective heat flux can be expressed using Stanton number (St) as

$$\dot{q}_{cw} = 0.5\rho_\infty V_\infty^3 \cdot St = h_{st}\rho_\infty V_\infty St \quad (3.28)$$

Equation (3.27) can be substituted into equation (3.28) to give;

$$\dot{m}_{\text{air}} = \frac{\dot{q}_{cw}}{h_{st}} \quad (3.29)$$

The flow rate was based on \dot{q}_{cw} rather than \dot{q}_{hw} since higher wall temperature will not decrease the actual number of collisions between air particle and the surface.

Chapter 3

The average mass flux of oxygen flow to a surface is as follows with the oxygen mass fraction of 0.215.

$$\dot{m}_{ox} = 0.215 \times \frac{\dot{q}_{cw}}{h_{st}} \quad (3.30)$$

Because only some fraction of the oxygen particles impacting the object will react with the surface, the resulting oxidation heat flux can be expressed as follows [46].

$$\dot{q}_{ox} = \frac{0.215 \times \dot{q}_{cw} \times \Delta H_{OX} \times \tau}{h_{st}} \quad (3.31)$$

Where,

\dot{q}_{ox} : oxidation heat flux (kW/m²)

ΔH_{OX} : heat of oxidation of the surface material per kg of oxygen (J/kg-O₂)

τ : oxidation efficiency

3.1.3.6. Reradiation heat loss

As a surface becomes heated, a portion of the thermal energy will be reradiated to space. The reradiation heat loss was computed using the Stephan-Boltzmann equation with the temperature of the outer surface and the thermal emissivity. The reference area for the reradiation heat flux (\dot{q}_{rr}) was chosen as the whole surface area contacting the surrounding air. This is the main difference from ORSAT where the reference area for reradiation heat loss is same as that of the convective heat flux [35]. The detailed explanation with this point will be given in section 3.2.2. The Stephan-Boltzmann equation for heat flux is as follows ;

$$\dot{q}_{rr} = \epsilon \sigma T_w^4 \quad (3.32)$$

Where,

ϵ : emissivity of the material (function of temperature)

σ : Stephan-Boltzmann constant ($5.67 \times 10^{-8} \text{W/m}^2 \text{K}^4$)

T_w : surface temperature (K)

3.1.3.7. Uncertainties of aerothermodynamics module

The modules of the SAPAR code have some level of errors in modeling the physical problem. Especially the aerothermodynamics module has several uncertainty sources due to the lack of the experimental and theoretical knowledge in hypersonic and high temperature gas dynamics. These sources need to be discussed for proper understanding of the analysis results.

The stagnation point heat flux calculation in continuum regime using the Detra, Kemp, and Riddell formula [49] has several assumptions that the flow is laminar, the flow reaches its equilibrium state at the edge of the boundary layer, and the flow in the boundary layer is in equilibrium state or the surface of the object is fully catalytic. Because the laminar flow conditions results in a lower heat flux following conservative results when compared with the turbulent flow conditions, it can be surely admitted in safety analyses. On the other hand, the assumption that the boundary layer is in equilibrium state or the surface is fully catalytic doesn't guarantee a conservative result and it needs to be estimated. Regarding this problem, more detailed analysis is given in the next chapter.

The oxidation heat flux is predicted using the equation and coefficients presented by Cropp [46] in this research as in ORSAT. The equation was derived using simple assumptions that seem to be lack of experimental or theoretical base. As a result, further researches regarding the oxidation heat flux is thought to be needed. Zero oxidation efficiency, which means zero oxidation heat flux, can be used to eliminate the uncertainty of the oxidation heat flux and to generate a conservative analysis result. However, the oxidation of the surface does proceed in reentry process, and need to be considered in the survivability analysis for accurate results.

3.1.4 Thermal module

SAPAR uses nodal thermal mass model for spheres, cylinders, and boxes, while applying lumped mass model for flat plate. The lumped mass model can be understood as the thermal mass model that has only one node. The thermal module of SAPAR determines the temperatures of surface and each node using the net heat flux ($\bar{q}_{net} = \bar{q}_{hw} + \bar{q}_{ox} - \bar{q}_{rr}$) calculated from aerothermodynamics module. A thermal conduction analysis is required to determine the appropriate temperature response of the object. The temperature was calculated by using a FTCS (Forward Time Central Space) finite difference solution in one space dimension.

3.1.4.1 Heat conduction of spheres

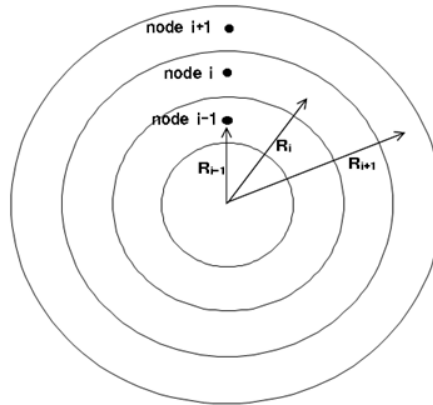


Fig.3.9 1-D heat conduction model of a sphere

For a spinning sphere, a 1-D heat conduction model was assumed, meaning that heat was assumed to be conducted only in the radial direction. Consider the above diagram.

When we apply Fourier law to a spherical shell, the heat transfer between i and $i+1$ nodes is expressed as follows [54].

$$\dot{Q} = \frac{4\pi k R_i R_{i+1}}{R_{i+1} - R_i} (T_{i+1} - T_i) \quad (3.33)$$

Where,

k : thermal conductivity (W/m-K, function of temperature)

T : temperature of each node (K)

If we use the concept of conductor (G), Eq (3.33) is expressed as;

$$\dot{Q} = G(T_{i+1} - T_i) \quad (3.34)$$

$$G = \frac{4\pi k R_i R_{i+1}}{R_{i+1} - R_i} \quad (3.35)$$

Using Eq (3.34) the temperature of each node can be calculated as;

$$Q_{in} = G_i(T_{i+1} - T_i)\Delta t \quad (3.36)$$

$$Q_{out} = G_{i-1}(T_i - T_{i-1})\Delta t \quad (3.37)$$

$$T_j = T_{j-1} + (Q_{in} - Q_{out})/(m_i c_{p,i}) \quad (3.38)$$

Where,

i : node index

j : time index

t : time (sec)

m_i : mass of ith node (kg)

c_{p,i} : specific heat of material in ith node (J/kg-K, function of temperature)

The surface temperature is calculated using the temperature of outermost node and the net heat flux to the surface as [27, 53];

$$T_w = \frac{\dot{q}_{net} A_{s,i\max}}{G_{i\max}} + T_{i\max} \quad (3.39)$$

Where,

A_s : surface area of object (m²)

imax : index of outermost node

Chapter 3

\dot{q}_{net} : net heat flux from aerothermodynamics module (W/m²)

3.1.4.2 Heat conduction of cylinders

Applying Fourier law to a cylinder, the heat transfer between i and $i+1$ nodes in radial direction is expressed as follows [54];

$$\dot{Q} = \frac{2\pi kL}{\ln(R_{i+1}/R_i)}(T_{i+1} - T_i) \quad (3.40)$$

Where,

L : length of cylinder (m)

R_i : radius of i^{th} node (m)

Using the concept of conductor (G), Eq. (3.40) can be expressed as Eq. (3.34) with

$$G = \frac{2\pi kL}{\ln(R_{i+1}/R_i)} \quad (3.41)$$

The temperature of each node and surface can be calculated using Eqs (3.36) ~ (3.39) as in sphere model.

3.1.4.3 Heat conduction of boxes

The 1-D heat conduction model was applied to the flat plate after stretching the six faces of the box. If the Fourier law is applied to the flat plate, the heat transfer per unit time between i and $i+1$ nodes is expressed as follows [54];

$$\dot{Q} = \frac{kA}{(x_{i+1} - x_i)}(T_{i+1} - T_i) \quad (3.42)$$

Where,

A : area of the flat plate (m²)

x_i : coordinate in thickness direction of i^{th} node (m)

Using the concept of conductor (G), Eq. (3.42) can be express as Eq. (3.34) with

$$G = \frac{kA}{(x_{i+1} - x_i)} \quad (3.43)$$

The temperature of each node and surface can be calculated using Eqs (3.36) ~ (3.39) as in sphere model.

3.1.5 Ablation module

As the temperature of an object rises, the outer layer will eventually reach the melting point of the material. After the melting temperature is reached, the surface temperature is held constant and the heat into each layer is tracked with time. If the total heat absorbed into the outer layer meets or exceeds the heat of ablation for the material, the layer is assumed to be removed by aerodynamic shear forces and the next layer is assumed to face the aerothermodynamic heating. The following equation is the condition for a layer to demise.

$$Q_{absorbed,i} > H_{ablation,i} = m_i \left(h_{f,i} + \int_{T_{init,i}}^{T_{melt,i}} c_{p,i}(T) dT \right) \quad (3.44)$$

Where,

$Q_{absorbed,i}$: net absorbed heat to i^{th} node or layer (J)

$H_{ablation,i}$: heat of ablation for i^{th} node (J)

m_i : mass of i^{th} node (kg)

$h_{f,i}$: heat of fusion for the material in i^{th} node (J/kg)

$T_{init,i}$: initial temperature of i^{th} node (K)

$T_{melt,i}$: melting point of the material in i^{th} node (K)

$C_{p,i}(T)$: specific heat of the material in i^{th} node (J/kg-K)

The mass and size of the object change after the layers remove and this change is applied to the other modules such as trajectory module. It was assumed that the

material does not produce gases which might affect the aerothermodynamic heating to the surface for simplicity.

3.2 Program validation

3.2.1 Comparison with ORSAT and SCARAB analysis on simple-shaped objects

In this section, the SAPAR code will be validated by comparing its analysis results for objects with simple shapes to results from ORSAT and SCARAB that were presented by Lips et al. [25]. They compared survival analysis results from SCARAB and ORSAT for 120 cases: 24 spheres, 48 cylinders, and 48 boxes. In their study, the diameter of the spheres or cylinders and the width of the boxes ranged from 0.25 m to 1.0 m; the length-to-width ratios for boxes or the length-to-diameter ratios for cylinders were equal to 2.0 or 5.0; and the masses of the objects were between 10 and 3700 kg. The material properties and the dimensions for each case can be found in table 5 ~ 7. The dimensions shown in table 6 are for cylinders with a length to diameter ratio (L/D) equal to 2. Similar cases were compared for length to width ratio (L/W) equal to 2 for boxes and an L/D and L/W equal to 5 for cylinders and boxes, respectively. The initial conditions are listed in Table 8. For these conditions, SCARAB and ORSAT have shown good agreement in the final results, although the two codes use completely different approaches for the trajectory simulation and the calculation of drag coefficients and heating rates. Because SCARAB cannot account for the oxidation heat flux, the ORSAT didn't include the oxidation heating in the simulation for proper comparison in their research.

Table. 5 Physical properties of spheres for code validation [25]

Case	Material	Outer Radius(m)	Inner Radius(m)	Mass(kg)
1	Al	0.125	0.075	17.318
2	Ti	0.125	0.075	28.222
3A	Gr Ep I	0.125	0.075	10.070
3B	Gr Ep II	0.125	0.075	9.945
4	Al	0.250	0.212	69.272
5	Ti	0.250	0.212	112.288
6A	Gr Ep I	0.250	0.212	40.280
6B	Gr Ep II	0.250	0.212	39.780
7	Al	0.500	0.465	276.459
8	Ti	0.500	0.465	450.525
9A	Gr Ep I	0.500	0.465	160.756
9B	Gr Ep II	0.500	0.465	158.759
10	Al	0.125	0.094	12.685
11	Ti	0.125	0.108	12.685
12A	Gr Ep I	0.125	0.029	12.685
12B	Gr Ep II	0.125	0.000	12.685
13	Al	0.250	0.244	12.685
14	Ti	0.250	0.246	12.685
15A	Gr Ep I	0.250	0.239	12.685
15B	Gr Ep II	0.250	0.239	12.685
16	Al	0.500	0.499	12.685
17	Ti	0.500	0.499	12.685
18A	Gr Ep I	0.500	0.498	12.685
18B	Gr Ep II	0.500	0.498	12.685

Chapter 3

Table. 6 Physical properties of cylinders (L/D=2) for code validation [25]

Case	Material	Outer Radius(m)	Inner Radius(m)	Mass(kg)
1	Al	0.125	0.075	47.183
2	Ti	0.125	0.075	76.890
3A	Gr Ep I	0.125	0.075	27.436
3B	Gr Ep II	0.125	0.075	27.095
4	Al	0.250	0.209	188.731
5	Ti	0.250	0.209	307.562
6A	Gr Ep I	0.250	0.209	109.744
6B	Gr Ep II	0.250	0.209	108.381
7	Al	0.500	0.462	754.925
8	Ti	0.500	0.462	1230.248
9A	Gr Ep I	0.500	0.462	438.975
9B	Gr Ep II	0.500	0.462	433.523
10	Al	0.125	0.115	12.685
11	Ti	0.125	0.119	12.685
12A	Gr Ep I	0.125	0.106	12.685
12B	Gr Ep II	0.125	0.106	12.685
13	Al	0.250	0.248	12.685
14	Ti	0.250	0.249	12.685
15A	Gr Ep I	0.250	0.246	12.685
15B	Gr Ep II	0.250	0.246	12.685
16	Al	0.500	0.499	12.685
17	Ti	0.500	0.500	12.685
18A	Gr Ep I	0.500	0.499	12.685
18B	Gr Ep II	0.500	0.499	12.685

Table. 7 Material properties of objects for code validation [25]

Material	Density (kg/m ³)	Melting point(K)	Heat of fusion (J/kg)	Specific heat (J/kg-K)	Conductivity (W/m-k)	emissivity
Graphite epoxy I (ablator)	1570	700	1.61×10^7	1100	110	0.86
Graphite epoxy II	1550.5	700	236.6	879	0.87~6.4	0.9
Aluminum	2700	850	3.9×10^5	1100	140	0.3
Titanium	4400	1950	4.7×10^5	600	15	0.25

Table. 8 Initial conditions of simulation

Altitude	122 km
Relative velocity	7.41 km/s
Relative flight path angle	-0.1°
Orbital inclination	28°
(Longitude, Latitude)	(0°, 0°)

Figures 3.10, 3.11, and 3.12 show the impact masses and demise altitudes of spheres, cylinders, and boxes predicted by ORSAT, SCARAB, and SAPAR. It is noted that the profiles predicted by the SAPAR code are in excellent agreement with the results of SCARAB and ORSAT for the impact masses and the demise altitudes. The coefficient of determination (R^2) presented in the figures is a statistical parameter that indicates the closeness of the points to the trend line; i.e., if all the points lie on the line, R^2 should be 1.0. It can be seen that the values of R^2 for the three figures are very close to unity, and that the trend lines have slopes of nearly unity. This means the SAPAR results are almost identical to those of SCARAB and ORSAT.

Chapter 3

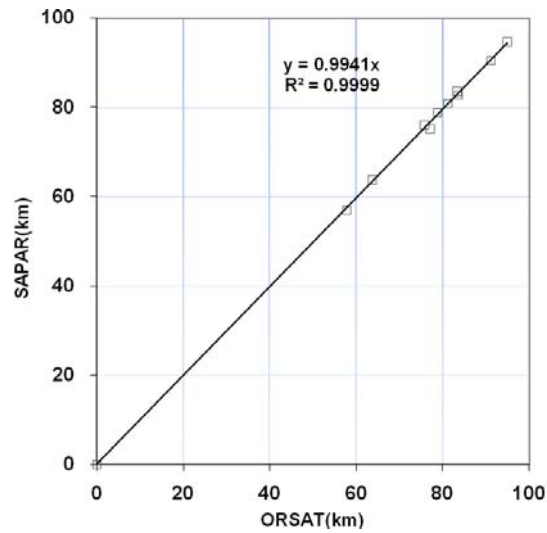


Fig.3.10 Comparison of demise altitudes for spheres predicted by ORSAT [25] and SAPAR

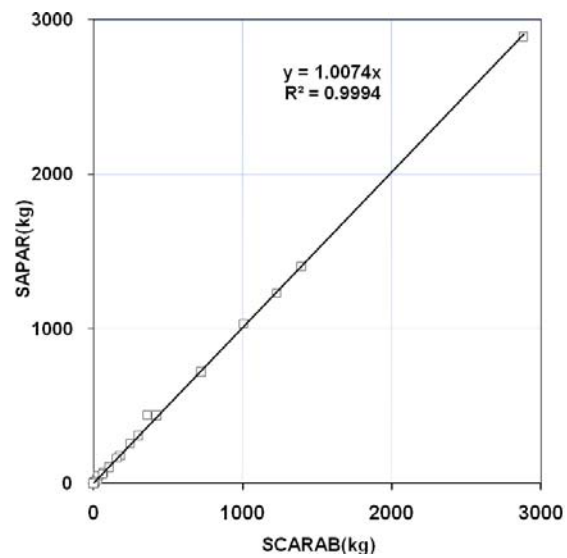


Fig.3.11 Comparison of impact masses for cylinders predicted by SCARAB [25] and SAPAR

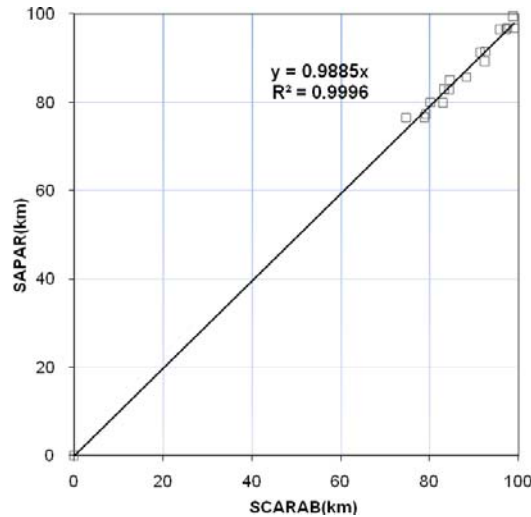


Fig.3.12 Comparison of demise altitudes for boxes predicted by SCARAB [25] and SAPAR

3.2.2 Comparison with actually recovered space debris

The Delta II rocket was launched on April 24, 1996 and the 2nd stage of this rocket reentered the atmosphere on January 22, 1997 [23, 55]. Two fragments survived entry; a stainless steel cylindrical propellant tank which landed near Georgetown, Texas and a titanium helium-pressurization sphere which landed near Seguin, Texas [23]. Rochelle et al. [23, 31] presented two similar results (Fig. 17 in [23] and Fig. 16 in [31]) based on detailed survival analysis using ORSAT 5.0. These analyses coincided with real measurements in that they predicted the survival of the cylindrical propellant tank during reentry. On the other hand, for the surface temperature of the tank, the ORSAT results were different than those of Ailor et al [16]. They performed micro-structural analysis on the recovered tank and concluded that the peak overall reentry temperature of the tank was between 1473 and 1553 K, which is much lower than the melting temperature of stainless steel (1700 to 1750 K). In contrast, ORSAT [23, 31] predicted

Chapter 3

that the object would reach the melting temperature and remain at that state for more than 70 seconds.

The cause of the discrepancy in the results from ORSAT and the experimental measurement was investigated in this research and a revised equation for reradiation heat loss was suggested [35]. Using the proposed equation for reradiation heat loss and applying a practical value for thermal emissivity, the SAPAR code predicted the maximum temperature of the Delta-II second stage cylindrical tank reentering the Earth's atmosphere that is in good agreement with the Ailor's analysis [16].

The total absorbed heat of cylindrical bodies in ORSAT can be expressed by Eq. (3.45), where the lateral surface area (πDL) is used as the reference surface area neglecting the heat loss in the end caps. On the other hand, if we take into account the reradiation heat loss of the end caps (assuming that the temperature of the end caps is similar to that of lateral surface), the total absorbed heat of the cylindrical body can be expressed by Eq. (3.46). Because a 1-D heat conduction model was employed in ORSAT and SAPAR, Eq. (3.46) is believed to be more realistic than Eq. (3.45). By comparing Eqs. (3.45) and (3.46), it should be noted that the ignored heat loss in ORSAT plays a significant role when the reradiation heat flux is comparable to the net heat flux and the length-to-diameter ratio (L/D) is small.

$$\begin{aligned} Q_{total} &= A_{surf} \times \int \dot{q}_{net} dt \\ &= \pi DL \times \int \dot{q}_{net} dt = \pi DL \times \int (\bar{\dot{q}}_{hw} + \dot{q}_{ox} - \dot{q}_{rr}) dt \end{aligned} \quad (3.45)$$

$$\begin{aligned} Q_{total} &= \int [(\dot{q}_{hw} + \dot{q}_{ox}) \times \pi DL - \dot{q}_{rr} \times (\pi DL + 0.5\pi D^2)] dt \\ &= \pi DL \times \int \left[\dot{q}_{net} - \dot{q}_{rr} \times \frac{1}{2L/D} \right] dt \end{aligned} \quad (3.46)$$

Figure 3.13 shows the temperature profiles predicted using the revised reference area for reradiation heat loss based on Eq. (3.46). The predicted temperature using a higher-fidelity Systems Improved Numerical Differencing Analyzer (SINDA) [55]

model is also shown in Fig. 3.13. In the SINDA calculation, the sum of the hot-wall and the oxidation heat fluxes from ORSAT analysis [31] was given as the heating condition and the reradiation heat loss via the whole surface was considered based on the surface temperature calculated by the SINDA code. Both the SINDA and the SAPAR codes with Eq. (3.46) and the emissivity of 0.3 predicted maximum temperatures slightly below the melting point of stainless steel, 1714K and 1721K respectively. On the other hand, the ORSAT result showed that the tank would be at the melting temperature and continuously ablated from 40 to 120 s. Almost the same profile as that of ORSAT was produced by the SAPAR code with Eq. (3.45) and the emissivity of 0.3 as seen in Fig. 3.13. The temperature difference between the results of SINDA and SAPAR with Eq. (3.46) and the emissivity of 0.3 after 100 s from breakup can be primarily attributed to a difference in the trajectory. The SINDA code used the heat flux profiles by Rochelle et al. [31] such that the object would be ablated during reentry and undergo greater deceleration compared to the result of SAPAR with Eq. (3.46), in which the ablation did not occur.

The reentry survival analysis can be significantly affected by the emissivity of material [27]. However, the prediction of the accurate emissivity of an object is very difficult because it is dependent on the temperature, the level of oxidation, and roughness of the surface etc. A case study was performed in this paper to investigate the effect of the thermal emissivity on reentry survival analyses for Delta-II second stage stainless steel tank, and to find out the emissivity for the peak temperature of this cylindrical tank to agree with that by Ailor et al. [16]. The analyses by SAPAR with Eq. (3.46) and the emissivity from 0.46 to 0.57 predicted that the peak temperature would be within the peak temperature range Ailor et al. [16] suggested.

The emissivity of 0.8 is the mean value for the oxidized stainless steel [27] which is well manufactured in a furnace with enough oxygen and time. Hence, the effective emissivity for Delta-II second stage stainless steel tank, which were in oxidation process in rarefied air condition for a short time, should be much lower than 0.8. In this light, it is believed that the analysis by SAPAR with Eq. (3.46) is reasonable in that the

result agreed well with the analysis by Ailor et al., when using the emissivity from 0.46 to 0.57 as was stated above.

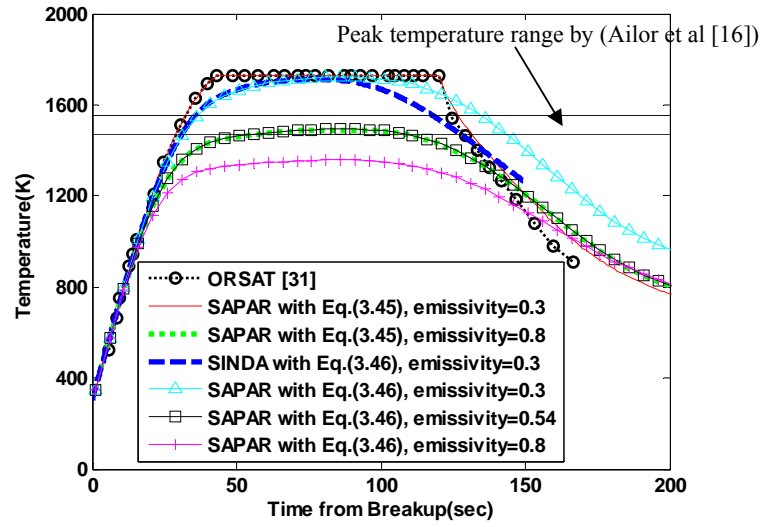


Fig.3.13 Temperature vs. time for Delta-II second stage cylindrical tank

Figure 3.14 shows the heat fluxes as functions of the flight time for Delta-II second stage cylindrical tank computed by ORSAT and SAPAR. As can be seen in the figure, SAPAR results showed good agreement with those from ORSAT when the same equations for reradiation heat flux (Eq. 3.45) was used. However, when the revised equation (Eq. 3.46) was used, the net heat flux profile is lower than that of ORSAT due to the more reradiation heat loss as explained in the above paragraphs. It can be seen that the convective hot wall heat flux by the SAPAR calculation with Eq. (3.46) and emissivity of 0.3 is larger than others after 100 seconds. It can be attributed to the difference in the trajectory i.e. the velocity of the object. In this case of calculation, the object wasn't ablated at all and underwent smaller deceleration compared to the result of ORSAT or SAPAR with Eq. (3.45), in which the ablation occurred and the mass of the object decreased.

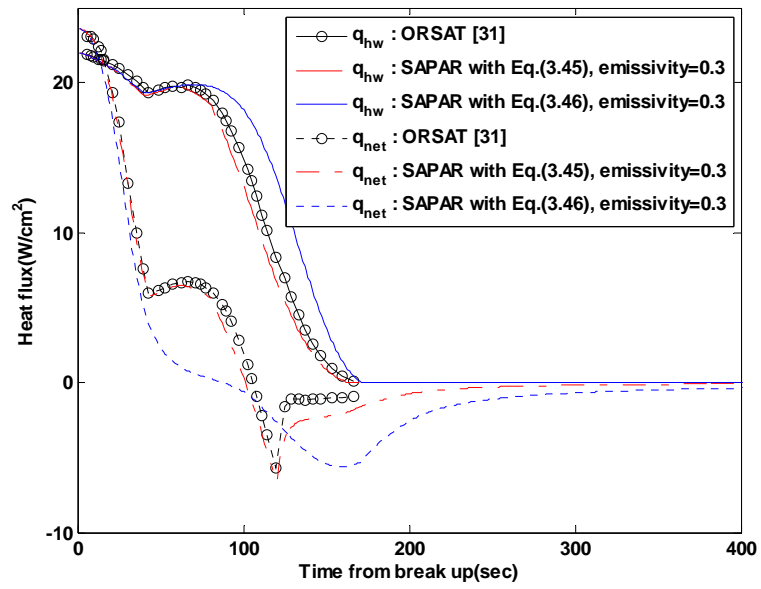


Fig.3.14 Heat fluxes vs time for Delta-II second stage cylindrical tank

Chapter 4. Flight safety analysis on the upper stage of a launch vehicle

Flight safety analysis on the upper stage of a sample 2-stage launch vehicle is conducted in this chapter. Because the vehicle velocity is very high in this flight phase, the flight safety analysis accounting for the demise of the debris is considered. To this end, the SAPAR code was put into the FSAS program in the procedure of trajectory simulation of falling debris. The resulting combined procedure for the flight safety analysis used in this chapter is already depicted in Fig. 1.5.

The sample launch vehicle analyzed in this chapter was assumed to be launched in southern area of South Korea to the southern direction. The first stage is assumed to be powered by a liquid propellant rocket engine while the second stage be thrust by a solid propellant kick motor. A small satellite is assumed to be inserted into a circular orbit with an altitude of 300 km.

The flight safety analysis will be conducted over the area of east Australia that the launch vehicle's IIP (Instantaneous Impact Point) trajectory passes through at second stage thrusting phase of the vehicle. Various flight conditions are considered in the analyses such as the launch azimuth and wind profiles etc.

4.1 Launch vehicle configuration and trajectory

4.1.1 Main mass characteristics

The mass data of the launch vehicle are presented in table 9. The total mass at lift-off is about 141 ton of which 13% (about 18 ton) is for structure. The fuel mass of first and second stages are 121 ton and 1.6 ton respectively. The payload fairing to protect the payload from aerodynamic load in early stage of the flight weighs 500 kg. The satellite mass is 100 kg.

Table. 9 Mass characteristics of the launch vehicle

Parameter	Mass, kg
LV	
LOC(Lift-Off Contact) moment	140800
Before separation of stage I	19300
After separation of stage I	2300
Before separation of SC	700
Stage I	
Structure with equipments	17000
Propellant	121000
Stage II	
Structure with equipments	600
KM Propellant	1600
Payload Fairing	500
Spacecraft	100

4.1.2 Mission definition and sequence

Table 10 shows the mission condition of the launch vehicle. The vehicle is launched in Naro space center located in southern area of Korean peninsula with launch azimuth of 160 or 165 degree. The satellite achieves perigee and apogee altitude of 300 km at KM burn out with 70 or 75 degree of inclination angle.

Table 11 shows the flight event of the launch vehicle. The vehicle starts pitch program at 10 sec after lift-off and reaches Mach 1 at 60.1 sec. The payload fairing separates from the vehicle at 210 sec and the first stage liquid rocket engine (LRE) shuts down at 226 sec. Four seconds after the first stage engine shuts down, the first stage separates from the second stage of the vehicle. The second stage kick motor

Chapter 4

ignites at 400 sec after lift-off and burns for 112 seconds. Finally the satellite will be inserted into the low earth orbit at 512 second after lift-off.

Table. 10 Mission condition of the launch vehicle

Launch Site	Name	Naro Space center
	Coordinates	Latitude: 34.43N deg Longitude: 127.54E deg Altitude: 100.0 m
	Launch azimuth	160 or 165.0 deg
Payload Mass		100.0 kg
Mission Orbit	Perigee altitude	300 km
	Apogee altitude	300 km
	Inclination	70 or 75 deg

Table. 11 Flight event sequence of the launch vehicle

Event	Time (sec)	V_{relative} (m/sec)	Altitude (km)	Range (km)
LOC	0.0	0	0.1	0
End of vertical flight	10.0	30	0.2	0
Mach 1	60.1	311	7.3	2
Q Max	72.1	426	11	4
PLF Separation	210.0	4123	114	261
LPE cutoff	226.0	4665	135	327
Stage separation	230.0	4464	140	344
KM ignition	400.0	4359	285	1064
KMBO	512.0	7588	302	1668

4.1.3 Flight trajectory and parameters

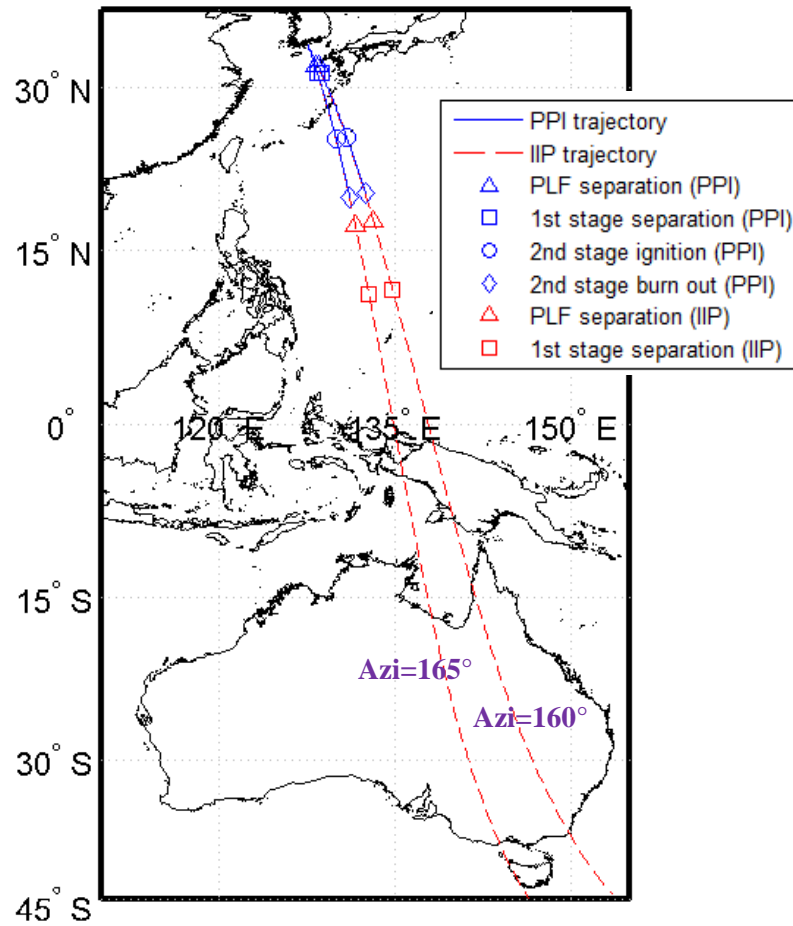


Fig.4.1 Launch vehicle PPI and IIP trajectory

Figure 4.1 shows the trajectories of present position indicator (PPI) and instantaneous impact point (IIP) of the launch vehicle with launch azimuths of 160 and 165 degrees. The jettisoned 1st stage was assumed to fall in west Pacific near Philippine and the IIP trajectory of the upper stage was assumed to overfly the east Indonesia and Australia. It can be seen in the figure that the PPI is only on the latitude of 20 degree at the time of burn-out of 2nd stage motor when the vehicle reaches orbit velocity.

Figures 4.2 to 4.5 show the vehicle flight parameters such as vehicle altitude, velocity, and acceleration. The vehicle reaches 300 km altitude at the velocity of

Chapter 4

7.6km/s where the satellite separates from the vehicle. At that point the vehicle downrange is about 1670 km. The LRE (liquid rocket engine) of first stage decrease its thrust at 150 sec after lift-off to lower the maximum acceleration level of the vehicle as can be seen in Fig. 4.5.

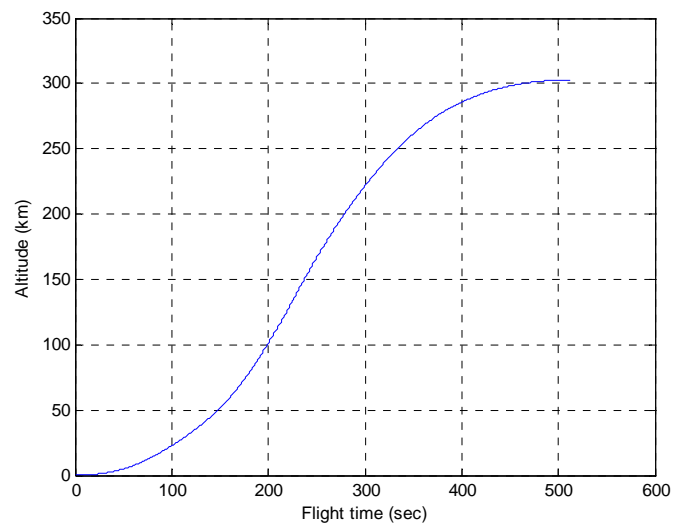


Fig.4.2 Altitude above Earth ellipsoidal surface vs. flight time

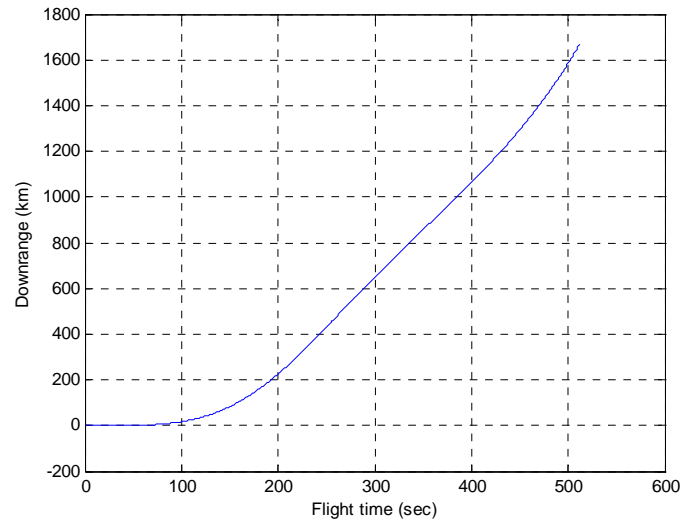


Fig.4.3 Downrange vs. flight time

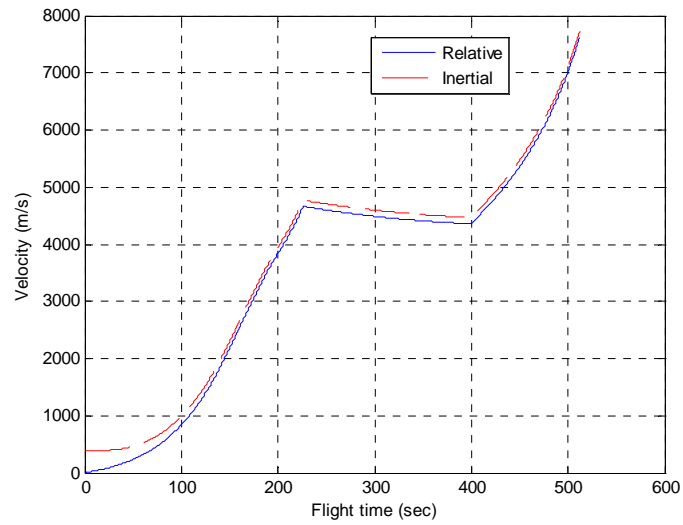


Fig.4.4 Velocity vs. flight time

Chapter 4

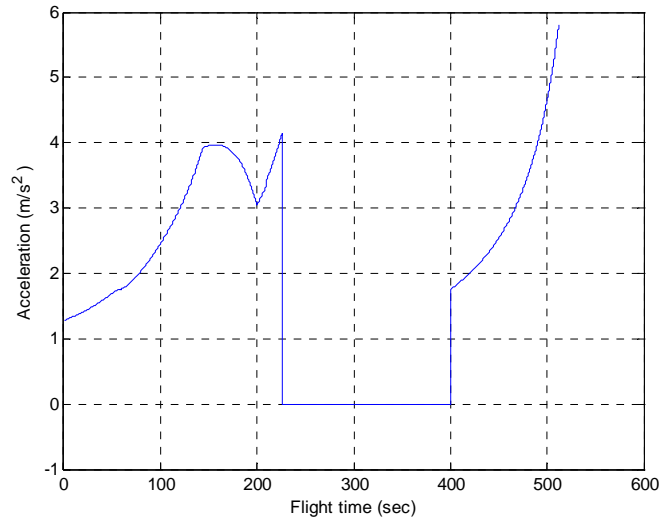


Fig.4.5 Acceleration vs. flight time

Figures 4.6 to 4.9 show the vehicle's uncertainties in position and velocity due to guidance and performance error for flight time from 250 sec to 512 sec. The 3-sigma errors for latitude and longitude are assumed to be about 0.2 degree and 0.1 degree respectively at burn out of 2nd stage motor. The altitude 3-sigma error is about 5 km and the velocity 3-sigma error is about 50 m/s at 2nd engine burn out.

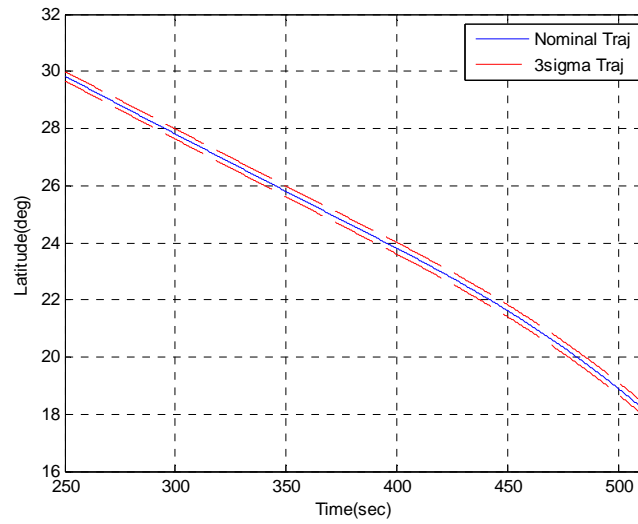


Fig.4.6 Vehicle nominal and 3-sigma position (latitude)

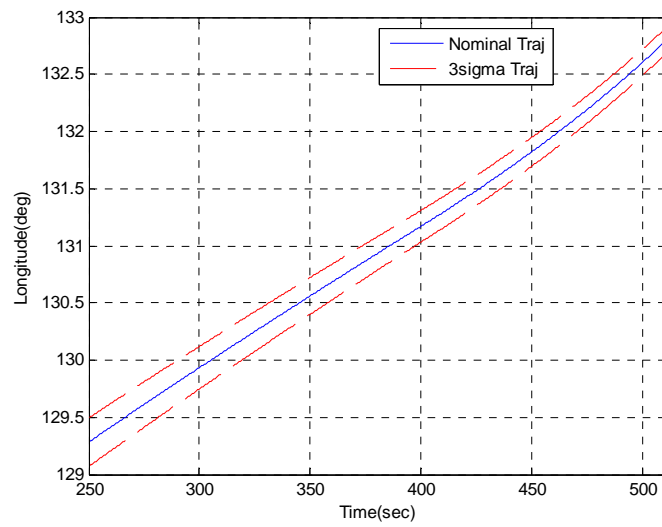


Fig.4.7 Vehicle nominal and 3-sigma position (longitude)

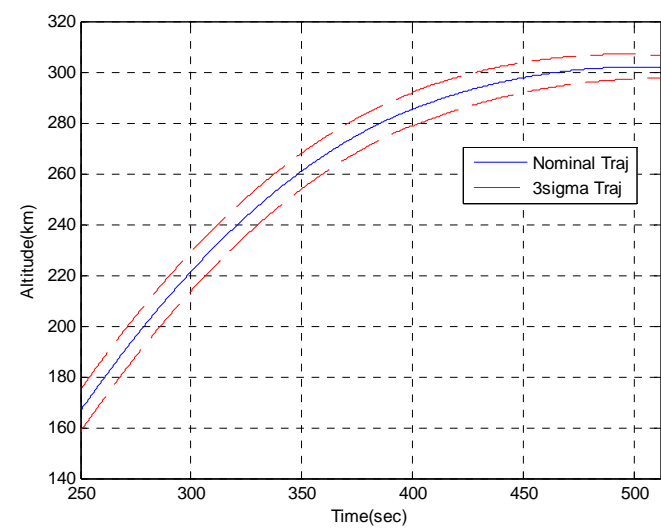


Fig.4.8 Vehicle nominal and 3-sigma position (altitude)

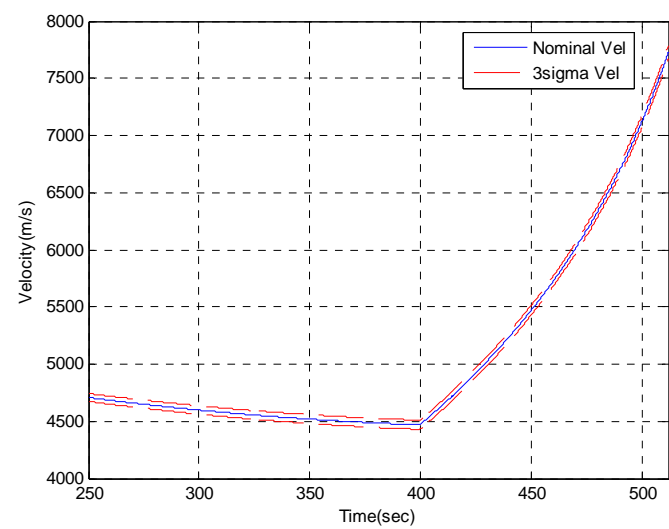


Fig.4.9 Nominal and 3-sigma Velocity

4.1.4 Population near trajectory

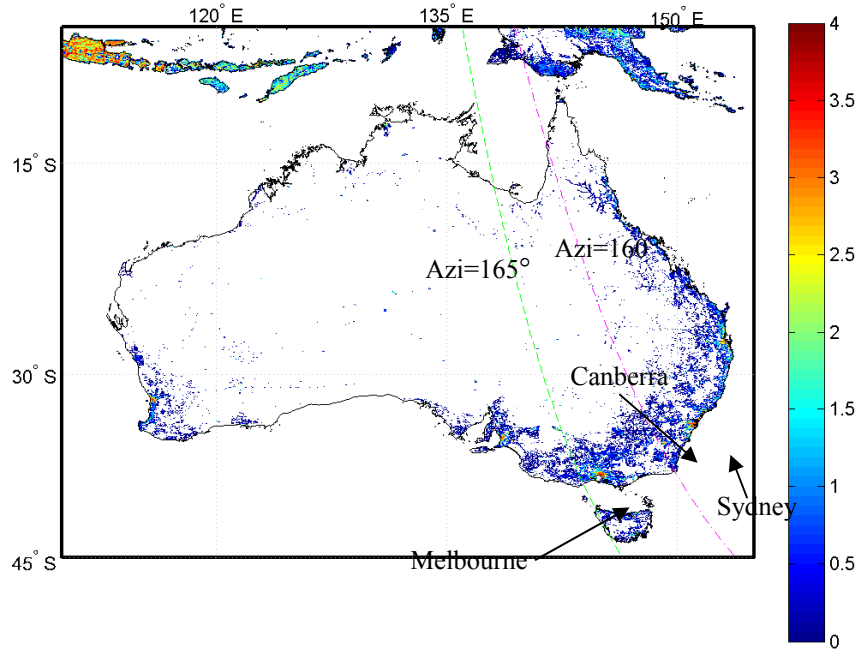


Fig.4.10 Australia population density ($\log_{10}(\text{pop}/\text{km}^2)$) near IIP trajectory

Figure 4.10 shows the population distribution of Australia near IIP trajectory of the vehicle. Here, the LandScan 2005 [44] was used as the world population model. It can be seen that the IIP trace of launch azimuth of 165 degree passes by Melbourne on the left side while 160 degree IIP trace lies between Melbourne and Sydney adjacent to Canberra. The population of Melbourne is about 3.7 million while that of Canberra is about 0.3 million. The population of Sydney is about 4.3 million. The Ec is expected to be high in these areas near IIP trajectory.

4.2 Conditions for flight safety analysis

4.2.1 Debris model

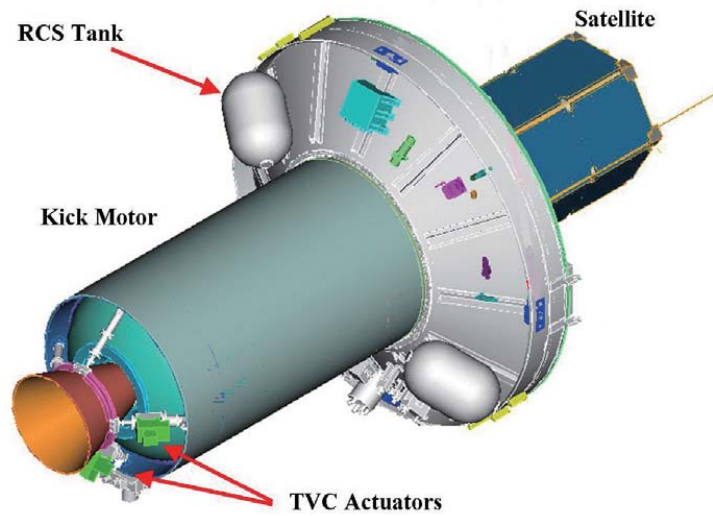


Fig.4.11 Configuration of KSLV-I upper stage [57]

The upper stage of the launch vehicle which is analyzed in this paper is assumed to be resembling that of KSLV-I (Korea Space Launch Vehicle-I). Only the size and the mass of the structure and fuel are assumed to differ from those of KSLV-I upper stage. Figure 4.11 shows the upper stage of KSLV-I [57].

The upper stage of the launch vehicle is assumed to disintegrate at the time of explosion. The fragments are simulated including the survivability analysis from the fail time to the time they reach the altitude of 20km, below which the IIP (Instantaneous Impact Point) module of FSAS (Flight Safety Analysis System) is applied to determine the impact point location. Six fragment groups are considered in the analysis; KM(Kick Motor) case, KM(Kick Motor) nozzle, KMS(Kick Motor Support) structure, electronic boxes, RCS(Reaction Control System) tanks, and satellite.

Some fragment groups have only one fragment, while others have several pieces of debris.

In the survivability analysis, the concept of parent-child fragment hierarchy [27, 56] was used. Parent fragments are modeled as containers and children as components inside the containers. If the container demises, then the internal components are released and exposed to aerodynamic heating. In this case, the number of fragments usually increases and the survivability analysis are applied to the new fragments. In practice, if the outer graphite epoxy of the KM case fully ablates, then the inner heat-resistant component is assumed to be exposed to aerodynamic heating. Electronics box is assumed to be composed of the 4.0kg container and an inner component of 6.0 kg. RCS tank is assumed to have inner aluminum tank wrapped by graphite epoxy. The satellite was assumed to be composed of container of 20 kg and 8 inner boxes weighing 10 kg each. KMS structure is assumed to be shaped as a cylinder composed of KMS, fairing joint, adapter ring, and payload adapter etc. Table 12 shows the fragment model analyzed in this paper. The total mass of fragments considered is 604 kg which is about 86.3% of the whole mass of the upper stage (600kg) and the satellite (100kg).

The analysis of survivability of reentering object is heavily affected by the material of the object. Table 13 shows the material property of the fragment used in this research. The properties for CC (Carbon-carbon reinforced material) were used instead of the resistant material of the KM case, EPDM. Because these two materials have high resistant abilities against the heat, they both survive the reentry in this research, not affecting the final expected casualty results.

Table. 12 Debris model of the upper stage of the launch vehicle

Fragment Level-1	Fragment Level-2	Material	Qty	Shape	Dimension, m	Mass, kg
KM case	KM Case	Epoxy	1	Cyl	D=1.2, L=1.5 Thick=0.0074	90

Chapter 4

	Heat-resistant part	EPDM	1	Cyl	D=1.19, L=1.48, Thick=0.0041	50
KM nozzle	KM nozzle	Carbon-carbon reinforced	1	Cyl	D=0.4, L=0.7, Thick=0.0251	40
KMS+other structure	KMS+other structure	Aluminum	1	Cyl	D=2.4, L=0.5, Thick=0.0058	200
Electronic box	Container	Aluminum	10	Box	L=0.3, W=0.2, Thick=0.0048	4×10=40
	Inner component	Aluminum	10	Box	L=0.2, W=0.15, Thick=0.0166	6×10=60
RCS tank	Outside wrapper	Epoxy	2	Cyl	D=0.4, L=0.5 Thick=0.0076	10×2=20
	Inside tank	Aluminum	2	Cyl	D=0.38, L=0.48 Thick=0.0009	2×2=4
Satellite	Container	Aluminum	1	Box	L=1.0, W=0.6, Thick=0.0024	20
	Inner component	Aluminum	8	Box	L=0.3, W=0.2, Thick=0.013	10×8=80
Sum						604

Table. 13 Material properties [25, 26]

Material properties	Epoxy	Aluminum	Carbon-carbon reinforced
Density, kg/m ³	1550.5	2700	1570
Melting point,	700	850	700
Heat of fusion, J/kg	236	390000	16000000
Oxidation	0.0	0.5	0.0

efficiency			
Heat of oxidation, J/kg-O ₂	-	34910934	-
Conductivity, W/(m-K)	6.4	218~248	110
Specific heat, J/(kg-K)	879	791~1034	1100
Emissivity	0.9	0.26	0.86

In the survivability analysis, 5 nodes are usually used for aluminum material and 10 nodes are used for graphite epoxy material due to its low conductivity. When the shell is very thin, 1 or 2 nodes are also used. The initial temperatures of the fragments are assumed to be 300K.

4.2.2 Statistical Analysis

For the analysis on the expected casualty (E_c) of the Australia from the failure of the launch vehicle, the vehicle is assumed to fail on each second from 496 to 507 sec when the vehicle's IIP's are on or near the landmass of Australia. The probability of failure occurring during one second interval is assumed to be $1.0e-3$. Monte-Carlo simulations for each of explosion velocity, ballistic coefficient, and guidance and performance uncertainties are conducted 500 times for each fail time. In calculation of impact footprints of space launch vehicles, vehicles with explosive payload, or reentry spacecrafts, simulation times between 100 and 1000 are usually used in Monte-Carlo method [12, 58-60]. As can be seen in Fig. 4.12, the number of simulation, 500 times, was found to be sufficient because further increase in simulation times did not significantly affect the size of the debris footprint for all the fragment groups. Only the failure mode for the launch vehicle to explode during 2nd stage thrusting phase is

Chapter 4

considered in this research for simplicity.

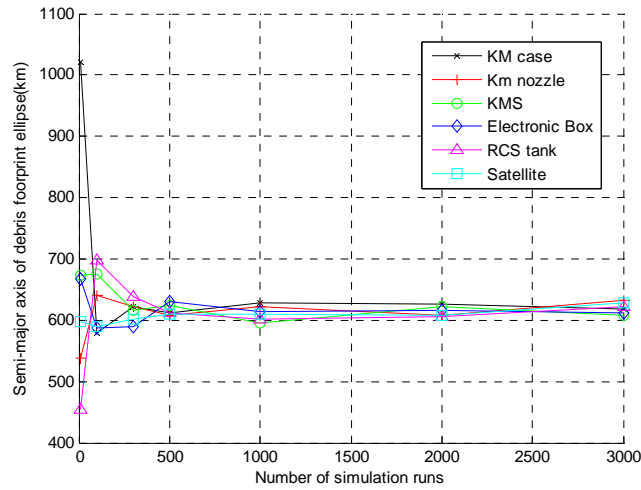


Fig.4.12 Semi-major axes of debris footprint ellipses of all the fragment groups vs. number of simulation runs for 506 sec fail case

4.2.3 Wind profile of Australia

The impact point of the launch vehicle fragment can be affected by wind profiles. The monthly wind data for east Australia are used in this research. GRAM95 (NASA/MSFC Global Reference Atmospheric Model-1995) [38] was used as the wind model. Figure 4.13 to 4.24 show the wind profile data used in this research. U means the velocity toward eastern direction while V is due north. It should be noted that because of the very low air density in high altitudes, the wind in low altitude is important in the impact point prediction.

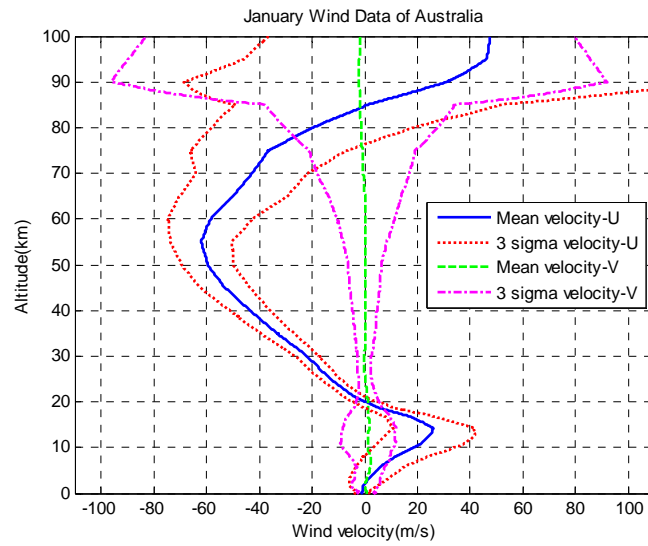


Fig.4.13 January wind profile of Australia

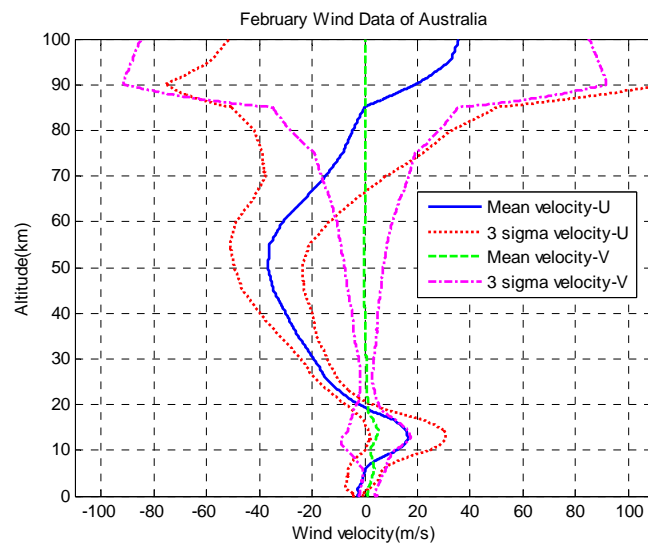


Fig.4.14 February wind profile of Australia

Chapter 4

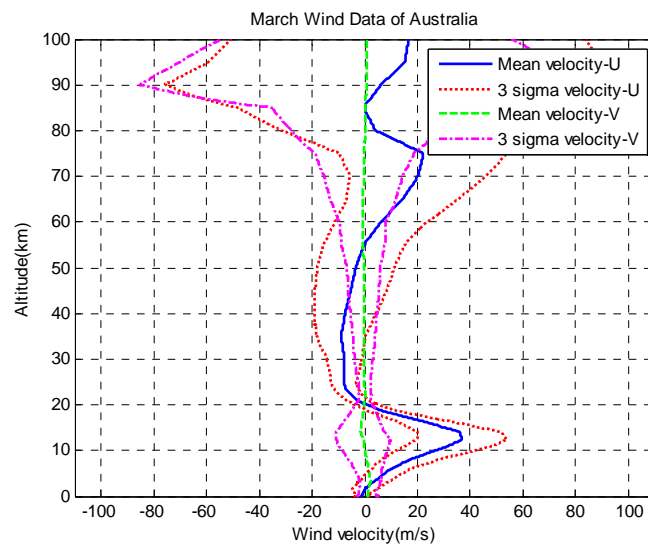


Fig.4.15 March wind profile of Australia

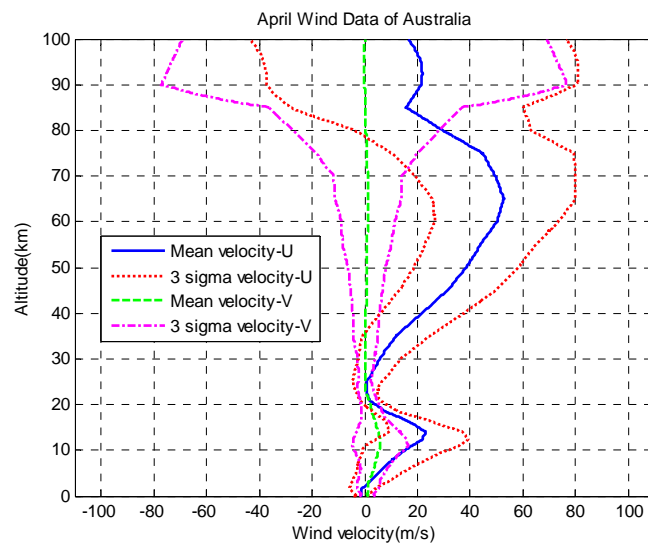


Fig.4.16 April wind profile of Australia

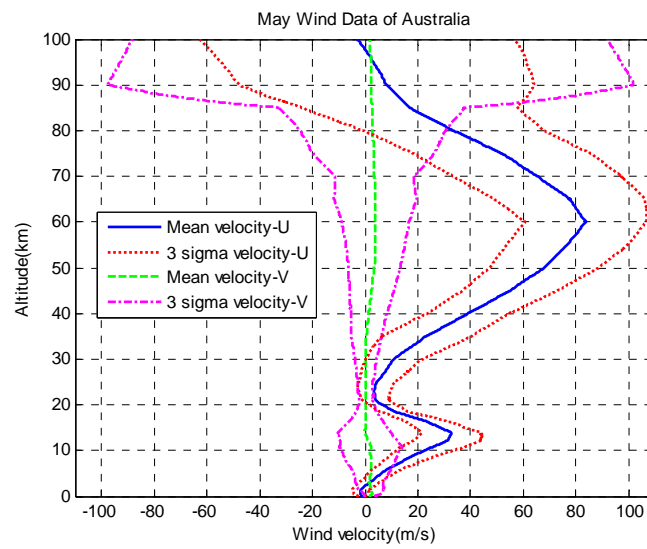


Fig.4.17 May wind profile of Australia

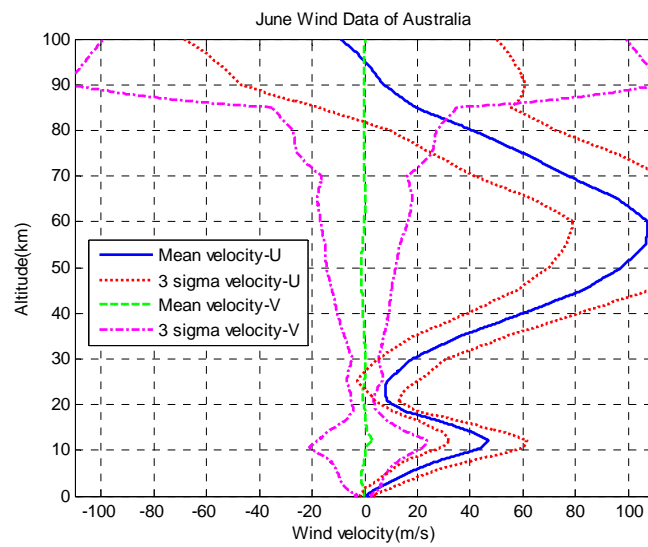


Fig.4.18 June wind profile of Australia

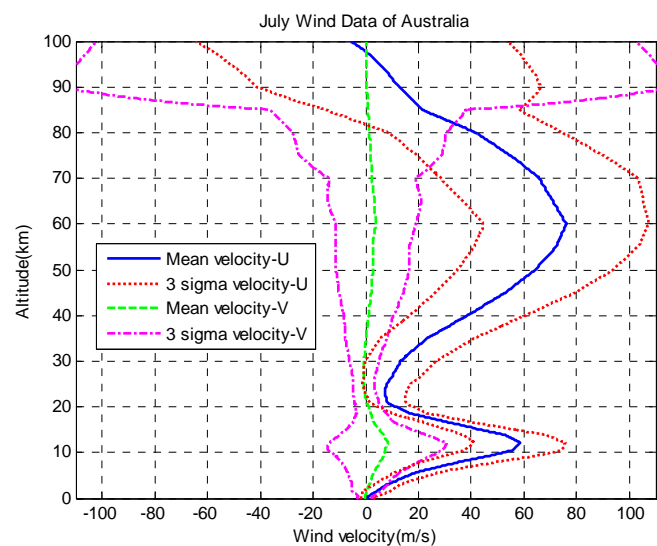


Fig.4.19 July wind profile of Australia

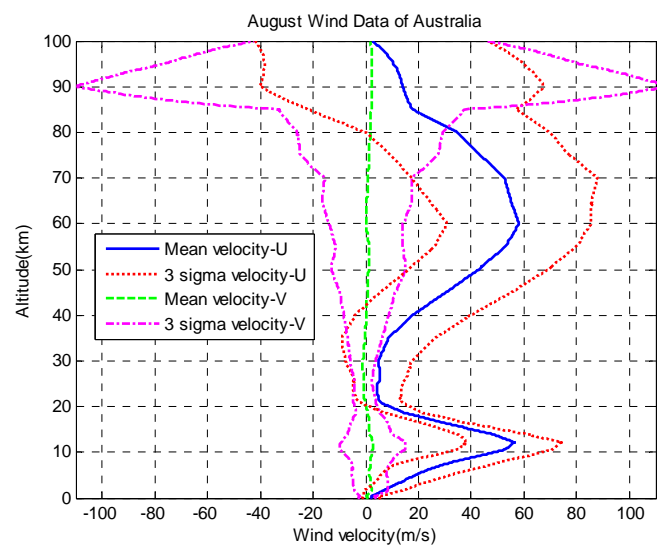


Fig.4.20 August wind profile of Australia

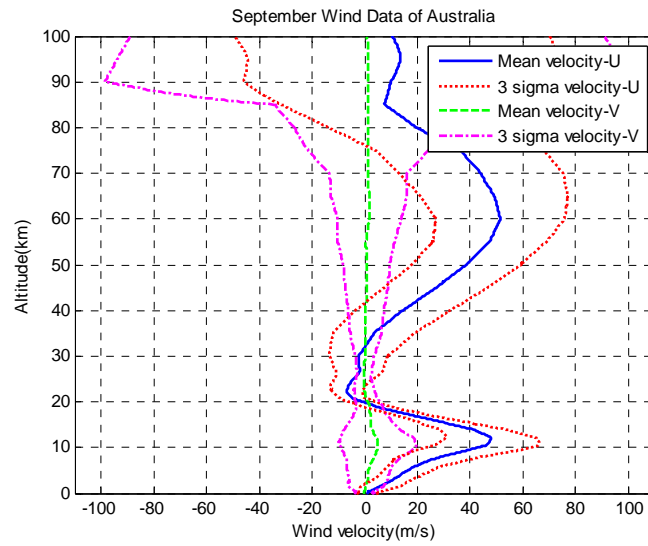


Fig.4.21 September wind profile of Australia

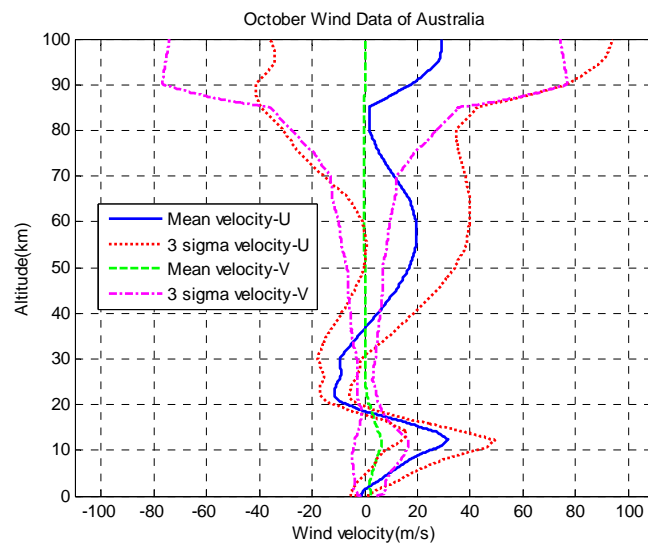


Fig.4.22 October wind profile of Australia

Chapter 4

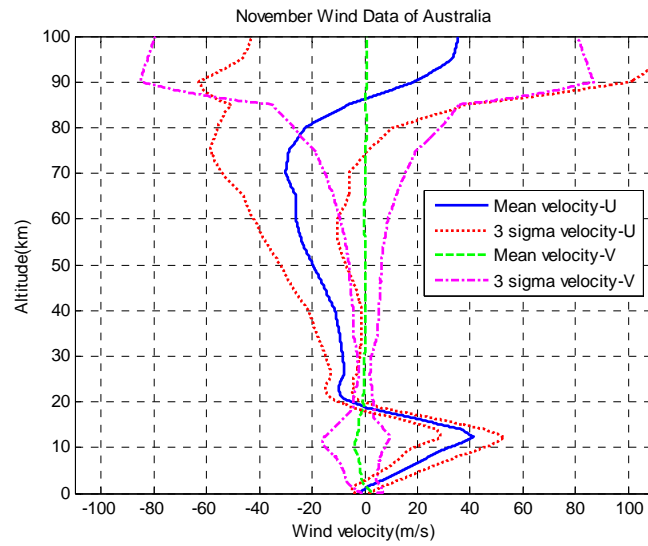


Fig.4.23 November wind profile of Australia

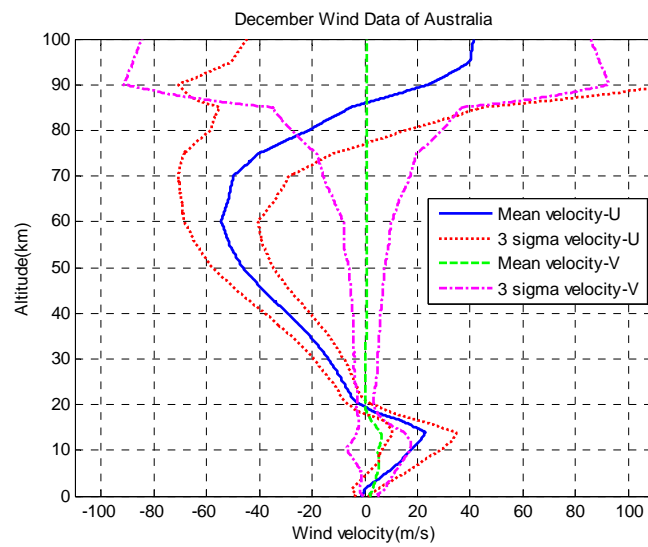


Fig.4.24 December wind profile of Australia

4.3 Flight safety analysis on the upper stage

4.3.1 Survivability analysis

4.3.1.1 Survivability analysis for fail time of 505 sec

In this section, in order to investigate the survivability analysis results in detail, the results for specific fail time are presented for the case of 165 degree launch azimuth. The July wind profile was used in the simulation. In Figs. 4.25 and 4.26, the altitudes of the fragments are plotted as a function of downrange from the launch site for the case where the vehicle fails at 505 sec after lift-off. The altitude and velocity of the vehicle at 505 sec are 302 km and 7.25 km/s respectively. In the figures, the simulations were conducted assuming zero imparted velocity by explosion, no guidance and performance error, mean ballistic coefficients of the fragment groups, and mean wind profile for July.

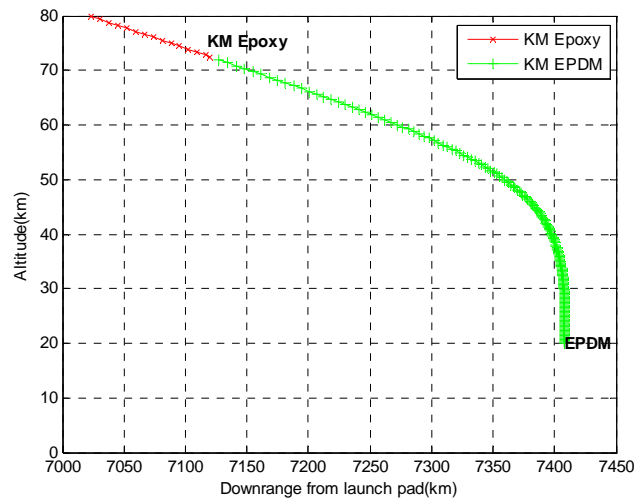


Fig.4.25 Altitude for KM case fragment vs. downrange for 505 sec fail case

Chapter 4

In order to see the result for the parent-child debris concept, the result of the KM case was presented in Fig. 4.25. After KM epoxy case is fully ablated at 72 km altitude, the heat-resistant component made of EPDM is exposed to convective heating and falls to the ground without any ablation due to its high heat capacity. Because the survivability analysis of the fragment was conducted only for the altitude above 20 km, the graph is drawn to that altitude.

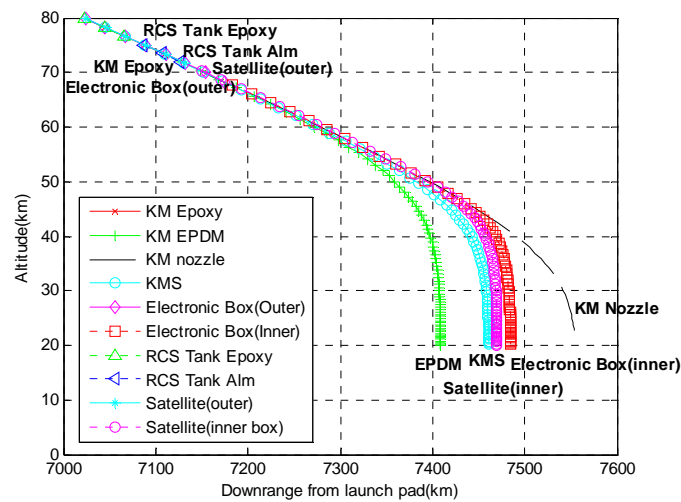


Fig.4.26 Altitude for all fragment groups vs. downrange for 505 sec fail case

Figure 4.26 shows the altitude of all the fragments from the launch vehicle as a function of downrange from the launch site. It can be seen that several fragments are predicted to demise; outer skin of RCS tank made of epoxy demises at an altitude of 77 km, KM case made of Epoxy demises at 73 km, RCS inner tank made of aluminum demises at 72 km, outer container of satellite made of aluminum demises at 72 km, and aluminum outer container of electronic box demises at 68 km. Other fragments (KM EPDM, KMS, satellite inner components, inner components of electronic boxes, and KM nozzle) are predicted to survive the reentry and impact the ground. Although they are predicted to survive the reentry, it is computed that some portions of the fragments would demise and the resulting sizes and masses of the fragments would be decreased

compared with their initial state.

Figure 4.27 shows the velocity-altitude map for all fragments. Fragments with large ballistic coefficient like KM nozzle is predicted to remain at high velocity to relatively low altitude. However, all fragments including KM nozzle decelerate steeply below 30 km altitude because of high air density. The velocities of the fragments reach about 300 m/s ie. Mach 1 at an altitude of 20 km. Because convective heating in this level of object speed is negligible, the survivability analysis can be omitted below 20 km with little effect to final results.

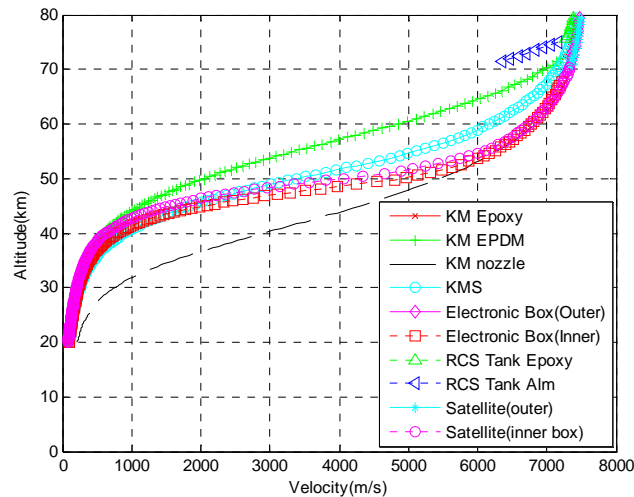


Fig.4.27 Velocity-altitude map of all fragment groups for 505 sec fail case

Figure 4.28 shows the surface temperatures of the fragments as a function of altitude. It can be seen that the surface temperatures begin to rise around the altitude of 100 km where the air particles are dense enough to heat the object. As the fragments penetrate into low altitudes, the surface temperatures rise to the melting points of the materials and stay there. If the net heat absorbed meet or exceed the heat of fusion for the material, the object demises. If the absorbed heat is not enough to fully ablate the object and the velocity reduces due to aerodynamic drag, the surface temperature

Chapter 4

decreases when the reradiation heat flux is larger than the convective heat flux. Because the initial temperatures are assumed to be 300 K for all the fragments, the temperatures of child fragments begin to rise from 300K when they are exposed to convective heating after the outer containers demise.

Figure 4.29 shows the mass variation of the fragments as a function of the altitude. KM epoxy, satellite outer container, electronic box container, and RCS tanks are predicted to fully demise. KMS structure begins to fall with the initial mass of 200 kg and starts to melt at the altitude of 57km but doesn't fully demise to impact the Earth surface with the mass of 120 kg. KM nozzle and KM EPDM don't melt at all remaining at their initial mass during free fall. In this figure the mass of the parent structure means the summed one of the parent and child fragment.

Figure 4.30 shows the demise factor for each fragment which is defined as the ratio of the absorbed heat divided by the heat of ablation of the object. When the demise factor becomes close to 100%, the amount of melting portion increases and when it reaches 100% the object is fully demised. It can be seen that demise factors of the inner parts of the electronic boxes and the satellite are close to 100%. These components would demise at higher fail velocities of the vehicle, i.e. when the vehicle fails in later time than 505 sec. The demise factors for KM nozzle and KM EPDM are lower than 10% meaning almost no ablation, because these objects are designed to resist the high heating rate.

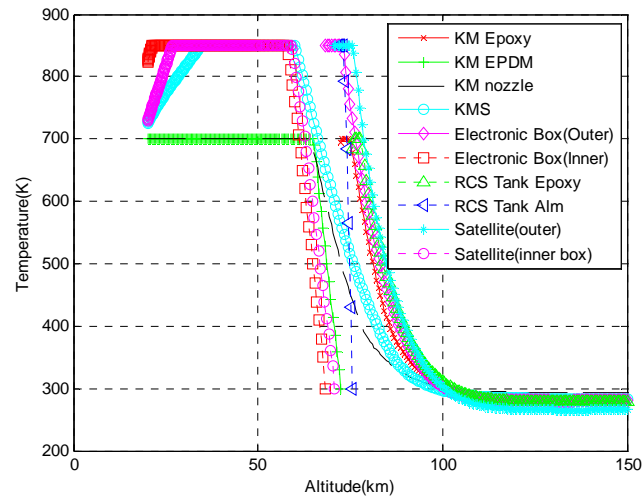


Fig.4.28 Surface temperatures for all fragment groups vs. altitude for 505 sec fail case

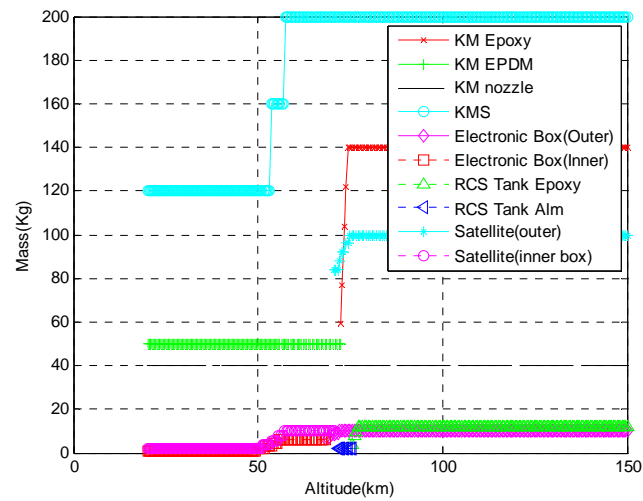


Fig.4.29 Mass of all fragment groups vs. altitude for 505 sec fail case

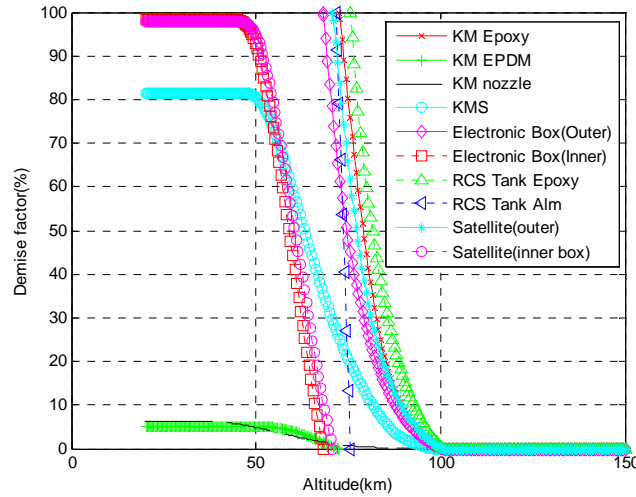


Fig.4.30 Demise factor of all fragment groups vs. altitude for 505 sec fail case

4.3.1.2 Survivability analysis according to vehicle fail time

In this section, in order to investigate the effect of the initial velocity on survivability analyses, the results for KM nozzle were compared according to the vehicle fail time i.e. the initial velocity of the fragment. Figure 4.31 shows the heat fluxes for various vehicle fail time and initial velocities as functions of the time. It should be noted that time in abscissa is shifted for the time of maximum heat flux to be located on zero. It can be seen that the earlier the vehicle fail time is i.e. the lower the initial velocity of the object is, the higher the maximum convective heat flux becomes. The maximum convective heat flux for the case when the vehicle fail velocity is 6836 m/s is about 88 W/cm^2 , while when the vehicle fails at the velocity of 7531 m/s the maximum convective heat flux is only about 78 W/cm^2 . However except for the maximum heat flux regime, the higher the initial velocities of the object become, the higher the heat fluxes are. Hence, the whole heat load integrated for the total falling time becomes larger when initial velocity increases, resulting in higher demise factor.

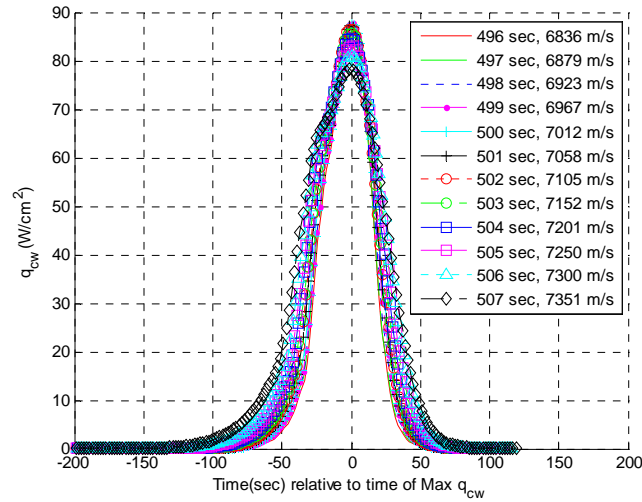


Fig.4.31 Heat flux of KM nozzle vs. time for various vehicle fail time and velocities
(time in abscissa is shifted for the time of maximum heat flux to be zero)

Figure 4.32 shows demise factors of KM nozzle vs. time which is shifted for the time of maximum heat flux to be zero for various fail time i.e. initial velocities. It can be seen that the higher the initial velocities are, the larger the demise factors become for the whole time range as stated before. If the initial flight velocity of the object is higher, the object starts to absorb the heat much earlier than the maximum heat flux time (time in abscissa is zero) and hence the demise factor is larger for the whole time range.

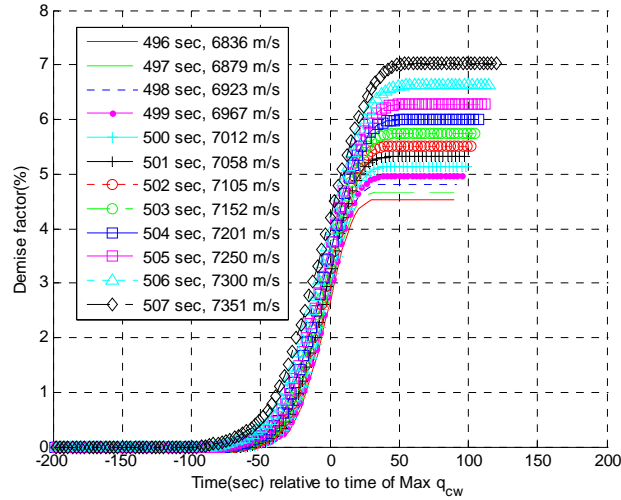


Fig.4.32 Demise factor of KM nozzle vs. time for various vehicle fail time and velocities (time in abscissa is shifted for the time of maximum heat flux to be zero)

The maximum heat flux level was seen to be lower when the initial reentry velocity of an object was higher in Fig. 4.31. In order to find the cause of this phenomenon, graphs showing heat flux vs. altitude and altitude vs. velocity (velocity-altitude map) were presented in Figs. 4.33 and 4.34. In Fig. 4.33, it can be seen that the altitudes for maximum heat fluxes lie between 50 and 60 km while the altitudes for maximum heat fluxes are increasing when the initial velocity becomes higher. In velocity-altitude map (Fig. 4.34), when the initial velocity is higher, the object is seen to decelerate more in the altitude above 60 km. As a result, when the initial velocity is higher, the actual velocity becomes lower in the altitude region below 60 km where the maximum heat fluxes occur, resulting in lower maximum heat flux level. This means that the object with higher velocity decreases more in high altitude where the heat flux is relatively low, and in some altitude region (50~60 km) where the air density is high enough to generate the large heat flux, the velocity becomes lower than the other objects with smaller initial velocity.

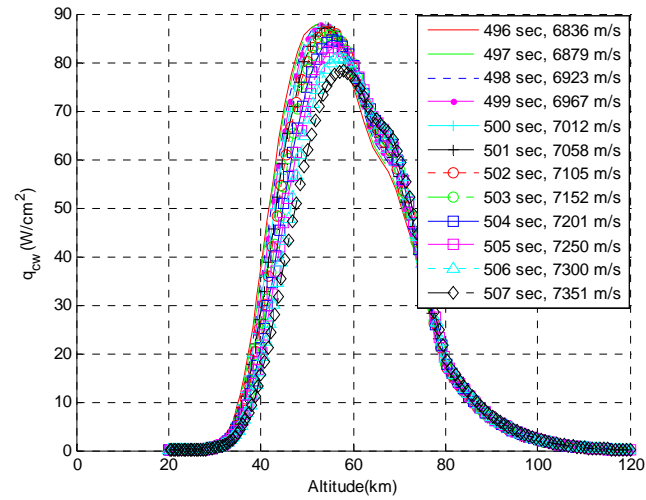


Fig.4.33 Heat flux of KM nozzle vs. altitude for various vehicle fail time and velocities (time in abscissa is shifted for the time of maximum heat flux to be zero)

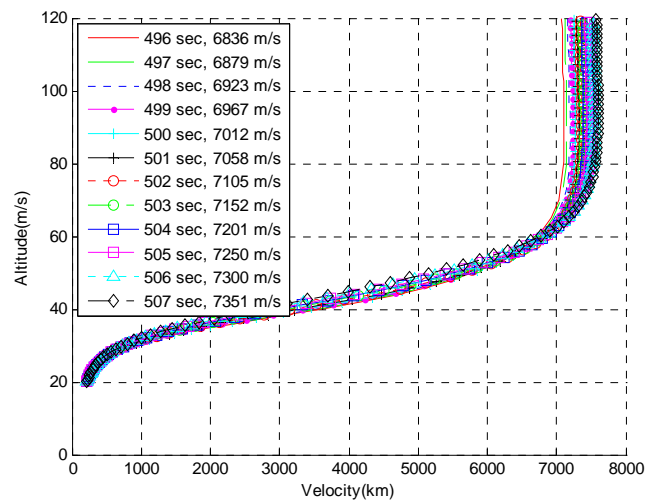


Fig.4.34 KM nozzle velocity-altitude map for various vehicle fail time and velocities (time in abscissa is shifted for the time of maximum heat flux to be zero)

Chapter 4

In Fig. 4.35, the altitudes are plotted as a function of downrange from the launch pad. It is seen that the impact distance becomes very large by big step as the initial velocity grows higher. This is because when the vehicle's velocity approaches the orbit velocity, the impact distance is heavily affected by the initial velocity. In Fig. 4.34, it was shown that when the initial velocity was higher, the object was more decelerated at high altitude (above 60 km). It can be partly explained as follows; as can be seen in Fig. 4.35, the object with higher initial velocity reenters the Earth's atmosphere with smaller flight path angle to fly longer distance in high altitude, resulting in larger total deceleration that is integrated for the flying time.

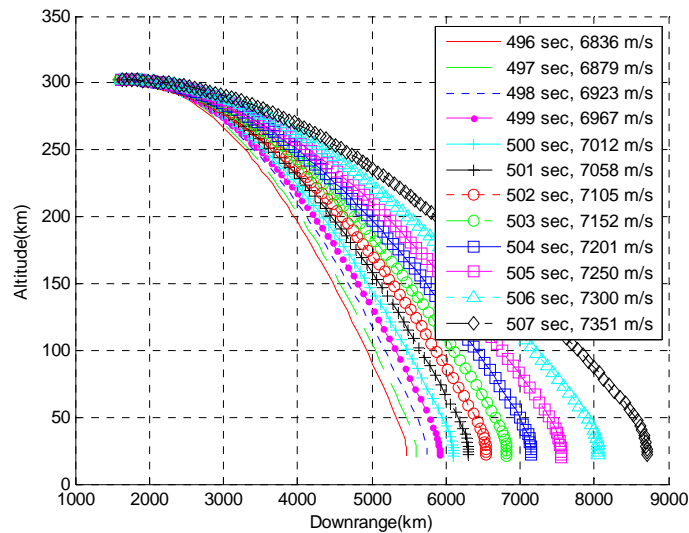


Fig.4.35 Altitude of KM nozzle vs. downrange from launch pad for various vehicle fail time and velocities (time in abscissa is shifted for the time of maximum heat flux to be zero)

In Fig. 4.32, it was seen that the demise factor for KM nozzle becomes higher with increasing initial velocities. Figure 4.36 shows the maximum demise factors for all fragment groups as a function of the initial velocity. KM epoxy, RCS tank, and outer

containers of satellite and electronic boxes are predicted to be fully demised at all velocities above 6836 m/s with demise factor of 100 %. Inner components of satellite and electronic boxes are analyzed not to be fully melted at lower velocities but fully demised at velocities above about 7300 m/s.

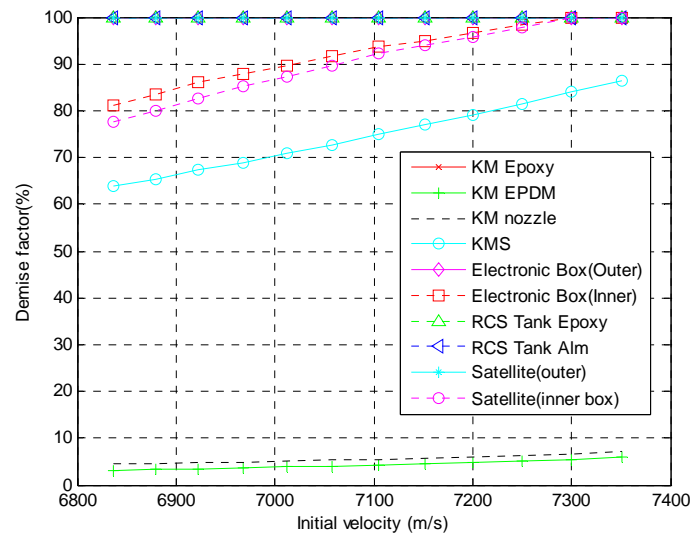


Fig.4.36 Demise factors of all fragment groups vs. initial velocity

4.3.2 Expected casualty analysis

4.3.2.1 Not considering fragment demise (Without SAPAR)

In this section, the expected casualty for Australia was analyzed assuming the fragments do not melt at all during free fall and impact the ground in their initial state. The fragments considered are KM case, KM nozzle, KMS structure, electronic boxes, RCS tank, and satellite as in the survivability analysis. Masses, ballistic coefficients, and casualty areas for fragment groups according to sheltering levels are presented in table 14. Because survivability analyses are not considered, fragment masses, casualty

Chapter 4

areas and ballistic coefficients are all the same irrespective of fail time. In this table, the casualty areas for wood or light metal are larger than for open in some fragment groups due to the secondary fragments from the buildings when the fragments penetrate the roofs.

Table. 14 Debris model of the upper stage of the launch vehicle

Fragment group	Mass per fragment, kg	Ballistic Coeff. Kg/m ²	Qty	Casualty area per fragment, m ²				
				Open	Wood	Light metal	Composite	Reinforced concrete
KM case	140	90.4	1	11.24	20.29	19.52	2.29	1.61
KM nozzle	40	166.1	1	3.67	7.46	2.91	0.87	0.87
KMS	200	51.5	1	22.53	22.74	20.69	1.79	0.98
Electronic box	10	158.7	10	2.03	1.78	0.63	0.54	0.60
RCS tank	12	69.8	2	3.3	1.45	0.29	0.77	0.61
Satellite	100	158.7	1	5.49	14.74	7.44	1.86	1.41

Figure 4.37 shows the 3-sigma impact areas of all the fragment groups for the fail time between 496 and 507 sec for the case of 165 degree launch azimuth. The July wind profile was used in the simulation. For the sake of visibility, the impact areas are plotted in two second interval. The impact areas in the figure are computed by combining the impact distributions by uncertainty of wind, ballistic coefficient, and guidance and performance etc. The impact distribution areas are shaped as elliptic having the long axis in the direction of the flight.

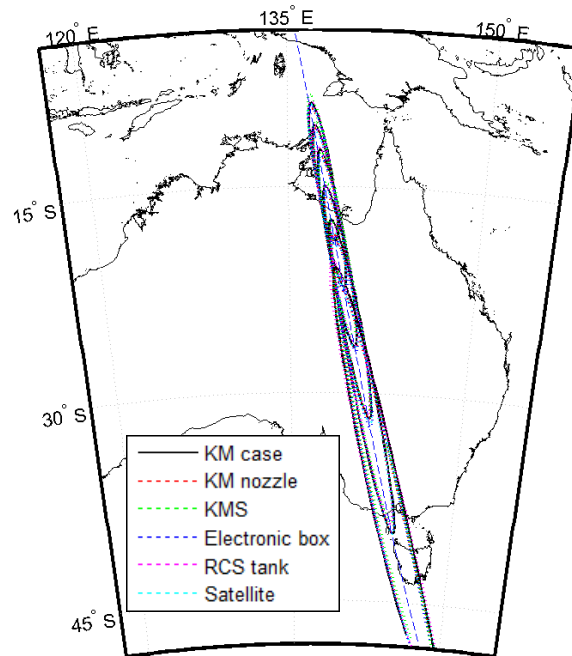


Fig.4.37 Three-sigma impact areas of all fragment groups for 496~507 fail time with July wind profile in two second interval in case of not considering the demise of debris

In Fig. 4.38, the expected casualty result per $1 \text{ km} \times 1 \text{ km}$ grid was plotted on the map with the IIP trace. It can be seen that the expected casualty is distributed near the impact areas of Fig. 4.37. The population centers shown in Fig. 4.10 have relatively high expected casualty values.

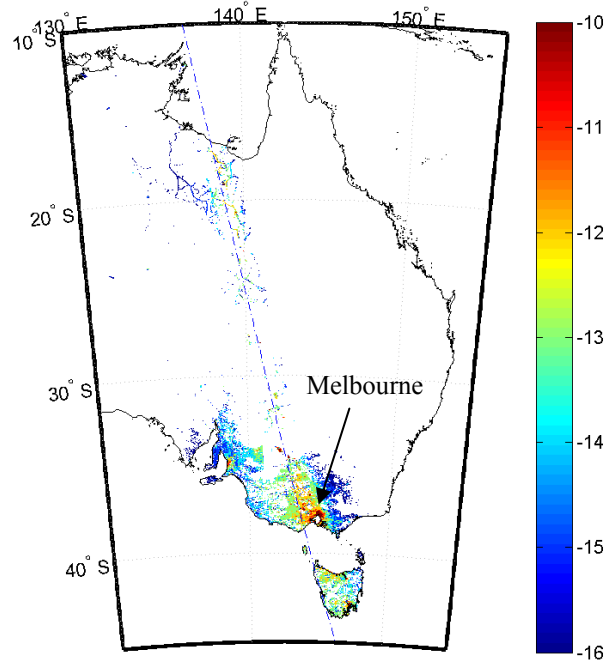


Fig.4.38 Expected casualty distribution ($\log_{10}(\text{Ec}/\text{km}^2)$) of Australia by the launch vehicle failure in 496-507 sec with July wind profile not considering the demise of debris

Figure 4.39 shows the accumulated expected casualty distribution according to the latitude. The latitude in abscissa is plotted in reverse direction because the vehicle flies to the south. Because the figure shows the accumulated Ec values, the regions where the curve rises steeply are the high risk areas. In the regime near the latitude of -19 degree, there is a small town which is only about 10 km apart from the IIP trace. One of the major cities of Australia, Melbourne, is located on the latitude of -38 degree about 150 km apart from IIP trace. Most of the Ec values are occurred in these areas as can be seen in the figure. The final expected casualty in Australia is about $9.74\text{e-}7$ when the demise of fragment isn't considered in the analysis.

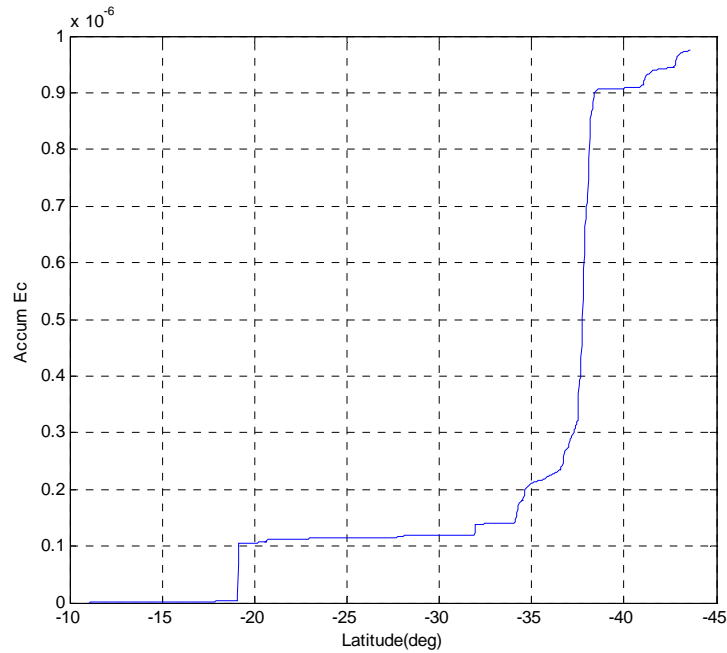


Fig 4.39 Accumulated Ec in Australia vs. latitude by the launch vehicle failure in 496-507 sec with July wind profile not considering the demise of debris

4.3.2.2 Considering fragment demise (With SAPAR)

If the fragments with high speed fully demise during the free fall by extreme heat loads, they don't pose risk to the ground lowering the Ec value. In addition, although a fragment does not fully demise, if it is partially melted away by heat load then the mass and kinetic energy of the fragment are reduced, resulting in low probability of causing damage to people on the ground. Especially when the people are protected by the structure with some sheltering level, these effects can be significant. For the sake of practical analysis, the flight safety was analyzed in this section including the sheltering effect and the survivability analysis. Fragments considered are already presented in table 12.

Chapter 4

Figure 4.40 shows the 3-sigma impact areas of all the fragment groups for the fail time between 496 and 507 sec in the case of considering the demise of debris i.e. with SAPAR calculation. For the sake of visibility, the impact areas are plotted in two second interval. As can be seen in the figure, the impact areas don't show significant difference from those presented in Fig. 4.37 where the survivability analysis isn't considered.

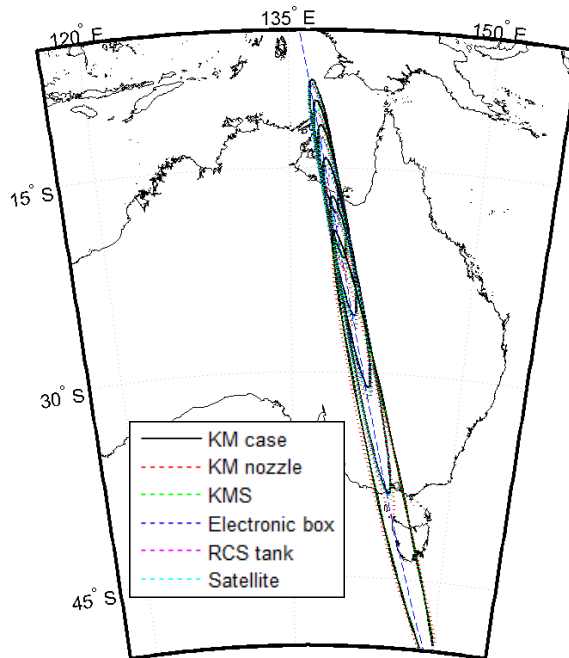


Fig.4.40 Three-sigma impact areas of all fragment groups with survivability analysis for 496~507 fail time with July wind profile in two second interval

Figure 4.41 shows the expected casualty on the map per 1 km × 1 km grid with the IIP trace. It can be seen that the expected casualty distribution is in similar trend to that of the case where demise of debris wasn't considered while the colors that represent the

Ec level are changed.

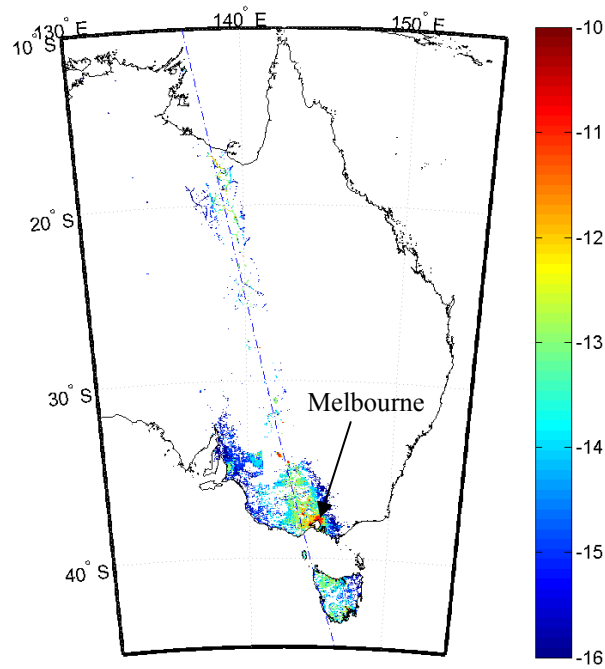


Fig.4.41 Expected casualty distribution ($\log_{10}(Ec/km^2)$) of Australia by the launch vehicle failure in 496-507 sec with July wind profile considering the demise of debris

In Fig. 4.42, accumulated expected casualty distribution was plotted as a function of the latitude. The latitude in abscissa is plotted in reverse direction because the vehicle flies to the south. Also, in order to examine the effect of including the survivability analysis, the result of the case without SAPAR is plotted in the figure. It can be seen that the final Ec value of the case where survivability analysis was considered (with SAPAR) is about $2.34e-7$ that is about 24% of the Ec for the case without SAPAR ($Ec=9.74e-7$). The difference between two cases becomes large when the latitude is smaller where the fragment falls when the vehicle fails at high velocity. This is, as was

Chapter 4

stated before, because the fragments are melted more when the initial velocities are high. So, it can be concluded that for the flight safety analysis of the upper stage of a launch vehicle flying at high speed, the survivability analysis must be considered for accurate results.

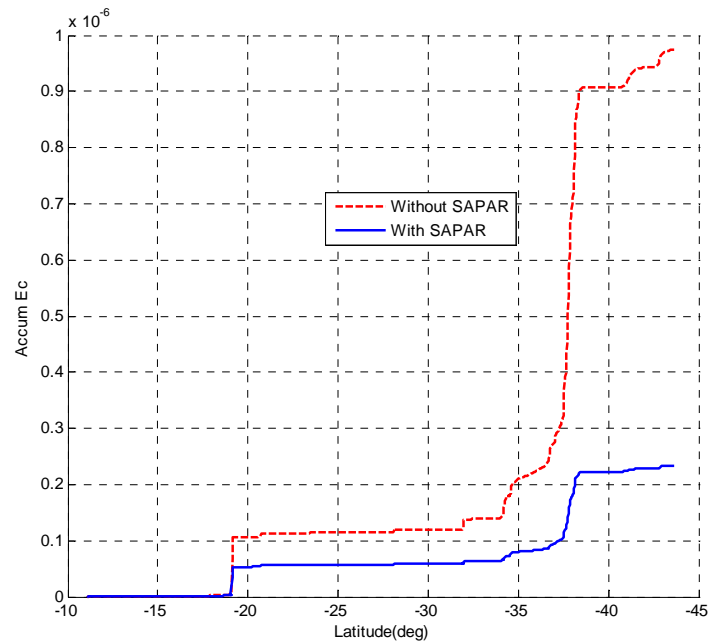


Fig.4.42 Comparison of accumulated Ec in Australia vs. latitude by the launch vehicle failure in 496-507 sec with July wind profile between the cases with and without SAPAR application

The Ec results without debris survivability analysis can be used to obtain launch licenses from the government due to their conservativeness. However, the reduction of the Ec value by considering the demise of debris turns out to be remarkable and the level of conservativeness seems to be too large. Although the Ec results of our case are about the order of 10^{-7} or 10^{-6} , the values can be much higher resulting in excess of the risk standards in other cases where IIP traces pass slowly near many big population centers. In those cases, the inclusion of the demise of fragments to the flight safety

analysis is essential to lower the Ec results while still sustaining the physical consistency. And this can result in the reduction of the development cost or time by excluding the additional activities such as the modification of the vehicle configuration or trajectory and evacuation of the residence in high risk areas.

4.3.3 Parametric study

4.3.3.1 Wind profiles

In the calculation of the previous section only the July wind profile was used. The expected casualty can be affected by the wind profiles because the impact distributions of the debris are varied by the wind. The Ec was analyzed using the wind profiles of the other months in this section. Figure 4.43 shows the accumulated Ec in Australia according to the wind profile as a function of the latitude.

The expected casualty has the maximum value of about 2.46×10^{-6} with the June wind profile while the minimum value is about 2.0×10^{-6} by the January data. The minimum Ec value is about 20% lower than the maximum value. As can be seen in the figure, the major difference in Ec result occurs in the region near latitude of $-38 \sim -37$ degree where Melbourne is located. Because Melbourne lies in the eastern side of the IIP trace of the flight with 165 degree launch azimuth as seen in Fig. 4.10, the Ec value with June wind profile which blows strongly in the eastern direction for all the altitude is highest. On the other hand, in January when the wind blows softly in the eastern direction below the altitude of 20 km and blows strongly in the western direction in the high altitude, the Ec value is the minimum because the fragments would fall more far away from Melbourne.

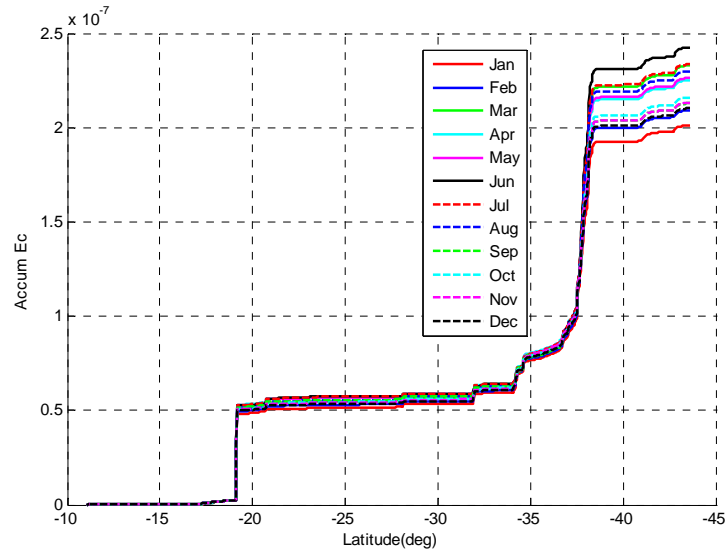


Fig.4.43 Accumulated Ec in Australia vs. latitude by the launch vehicle failure in 496-507 sec using wind profiles from January to December with SAPAR application

4.3.3.2 Imparted velocity by explosion

In the calculation of the previous section, maximum imparted velocity by explosion is assumed as 100 meter per second in each three orthogonal direction. If the perturbed velocity by explosion varies, the impact distribution areas can be enlarged or shrunk affecting the final casualty expectation. In this section, the expected casualties are analyzed varying the maximum imparted velocity by explosion in each three orthogonal direction from 50 m/s to 200 m/s. Figure 4.44 shows the accumulated Ec in Australia according to the explosion velocities of the debris as a function of the latitude. The collective Ec for the case of 50 m/s is about 1.90×10^{-7} , while for the case of 200 m/s the value is about 3.74×10^{-7} .

It should be noted that the Ec values occurred in the region near the latitude of -19 degree is largest when the imparted velocity is lowest (50 m/s) while near the Melbourne, where the altitude is about -38 degree, the Ec is largest when the imparted

velocity is highest (200 m/s). As stated before, most E_c values near -19 degree latitude are occurred in a small town which is located only 10 km apart from nominal IIP trace. In this latitude the crossrange standard deviations of the impact distributions of the fragment groups are about 15~20 km for the case of 50 m/s, while the values are about 40~50 km for the case of 200 m/s. Because the probability density function near the mean value becomes lower when the standard deviation grows bigger, the probability for the fragment groups to fall on the town near the IIP trace i.e. near the mean impact points becomes smaller when the imparted velocity by explosion grows higher.

For the area near the latitude of -38 degree the crossrange standard deviations of the impact distributions of the fragment groups are about 25~30 km when the maximum imparted velocity by explosion in each three orthogonal direction is 50 m/s, while the values are about 25~45 km, 32~90 km, and 55~145 km with the maximum imparted velocity by explosion in each three orthogonal direction of 100 m/s, 150 m/s and 200 m/s respectively. In the area near the latitude of -38 degree where Melbourne is located, the nominal IIP trace of the vehicle is about 150 km apart from the population center. Therefore, when the crossrange standard deviations of the impact distributions of the fragment groups are less than 50 km i.e. the crossrange 3-sigma is less than 150 km, the probability of the fragments falling in Melbourne is very small. For this reason, the expected casualty in this region was very small for the case of 50 or 100 m/s, while the value is relatively large for the case of 150 or 200 m/s when Melbourne is well contained in the 3-sigma impact point distribution area.

Chapter 4

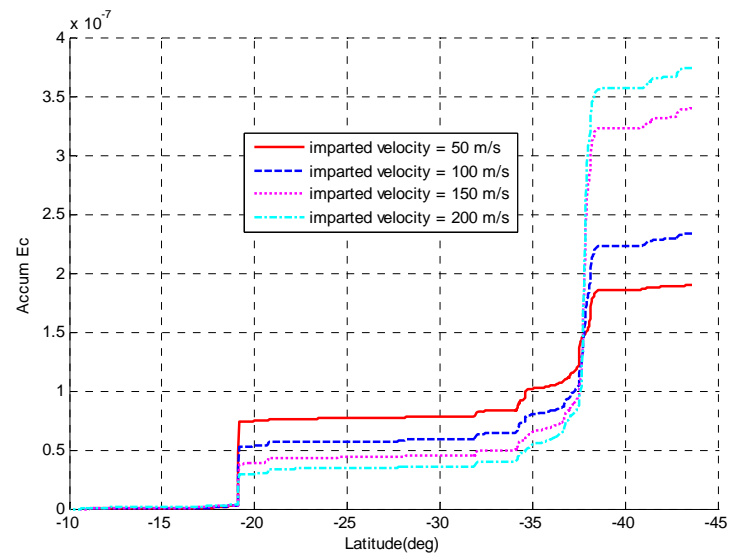


Fig.4.44 Accumulated Ec in Australia vs. latitude by the launch vehicle failure in 496-507 sec varying the maximum imparted velocity by explosion in three orthogonal direction with SAPAR application

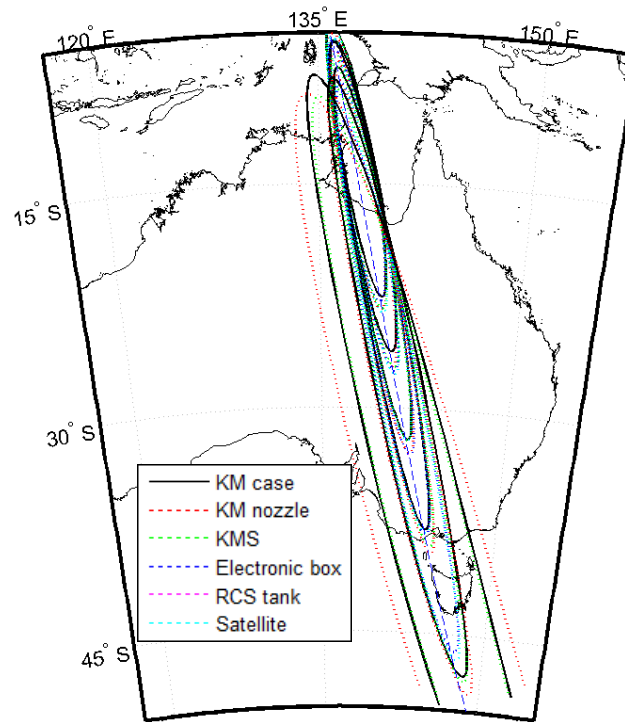


Fig.4.45 Three-sigma impact areas of all fragment groups for 496~507 fail time with July wind profile in two second interval in case of the maximum imparted velocity by explosion in each three orthogonal direction of 200 m/s with SAPAR application

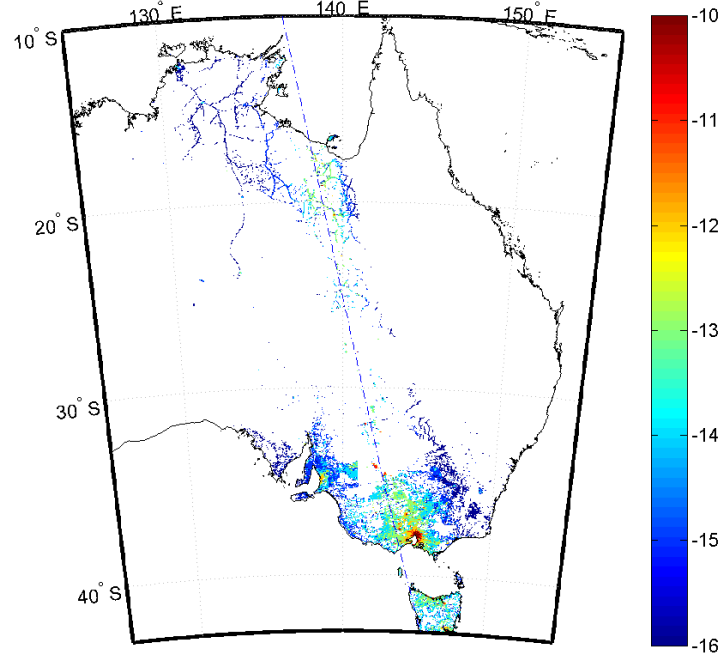


Fig.4.46 Expected casualty distribution ($\log_{10}(E_c/\text{km}^2)$) of Australia by the launch vehicle failure in 496-507 sec with July wind profile and maximum imparted velocity by explosion in each three orthogonal direction of 200 m/s with SAPAR application

4.3.3.3 Launch azimuth

The IIP trajectory has a very strong effect on the casualty expectation. When the IIP trace passes near the population center, the E_c value becomes high. In this section, the trajectory with launch azimuth of 160 degree was also analyzed in addition to the case of 165 degree. Figure 4.47 shows the accumulated E_c in Australia according to the launch azimuth as a function of the latitude. The July wind profile was used in the simulation. The maximum imparted velocity by explosion in each three orthogonal direction was assumed to be 100 m/s. The collective E_c for the case of 160 degree

launch azimuth is about $1.52\text{e-}7$, while for the case of 165 launch azimuth the value is about $2.34\text{e-}7$. When the launch azimuth is 160 degree, most Ec occurs near the latitude of -35 degree where Canberra is located as can be seen in Fig. 4.48. Because Canberra is very close to the IIP trace of 160 degree launch azimuth, although the population of the city is much smaller than that of Melbourne, the Ec value is about the same as that of Melbourne in the case of 165 degree launch azimuth.

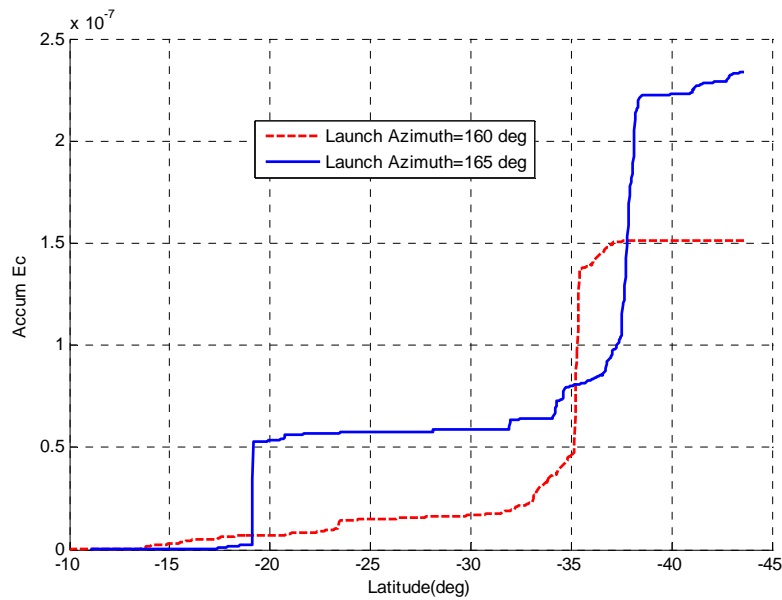


Fig.4.47 Comparison of accumulated Ec in Australia vs. latitude by the launch vehicle failure in 496-507 sec with July wind profile between the cases of 160 and 165 degree launch azimuths with SAPAR application

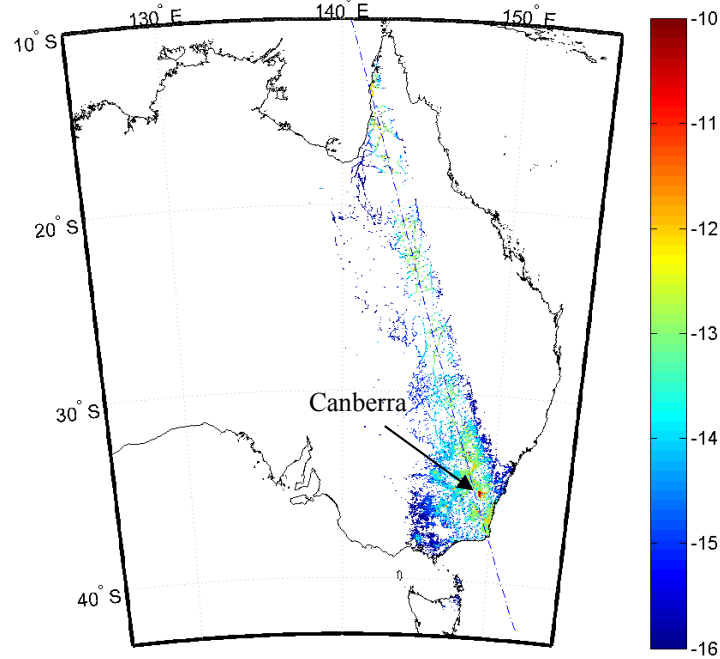


Fig.4.48 Expected casualty distribution ($\log_{10}(E_c/\text{km}^2)$) of Australia by the launch vehicle failure in 496-507 sec with July wind profile with SAPAR application (launch azimuth =160 degree)

4.3.3.4 Surface catalyticity of the object

In the aerthermodynamics module of SAPAR code, the convective heat flux in continuum regime was calculated using the Detra, Kemp, and Riddell formula [49]. This equation approximates the Fay-Riddell formula for stagnation heat flux of a sphere with the assumption of equilibrium boundary layer or frozen boundary layer and fully catalytic surface [27, 50, 51]. If the boundary layer is not equilibrium and the surface is not fully catalytic, the convective heat flux to the body may be reduced. In

this section, a factor was introduced to modify the stagnation heat flux to account for this uncertainty. The factor, which is called stagnation heat flux factor, can be multiplied by the original stagnation heat flux calculated with Eq. (3.13) of Detra, Kemp, and Riddell formula to produce the modified stagnation heat flux to the object;

$$\dot{q}_{ss} = F_{stg_heat} \times \frac{110285}{\sqrt{R}} \left(\frac{\rho}{\rho_{sl}} \right)^{0.5} \left(\frac{V}{V_{cir}} \right)^{3.15} \quad (4.1)$$

Where,

F_{stg_heat} : stagnation heat flux factor

This factor is unity (1.0) when the boundary layer is equilibrium or the surface of the object is fully catalytic while the value can be about 0.5 when the flow of the boundary layer is frozen and the surface is noncatalytic [47]. For an object of 1 m diameter made of metal or oxide, this factor can be 0.7~1.0 at the altitude of 75 km and velocity of 7.9 km/s [63]. It should be noted that as the altitude or the velocity of the object decreases this factor grows higher i.e. the actual heat flux gets closer to that obtained by Detra, Kemp, and Riddell formula.

Figure 4.49 shows the accumulated Ec in Australia according to the stagnation heat flux factor as a function of the latitude. The July wind profile was used in the simulation. As can be seen in the figure, the expected casualty decreases from 4.68e-7 to 2.34e-7 when the factor varies from 0.5 to 1.0. When the factor is 0.7, the Ec is about 4.11e-7, which is about 42% of the Ec value for the case without SAPAR (Ec=9.74e-7). The Ec result with the factor of 0.7 for the typical components of launch vehicles is a conservative one because the object velocity at the altitude of 75 km is much lower than 7.9 km/s and the catalyticity gets higher. Moreover the maximum heat fluxes of reentering objects from launch vehicles occur at the altitude between 50 and 60 km where the surface catalyticity is larger than for 75km altitude.

Chapter 4

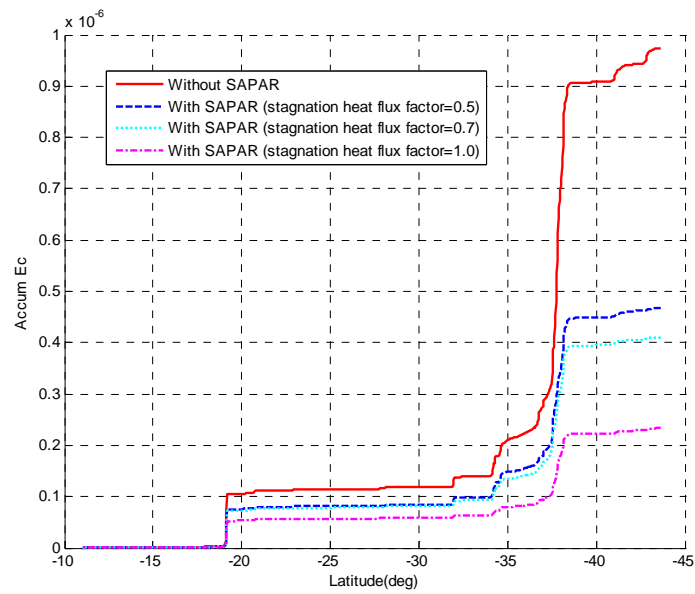


Fig. 4.49 Comparison of accumulated Ec in Australia vs. latitude by the launch vehicle failure in 496-507 sec with July wind profile between the cases varying the stagnation heat flux factor

Chapter 5. Conclusions

Flight safety analyses for launch vehicles have been conducted prior to the launches for several decades in space faring nations in order to confirm that the risks posed to the ground by the launches of launch vehicles are acceptably low. In these analyses, the vehicle debris have been usually assumed to impact the Earth surface in their initial state without any melting even if the vehicle's debris fall at very high speed. Consequently, this procedure can result in an overestimated risk and can subsequently increase the launch or development cost for a launch vehicle to reduce risk factors. To this end, present research is aimed at improving the flight safety analysis and at more accurate assessment of the risk posed to the public on the ground by incorporating the survivability analysis of the debris in the analysis procedure.

To do this, a program to analyze the flight safety of a launch vehicle was developed. In order to generate the probability density distribution of the impact points for the debris of a failed vehicle, the impact uncertainties were calculated based on the effects of the normal vehicle guidance and performance error and uncertainties in imparted velocities of debris by explosion, debris ballistic coefficients, wind, and lift. With the obtained impact probability density distribution, the probability of impact was calculated for each fragment group on each population center. The final casualty expectation was computed based on the probability of each fragment group impacting the population center, the casualty area of the fragment group, and the population density of the center. In addition, a sheltering model to account for the protection provided to persons located inside structures was employed in this procedure. It was shown that the analysis results by the developed code was in good agreement with the analysis using TumCor program developed by ACTA(Inc) in USA which employs relatively simple approach for expected casualty analysis.

A code (SAPAR: Survivability Analysis Program for Atmospheric Reentry) to analyze the survivability of debris reentering the Earth's atmosphere at high velocity

Chapter 5

was developed to be included in the flight safety analysis procedure. This code employs integrated trajectory, aerodynamic, aerothermodynamic and thermal modules to simulate the reentry process. The trajectory was simulated by integrating the three degree-of-freedom (DOF) equations of motion in ECI (Earth Centered Inertial) frame. The aerothermodynamic load during free fall, the temperature variation due to thermal load, and the phase shift after reaching the melting point were integrated into the trajectory simulation of the debris. The trajectory simulation continues until whole fragment demises or the fragment impacts the ground. As a final result, the size and weight of the debris impacting the ground were predicted. The program was validated by comparing the results with those of the programs (ORSAT and SCARAB) developed by NASA and ESA. The demise altitudes and the impact masses were in good agreement with those obtained by ORSAT or SCARAB. Especially, the analysis on an actually reentered orbital object performed by the code predicted the measured results more accurately with the improvement in the reradiation heat loss calculation, when compared with ORSAT.

As a next step, the survivability analysis code was combined with the flight safety analysis program to analyze the flight safety of the upper stage of a 2-stage launch vehicle. It was shown that the resulting expected casualty with debris survivability analysis was much lower than the case in which the demise of debris wasn't considered, by about 76% for Australia where the vehicle's IIP passed through when the vehicle's velocity was above 6.5 km/s. As the velocity of the vehicle at fail time becomes higher, difference between the expected casualties for the two cases grows larger. Therefore, it can be concluded that the survivability analysis should be included in flight safety analyses of launch vehicles for the time period when the vehicles fly at high speed near the orbital velocity. With this procedure, the expected casualty value can be lowered, while still sustaining the physical consistency. This can, in some cases, result in the reduction of launch or development cost by excluding the additional activities to eliminate the risk factors such as modification of vehicle configuration or evacuation of residence in high-risk locations.

In order to investigate the effects of uncertainty variations, analyses by the developed program with various conditions were also conducted. It was shown that the wind profile, the IIP trajectory, and explosion velocity could have significant effects on the expected casualty of a launch vehicle. To reduce the risk from launch failures of launch vehicles, the change of launch month or the modification of the vehicle trajectory etc. can be useful measures. Simulations varying the stagnation heat flux factor were performed to account for the uncertainty regarding the catalyticity of the object surface. As the stagnation heat flux factor becomes small i.e. the catalyticity of the surface becomes weak, the expected casualty was analyzed to get higher due to less ablation of the object. Nevertheless, even if a conservative value for the stagnation heat flux factor was used, the expected casualty was predicted to be lowered by about 60% when compared with the value of the case in which the demise of debris wasn't considered.

Flight safety analyses were conducted assuming the vehicle exploded on their nominal trajectory in this research. However, if a vehicle fails by losing its thrust or by malfunction turn like tumbling, it begins free fall in its intact state following a possible destruction due to aerothermodynamic or structural loads. In those cases, the survivability analysis gets more difficult than in the case of vehicle explosion because the destruction phenomena should also be predicted and a number of uncertainties exist in the process. The breakup altitude can have a great effect on the final survivability analysis while this altitude is also hard to predict. In order to account for these uncertainties a parametric study varying the breakup altitudes and the resulting fragments emerged from the intact vehicle can be utilized.

The developed methodology and program for flight safety analyses of space launch vehicles can be used in the analyses of flight safety for the future launch vehicles of Korea such as KSLV-II (Korea Space Launch Vehicle – II). By considering the demise of fragments falling at high velocity, the flight safety analyses on those launch vehicles are expected to generate more rigorous and realistic results. In addition, the results of the analyses performed in the present research for various conditions can be utilized

Chapter 5

widely in the development and launch of the future launch vehicles.

Bibliography

- [1] AFSPC/SEC, AFSPC/SE. Air Force Space Command Manual 91-710, Volume 1~7. July 1, 2004.
- [2] Federal Aviation Administration, Code of Federal Registration Parts 401, 406, 413, et al. Licensing and Safety Requirements for Launch; Final Rule, U.S. Department of Transportation, Aug. 25, 2006.
- [3] National Aeronautics and Space Administration, Procedural Requirements 8715.5A-Range Safety Program, Sep. 2010.
- [4] Space Licensing and Safety Office, Flight Safety Code, Commonwealth of Australia, Department of Industry, Science and Resources, Australia, June 19, 2001.
- [5] Hammond, W. G. and Geisinger, R.E., "Reducing Safety Constraints Through Vehicle Design," AIAA Paper 70-248, AIAA Launch Operations Meeting, Cocoa Beach, Fal., Feb. 2-4, 1970.
- [6] Baker, J.B., Collins, J. D., and Haber J. M., "Launch Risk Analysis," Journal of Spacecraft and Rockets, Vol. 14, No. 12, pp. 733-738, 1977.
- [7] Range Safety Data for Saturn SA-10, George C. Marshall Space Flight Center, NASA, June 17, 1965.
- [8] AS-206 Launch Vehicle Operational Trajectory Range Safety Analysis, TN-AP-67-157, Space Division, Chrysler Corp., Jan 1967.
- [9] AAP-IA Launch Vehicle Performance and Preliminary Range Safety Analysis. Volume 2 Range Safety, SSR-107(TN-AP-67-279), Space Division, Chrysler Corp., Nov, 1967.
- [10] Montgomery, R. M., "Range Safety of the Eastern Test Range," AIAA Paper 70-246, AIAA Launch Operations Meeting, Cocoa Beach, Fla., Feb. 2-4, 1970.
- [11] Larson, E.W.F., Haber, J.M., Morris, J.O., and Collins, J.D., "A General Methodology for Analysis of Risks from Falling Debris," Proceedings of the 1st IAASS Conference, 25-27, Oct. 2005, Nice, France.
- [12] Lin, M.Y., Larson, E.W., and Collins, J.D. "Determination of Debris Risk to the

Bibliography

Public Due to the Columbia Breakup During Reentry,” Appendix D.16 Columbia Accident Investigation Board Report, September 2003

[13] Collins, J.D., "Risk Analysis Methodologies Developed for the US Department of Defense," Journal of Reliability Engineering and System Safety 1, #1, Jan 1988

[14] Federal Aviation Administration, Flight Safety Analysis Handbook, Version 1.0, U.S. Associate Administrator for Commercial Space Transportation, Sep. 2011.

[15] Anselmo, L., and Pardini, C., "Computational Methods for Reentry Trajectory and Risk Assessment," Advances in Space Research, Vol. 35 (2005), pp. 1343-1352

[16] Ailor, W., Hallman, W., Steckel, G. and Weaver, M., "Analysis of Re-Entered Debris and Implications for Survivability Modeling," In Proceedings of the Fourth European Conference on Space Debris, ESA SP-587.

[17] Botha, W. "Orbital debris: a case study of an impact event in South Africa," in: Sawaya-Lacoste, H. (Ed.), Proceedings of the Third European Conference on Space Debris, ESA SP-473, vol. 2, Noordwijk, The Netherlands, pp. 501–506, 2001.

[18] Klinkrad, H., *Space Debris-Chap.9 Re-entry Prediction and On-Ground Risk Estimation*, Springer Berlin Heidelberg, 2006. pp.241-288

[19] Lips, T., and Fritsche, B., "A comparison of commonly used re-entry analysis tools," Acta Astronautica. 57(2-8), pp. 312-323, 2005.

[20] Tewari, A., "Entry trajectory model with thermomechanical breakup," Journal of Spacecraft and Rockets. Vol. 46, No. 2, pp. 299-306, 2009.

[21] Kato, A, "Comparison of national space debris mitigation standards," Advance in Space Research. Vol. 28, No.9, pp. 1447-1456, 2001

[22] Fritsche, B., Klinkrad, H., Kashkovsky, A., and Grinberg E., "Spacecraft Disintegration during Uncontrolled Atmospheric Re-entry," Acta Astronautica, Vol. 47, 2000, pp. 513-523

[23] Rochelle, W. C., Kinsey, R. E., Reid, E. A., Reynolds, R. C., and Johnson, N. L., "Spacecraft Orbital Debris Reentry Aerothermal Analysis," NASA CP3359, Sept. 1997

[24] Bouslog, S. A., Ross, B. P., and Madden, C. B., "Space Debris Reentry Risk Analysis," AIAA Paper 94-0591, 1994

Bibliography

- [25] Lips, T., Wartemann, V., Koppenwallner, G., Klinkrad, H., Alwes, D., Dobarco-Otero, J., Smith, R. N., DeLaune, R. M., Rochelle, W. C., and Johnson, N. L., "Comparison of ORSAT and SCARAB Reentry Survival Results", Proceedings of the 4th European Conference on Space Debris, Darmstadt, Germany, 2005.
- [26] Anon. Debris Assessment Software User's Guide Version 2.0. NASA/JSC, JSC64047, Houston, TX, USA, Nov 2007.
- [27] Dobarco-Otero, J., Smith, R. N., Marichalar, J. J., Opiela, J. N., Rochelle, and W. C., Johnson, N. L., "Upgrades to Object Reentry Survival Analysis Tool (ORSAT) for Spacecraft and Launch Vehicle Upper Stage Applications," 54th, International Astronautical Congress, Bremen, Germany. Sep 29-Oct 3, 2003.
- [28] Dobarco-Otero, J., Smith, R.N., Bledsoe, K. J., Delaune, R., M., Rochelle, W.C., and Johnson, N.L., "The Object Reentry Survival Analysis Tool(ORSAT)-Version 6.0 And Its Application To Spacecraft Entry," 56th International Astronautical Congress, Fukuoka, Japan. Oct. 17-21, 2005.
- [29] O'Hara, R. E., and Johnson, N. L. Reentry survivability risk assessment of the extreme ultraviolet explorer (EUVE), in: Proceedings of the 3rd European Conference on Space Debris, Darmstadt, Germany, Mar 19-21 2001 (ESA SP-473, pp. 541-546). ESA Publications Divisions, ESTEC, Noordwijk, The Netherlands, 2001.
- [30] Rochelle, W. C., Marichalar, J. J., and Johnson, N. L. Analysis of reentry survivability of UARS spacecraft. Adv. Space Res. 34(5), pp. 1049-1054, 2004.
- [31] Rochelle, W. C., Kirk, B. S., Ting, B. C., Smith L. N., Smith R. N., Reid, E. A., Johnson, N. L, and Madden, C. B. "Modeling of space debris reentry survivability and comparison of analytical methods," paper IAA-99-IAA.6.7.03, in: Proceedings of 50th IAC, Amsterdam, Netherlands, 1999.
- [32] Lips, T., Fritsche, B., Koppenwallner, G., and Klinkrad, H., "Spacecraft Destruction during Re-entry – Latest Results and Development of the SCARAB Software System," Advances in Space Research, 34 (2004), pp. 1055-1060
- [33] Ziniu, W., Ruifeng, H., Xi, Q., Xiang, W. and Zhe, W., "Space Debris Reentry Analysis Methods and Tools," Chinese Journal of Aeronautics, Vol. 24, 2011. pp 387-

395.

- [34] Hu R F, Wu Z N, Qu X, "Debris Reentry and Ablation Prediction and Ground Risk Assessment System," *Acta Aeronautica et Astronautica Sinica* 2011; 32(3): 390-399. [in Chinese]
- [35] Hyung-seok Sim and Kyu-hong Kim, "Reentry Survival Analysis of Tumbling Metallic Hollow Cylinder," *Advances in Space Research* 48 (2011), pp. 914-922.
- [36] Malys, S., *The WGS84 Reference Frame*, National Imaginary and Mapping Agency, Nov. 7, 1996.
- [37] "US Standard Atmosphere, 1976," NASA-TM-X-74335, NASA 1976.
- [38] Justus, C. G., Jeffries, W.R., Yung, S., and Johnson, D.L., "NASA/MSFC Global Reference Atmospheric Model-1995 (GRAM-95)," NASA-TM-4715, Aug. 1995.
- [39] Matogawa, Y., Hinada, M., and Fukuda, K., "Statistical Analysis of Impact Points of Rockets," Institute of Space and Aeronautical Science, University of Tokyo, Report No. 520, Dec. 1974.
- [40] 2nd IAASS Conference. Range Safety Training Material. ACTA Inc., 2007.5
- [41] Larson, Erik W.F., "Large Region Population Sheltering Models for Space Debris Risk Analysis," 15-18 Aug. 2005, AIAA Atmospheric Flight Mechanics Conference and Exhibit
- [42] Sim, Hyungseok, Ko, Jeonghwan, Choi Kyusung, and Roh, Woongrae, "Sheltering Model for Flight Safety Analysis of Space Launch Vehicle," Proceeding of the 2008 KSAS spring conference.
- [43] Sim, Hyungseok, Ko, Jeonghwan, Choi Kyusung, "Sheltering model for flight safety analysis of KSLV-I," KARI-MDT-TM-2008-015, Technical Memorandum, Korea Aerospace Research Institute, 2008.
- [44] US Oak Ridge National Laboratory, <http://www.ornl.org>
- [45] Klett, R. D., "Drag Coefficients and Heating Ratios for Right Circular Cylinders in Free-Molecular and Continuum Flow from Mach 10 to 30," Sandia Corporation SC-RR-64-2141, Dec 1964.
- [46] Cropp, L. O., "Analytical Methods used in Predicting the Re-entry Ablation of

Bibliography

Spherical and Cylindrical Bodies,” Sandia Corporation SC-RR-65-187, Sep 1965.

[47] Anderson, J.D., *Hypersonic and High Temperature Gas Dynamics*, McGraw-Hill, 1998

[48] Sim, Hyungseok, Ko, Jeonghwan, Choi Kyusung, “Development of Survivability Analysis Program for Atmospheric Reentry,” KARI-MDT-TM-2010-004, Technical Memorandum, Korea Aerospace Research Institute, 2010.

[49] Detra, R. W., Kemp, N. H., and Riddell, F. R., "Addendum to heat transfer to satellite vehicles reentering the atmosphere," *Jet propulsion*, Vol. 27, No. 12, 1957, pp. 1256-1257

[50] Fay, J. A., and Riddell, R. R., "Theory of Stagnation Point Heat Transfer in Dissociated Air," *Journal of the Aeronautical Sciences*, Vol. 25, No. 2, 1958, pp. 73-85, 121

[51] Bertin, J.J., *Hypersonic Aerothermodynamics*, AIAA, 1994

[52] Stoney, W.E., Jr. and Swanson, A.G., "Heat Transfer Measured on a Flat-Face Cylinder in Free Flight at Mach numbers up to 13.9," NACA RM-L-57E13, June 17, 1957

[53] Kelley, R. L., Rochelle, W.C. "Atmospheric Reentry of a Hydrazine Tank," NASA White Paper, www.thebulletin.org/files/NASA_White_Paper.pdf, 2012.10.10. revisited

[54] White, F.M., *Heat Transfer*, Addison-Wesley Publishing company, 1984

[55] Anon. User's Manual, SINDA/FLUENT General Purpose Thermal/Fluid Network Analyzer-Version 4.8. Cullimore and Ring Technologies, Inc., Littleton, Co, USA, Oct. 2005

[56] Collins, J. D., Nyman, R., and Lottati, I., “Estimation of Space Shuttle Orbiter Reentry Debris Casualty Area,” AIAA paper 2005-6321, AIAA Atmospheric Flight Mechanics Conference and Exhibit, Aus. 15-18, 2005.

[57] Sun, B, C, Park, Y, G, Roh, W, R, and Cho, G, R, “Attitude Controller Design and Test of Korea Space Launch Vehicle-I Upper Stage,” *International Journal of Aeronautical and Space Science*. 11(4), pp. 303-312, 2010.

Bibliography

- [58] LaFarge, R. A., "Using Monte Carlo Technique and Parallel Processing for Fragmentation Analysis of Explosive payloads," AIAA-92-0653, 30th Aerospace Science Meeting & Exhibit, 6-9 Jan. 1992.
- [59] Qutka, D. E., LaFarge, R. A., "Mission Hazard Assessment for STARS Mission 1 (M1) in the Marshall Islands Area," SAND93-0218, Sandia National Labs, 1993.
- [60] Rao, P. P., Woeste, M. A., "Monte Carlo Analysis of Satellite Debris Footprint," AIAA Paper 79-1628.
- [61] R. M. Montgomery, J. A. Ward Jr. "Casualty Areas from Impacting Inert Debris for People in the Open", 1995, RTI Report No. RTI/5180/60-31F
- [62] Newman, L. K., Folta D. C., Ross, B. P. and Bouslog, S. A., "Reentry Analysis for Low Earth Orbiting Spacecraft," AAS/NASA International Symposium on Space Flight Dynamics, April, 1993.
- [63] Goulard, R., "On Catalytic Recombination Rates in Hypersonic Stagnation Heat Transfer," Jet Propulsion, Vol. 28, No. 11, 1958, pp. 737-745

국문초록

본 연구의 핵심은 큰 속도로 비행하는 우주발사체가 실패하는 경우의 정확한 지상 인명피해 분석을 위해 파편 대기 재진입 생존성을 고려한 비행안전 분석을 수행하는 것이다.

우주발사체의 비행안전 분석은 비행 실패를 가정한 파편 낙하 시뮬레이션, 지상 낙하 영역 분석, 파편 피해면적과 인구 분포를 이용한 예상 인명피해 추정의 과정으로 수행된다. 우주발사체가 큰 속도에서 실패하는 경우에 파편이 지구 대기에 재진입하는 과정에 큰 공력 열하중에 의해 녹아서 크기가 작아지거나 없어질 수 있으며 이는 지상 인명피해를 줄이는 영향을 준다. 따라서 빠른 속도로 낙하하는 파편에 의한 보다 정밀한 예상인명피해 분석을 위해서는 파편의 재진입 생존성 분석의 고려가 요구된다.

본 연구는 정확한 우주발사체 비행안전 분석을 위해 3가지 연구를 중심으로 수행되었다.

첫째, 우주발사체의 비행안전 분석 프로그램을 개발하였다. 먼저 우주발사체의 비행실패에 의한 파편의 지상 낙하 영역 분석을 위해 파편 폭발 속도의 불확실성, 탄도계수의 불확실성, 유도성능오차, 바람과 양력의 영향을 고려하였다. 인명이 건물 등에 위치하여 파편에 의해 보호되는 영향을 포함할 수 있도록 Sheltering 모델을 적용하였다. 최종적으로 파편의 피해 면적과 인구 분포를 이용하여 예상 인명 피해를 분석하였다. 분석 결과는 비교적 단순한 분석법을 사용하는 미국 ACTA(社)의 TumCor 프로그램 결과와 비교되었다.

둘째, 큰 속도로 지구에 재진입하는 파편의 생존성 분석을 위한 코드가 개발되었다. 3자유도 파편 낙하 시뮬레이션 과정에 파편이 낙하하는 도중에 받게 되는 공력 열하중, 열하중에 의한 파편의 온도변화, 녹는점에 도달한

후 물체의 상변화 여부 등을 포함하여 최종적으로 지상에 낙하하는 파편의 크기와 무게를 분석하였다. 개발된 코드의 검증을 위하여 단순한 형태의 파편에 대한 생존성 분석을 수행하여 NASA와 ESA의 코드 결과와 비교하였다. 또한 실제 재진입 파편에 대한 분석을 수행하여 측정된 결과와 비교하였다.

마지막으로, 개발된 재진입 생존성 분석 코드를 비행안전 분석 과정에 결합하여 2단형 발사체의 상단에 대한 비행안전 분석을 수행하였다. 생존성 분석을 포함하는 경우의 영향을 분석하기 위하여 생존성 분석이 배제되어 수행된 분석결과와 비교하였다. 결과적으로 생존성 분석을 고려하는 경우에 고려치 않은 결과에 비해 상당한 수준의 예상인명피해의 감소가 있는 것으로 나타났으며, 발사체가 빠른 속도로 비행하는 구간에서는 생존성 분석의 고려가 필수적임을 확인하였다. 또한, 불확실성을 가진 변수들의 영향을 살펴보기 위하여, 개발된 프로그램을 이용한 다양한 비행조건과 환경조건에 대한 분석을 수행하였으며 바람 프로파일, 발사체 폭발속도, 발사방위각이 예상인명피해에 큰 영향을 미치는 것을 확인하였다.

주요어 : 우주발사체, 비행안전분석, 파편 낙하영역, Sheltering, 지구 재진입, 극초음속, 공력 열하중, 생존성

학번 : 2009-30167

이름 : 심형석

감사의 글

석사 졸업 후 만 10년 만에 입학한 박사 과정은 제게 주어진 물리적 여건들과 오랜 학습 공백에 대한 우려로 자신감보다는 걱정스러움이 앞선 상태에서 시작되었습니다. 주어진 직장 업무를 소홀히 하지 않으면서 박사학업을 병행해야 하는 데 따른 부담감에 가슴 한 켠에 커다란 돌을 얹고 있는 듯한 기분을 내내 느껴야 했습니다. 돌이켜 보면 애초의 우려에도 불구하고 졸업이라는 문 앞에 무사히 설 수 있었던 것은 많은 주위 분들의 도움 때문이었습니다.

먼저 학업을 계속할 수 있게 시간을 허락해 준 한국항공우주연구원에 감사의 말씀을 드립니다. 또한 박사 입학을 결심하고 찾아 뵈었을 때 큰 도움이 되지 않는 파트타임 학생을 흔쾌히 받아 주시고 지도를 아끼지 않으신 김규홍 교수님께 진심으로 고개 숙여 감사의 말씀을 올립니다. 시간을 쪼개어 부족한 논문 심사에 애써주신 이동호 교수님, 윤영빈 교수님, 변영환 교수님께도 노고에 깊이 감사의 말씀을 올립니다. 바쁜 와중에도 학업에 시간을 할애할 수 있게 배려해 주신 연구원의 노웅래 박사님께 이 자리를 빌어 감사 드립니다. 업무적으로도 많은 배려를 해주시고 논문 방향에 대한 조언뿐만 아니라 심사까지 마다하지 않으신 고정환 박사님께 무한한 감사의 말씀을 올립니다. 박사 주제를 정하지 못해 주저하는 저를 일깨워 주고 SCI 논문의 길을 알려주신 김성룡 박사님, 정신 없이 바쁜 중에도 시간을 내어 제 연구에 많은 도움을 주고 어려운 문제에 대한 명쾌한 답을 주신 조상범 박사님, 결과 검증과 토론을 함께 해 주신 최규성 박사님의 도움이 없었다면 이 논문은 완성되지 못했을 것입니다. 후배에게 도움을 준다면 저널 논문 교정도 해 주고 고민 있을 때마다 자기 일처럼 신경 써 준 동원이 형, 고등학교 선배라고 제 문제를 같이 고민해 주고 답을 제시해 준 주용이, 논

문의 부족한 면을 채워준 최상호 선임께도 고맙다는 말을 전합니다. 그 밖에 여러모로 도움을 주신 팀 분들과 연구원의 다른 분들께도 감사의 말씀을 올립니다.

적지 않은 나이로 입학한 저를 굴러온 돌이라 무시하지 않고 동료로서 인정해 준 실험실 선후배들이 없었다면 저의 박사과정은 더욱 힘들었을 것입니다. 미안한 말이지만 늦게까지 학교에 남아줘서 실험실 환경이 낯선 저에게 큰 힘이 되어준 동기 재완이, 같은 나이라고 챙겨준 우례, 한 살 많다고 각듯이 대해준 정상이와 상훈이에게 특히 고맙다는 말을 하고 싶습니다. 실험실 일 때문에 바빠 졸업 못하고 있는 가람이, 곧 졸업을 앞둔 태경이, 정호, 준우, 성준이, 정현이 등 해준 것 없는 저를 선행으로 대해준 후배들에게도 감사의 말을 전하고 싶습니다. 후배님들의 앞날에 큰 영광이 있길 바랍니다.

힘들 때 부린 투정을 다 받아주며 격려해 준 아내 주리에게 이 감사의 글이 아주 작은 보답이라도 된다면 좋겠습니다. 우리 아이들에게 부끄러운 아빠가 되지 않기 위해 부단히 노력하고자 하였습니다. 현성이와 환익이가 제가 이룬 조그마한 성과에 자부심을 가질 수 있기를 마음속으로 간절히 빌어봅니다. 다 키워 독립시키시고도 늦게 공부한다고 힘들지 않냐고 항상 걱정해 주신 어머니의 은혜에 무슨 말로 감사드릴 수 있을 지 모르겠습니다. 하나뿐인 남동생, 오빠를 응원해준 누나들과 매형들, 여동생 내외에게도 고맙다는 말을 전합니다. 또한 부족한 저를 사위로 받아들여 주시고 묵묵히 사랑으로 응원해 주신 장인어른, 장모님께도 감사의 마음을 올립니다. 마지막으로 누구보다 기뻐하실 하늘에 계신 아버님께 존경을 담아 이 논문을 바칩니다.

2013년 1월 1일

심 형 석 올림